Kim Johnsen

Sorption-Enhanced Steam Methane Reforming in Fluidized Bed Reactors

Thesis for the degree philosophiae doctor

Trondheim, October 2006

Norwegian University of Science and Technology
Faculty of Natural Sciences and Technology
Department of Materials Science and Engineering

NTNU
Innovation and Creativity

IMT-Report 2006:87

NTNU
Norwegian University of Science and Technology

Thesis for the degree philosophiae doctor

Faculty of Natural Sciences and Technology
Department of Materials Science and Engineering

ISBN 82-471-7991-1 (printed version)
ISBN 82-471-7990-3 (electronic version)
ISSN 1503-8181

Doctoral theses at NTNU, 2006:116

Printed by NTNU-trykk

Preface

The work presented in this thesis has been carried out at the Department of Environmental Technology at Institute for Energy Technology (IFE), Kjeller in the period of February 2003 to June 2006. Parts of the work were also performed at the Norwegian University of Science and Technology (NTNU) in Trondheim, and at University of British Columbia (UBC) in Vancouver, Canada.

The work is a part of the larger project "*Future energy plants; Co-production of electrical power and hydrogen from natural gas with integrated CO_2-capture*", financed by the Research Council of Norway through the KLIMATEK program. This project is a co-operation between IFE, Christian Michelsen Research and Prototech AS, where the objectives have been to develop and test a concept for co-production of electricity and hydrogen from natural gas with integrated CO_2-capture. The work presented in this thesis is focusing on the hydrogen production part of the project.

Abstract

Hydrogen is considered to be an important potential energy carrier; however, its advantages are unlikely to be realized unless efficient means can be found to produce it without generation of CO_2. Sorption-enhanced steam methane reforming (SE-SMR) represent a novel, energy-efficient hydrogen production route with *in situ* CO_2 capture, shifting the reforming and water gas shift reactions beyond their conventional thermodynamic limits.

The use of fluidized bed reactors for SE-SMR has been investigated. Arctic dolomite, a calcium-based natural sorbent, was chosen as the primary CO_2-acceptor in this study due to high absorption capacity, relatively high reaction rate and low cost. An experimental investigation was conducted in a bubbling fluidized bed reactor of diameter 0.1 m, which was operated cyclically and batchwise, alternating between reforming/carbonation conditions and higher-temperature calcination conditions. Hydrogen concentrations of >98 mole% on a dry basis were reached at 600°C and 1 atm, for superficial gas velocities in the range of ∼0.03-0.1 m/s. Multiple reforming-regeneration cycles showed that the hydrogen concentration remained at ∼98 mole% after four cycles. The total production time was reduced with an increasing number of cycles due to loss of CO_2-uptake capacity of the dolomite, but the reaction rates of steam reforming and carbonation seemed to be unaffected for the conditions investigated.

A modified shrinking core model was applied for deriving carbonation kinetics of Arctic dolomite, using experimental data from a novel thermo gravimetric reactor. An apparent activation energy of 32.6 kJ/mole was found from parameter fitting, which is in good agreement with previous reported results. The derived rate expression was able to predict experimental conversion up to ∼30% very well, whereas the prediction of higher conversion levels was poorer. However, the residence time of sorbent in a continuous reformer-calciner system is likely to be rather low, so that only a fraction of the sorbent is utilized, highlighting the importance of the carbonation model at lower

conversions.

A dual fluidized bed reactor for the SE-SMR system was modeled by using a simple two-phase hydrodynamic model, the experimentally derived carbonation kinetics and literature values for the kinetics of steam reforming and water gas shift reactions. The model delineates important features of the process. Hydrogen concentrations of >98 mole% were predicted for temperatures ∼600°C and a superficial gas velocity of 0.1 m/s. The reformer temperature should not be lower than 540°C or greater than 630°C for carbon capture efficiencies to exceed 90%. Operating at relatively high solid circulation rates to reduce the need for fresh sorbent, is predicted to give higher system efficiencies than for the case where fresh solid is added. This finding is attributed to the additional energy required to decompose both $CaCO_3$ and $MgCO_3$ in fresh dolomite. Moreover, adding fresh sorbent is likely to result in catalyst loss in the purge stream, requiring sorbents with lifetimes comparable to those of the catalyst.

Thermo gravimetric analysis (TGA) was used to study the reversible CO_2-uptake of sorbents. In general, the multi-cycle capacity of the dolomite was found rather poor. Therefore, synthetic sorbents that maintain their capacities upon multiple reforming-calcination cycles were investigated. A low-temperature liquid phase co-precipitation method was used for synthesis of Li_2ZrO_3 and Na_2ZrO_3. Li_2ZrO_3 showed a superior multi-cycle capacity compared to Arctic dolomite in TGA, but the rate of reaction in diluted CO_2 atmospheres was very slow. The synthesized Na_2ZrO_3 proved to have both fast carbonation kinetics and stable multi-cycle performance. However, regeneration in the presence of carbon dioxide was not easily accomplished.

The findings of this thesis suggest that the bubbling fluidized bed reactor is an attractive reactor configuration for SE-SMR. Low gas throughput is the major disadvantage for this configuration, and operation in the fast fluidization regime is most likely to be preferred on an industrial scale of the process. Future work should focus on developing sorbents and catalysts that are suited for high velocity operation, with respect to reactivity and mechanical strength.

Acknowledgement

First, I would like to acknowledge Institute for Energy Technology (IFE) for financial support through the Zero Emission Gas (ZEG) project, sponsored by the Research Council of Norway. I would like to thank my superiors at the Department of Environmental Technology, Bjørg Andresen and Dag Eriksen, for their support and for always having confidence in my work. I also thank my colleague Julien Meyer for many informal and inspiring discussions on various aspects of the project. I am grateful to my former colleague Kwang Bok Yi, who unfortunately, for us, had to return to Korea, for numerous discussions and for all his clever experimental devices, making laboratory work more enjoyable. You are the *real* MacGyver !

I thank my supervisor, professor Leiv Kolbeinsen at Department of Materials Science and Engineering, NTNU, for his guidance and helpful advice during all stages of this work. In particular, I appreciate him for letting me follow my own path during my work. Also, I have appreciated his hospitality and the tasteful dinners prepared by his wife, Anne Kath, at their house during my spells in Trondheim.

The completion of this work would not have been possible without my stay at the University of British Columbia, Vancouver. Being a part of the Fluidization Group at the Department of Chemical and Biological Engineering was very inspiring and important for the progress of my work. In particular, the expertise of professor John Grace has been invaluable for the experimental part of the project, and I am grateful for the fruitful e-mail correspondence after I returned to Norway, resulting in a couple of journal papers. I would also like to thank professors Jim Lim and Said Elanashaie for their guidance during my stay. Dr. Ho-Jung Ryu deserves my gratitude for helping out with the modifications of the fluidized bed reactor, making operation possible within a limited period of time. These modifications had not been possible without the

assistance of Dr. Pierre Constantineau. During my relatively short stay in Vancouver I got to know many extremely friendly Canadians. In particular, my landlady Betsy Jones deserves my greatest gratitude for her hospitality, great sense of humor, delicious Thanksgiving turkey and of course her cable TV.

I thank all my friends for taking me out, making me laugh and think of other things than this thesis.

More important, my parents deserve my gratitude for their support and encouragement during all my years of study.

Finally, I thank my beautiful Ragnhild for her love and patience. Her endless support has been invaluable for the completion of this thesis. On New Year's Eve 2005, she gave birth to our son, Didrik. His arrival has certainly put work into a different perspective and made the last months of writing less frustrating. The thesis is finished now, Ragnhild. Let's get married !

Contents

List of Figures

List of Tables

List of symbols and abbreviations

Latin symbols

Symbol	Description	Unit
a_b	Interfacial bubble area per unit volume	1/m
A_c	Cross-sectional area of reformer	m^2
a_w	Surface area of heating tubes	m^2
b	Stoichiometric constant	mole CaO/mole CO_2
$C_{i,b}$	Molar concentration in bubble phase	mole/m^3
$C_{i,d}$	Molar concentration in dense phase	mole/m^3
D	Gas phase diffusivity	m^2/s
D_e	Effective diffusivity	m^2/s
d_{eq}	Average bubble diameter	m
D_{Kn}	Knudsen diffusivity	m^2/s
$d_{p,catalyst}$	Average particle diameter of catalyst	m
$d_{p,dolomite}$	Average particle diameter of dolomite	m
$d_{p,mix}$	Average particle diameter of mixture	m
D_{pl}	Product layer diffusion constant	m^2/s
d_t	Diameter for bed	m
D_t	Outer diameter for heating tube	m
E_a	Activation energy of carbonation	kJ/mole
F_i	Molar flow rate in the riser	mole/s
F_s	Sorbent circulation rate	kg dolomite/s
g	Acceleration of gravity	m/s^2

Latin symbols (cont.)

Symbol	Description	Unit
G_s	Flux of solids in the riser	kg/(m^2 ·s)
H	Enthalpy of streams	J/mole
H_{mf}	Bed height at minimum fluidization velocity	m
$H_{2,eq}$	Hydrogen yield	mole H_2/mole CH_4
k	Rate constant of carbonation	m/s
K_E	Equilibrium constant for carbonation	1/atm
k_g	External mass transfer coefficient	m/s
k_q	Interphase mass transfer constant	m/s
k_0	Arrhenius constant	m/s
LHV	Lower Heating Value	kJ/mole
n	Nonlinearity factor	-
Q_c	Energy of compression	J/mole CH_4
Q_H	Heating demand of calciner	J/mole CH_4
Q_s	Heating demand/excess of streams	J/mole CH_4
P_{Eq}	Equilibrium partial pressure of CO_2	atm
P_{CO_2}	Partial pressure of CO_2	Pa
$P_{CO_{2,eq}}$	Equilibrium partial pressure of CO_2	Pa
R	Gas constant	J/(mole ·K)
$R_{dolo}(X)$	Rate of carbonation	mole/(m^3 dolomite ·s)
R_p	Sorbent particle radius	m
r_1, r_2, r_3	Reaction rate of catalytic reactions	kmole/(kg cat ·h)
T_1	Reformer temperature	°C
T_2	Calciner temperature	°C

Latin symbols (cont.)

Symbol	Description	Unit
T_w	Temperature of heating tubes	°C
U	Superficial gas velocity	m/s
U_A	Bubble rise velocity	m/s
U_{mf}	Minimum fluidization velocity	m/s
U_t	Terminal velocity	m/s
$V_{dolomite}$	Total volume of calcined dolomite in reformer	m^3
V_p	Dolomite particle velocity	m/s
X_{CaO}	Conversion of CaO in reformer	%
X_{Calc}	Conversion of $CaCO_3$ in calciner	%
Y_{CaO}, Y_{MgO}	Weight percentage in Arctic Dolomite	%
z	Vertical coordinate	m

Greek symbols

Symbol	Description	Unit
β	Gas fraction in bubble phase	-
γ	Feed mass ratio	kg sorbent/kg catalyst
ϵ_0	Initial voidage of calcined dolomite	-
ϵ	Voidage	-
ϵ_b	Voidage of bubbling bed	-
ϵ_{mf}	Voidage at minimum fluidization	-
η_r	Reformer efficiency	%
λ	Volumetric fraction of sorbent	m^3 sorbent/m^3 solids
μ	Gas viscosity	Pa· s
ρ_{CaO}	Molar density of CaO in dolomite	mole CaO/m^3 dolomite
ρ_{cat}	Density of catalyst	kg/m^3
ρ_{dolo}	Density of Arctic dolomite	kg/m^3
ρ_{mix}	Density of catalyst/dolomite mixture	kg/m^3
ρ_f/ρ_g	Density of gas in bed	kg/m^3
ρ_s	Density of solids	kg/m^3
τ	Tortuosity factor	-
ψ	Slip-factor (ratio between the particles and actual gas velocity)	-
ω_c, ω_d	Weight fraction of catalyst/dolomite	-

List of Abbreviations

AJI	Air Jet Index
ATR	Autothermal Reforming
BFBR	Bubbling Fluidized Bed Reactor
CCS	Carbon Capture and Storage
CFB	Circulating Fluidized Bed
CLC	Chemical Looping Combustion
EOR	Enhanced Oil Recovery
FCC	Fluid Catalytic Cracking
GHG	Greenhouse Gas
IPCC	Intergovernmental Panel on Climate Change
MEA	Monoethanolamine
POX	Partial Oxidation
PSA	Pressure Swing Adsorption
S/C	Steam-to-Carbon ratio
SCM	Shrinking Core Model
SE-SMR	Sorption-Enhanced Steam Methane Reforming
SMR	Steam Methane Reforming
TGA	Thermo Gravimetric Analysis
TSA	Temperature Swing Adsorption
WGS	Water Gas Shift

Chapter 1

Introduction

We have a mighty task before us. The Earth needs our assistance.

(Laurens van der Post)

Fossil fuels, coal, oil and natural gas, have been a widely used source of energy every since the Industrial Revolution just before the dawn of the 20th century. Present concerns regarding global warming due to CO_2 emissions from fossil fuel combustion have given rise to extensive efforts in preventing CO_2 reaching the atmosphere. In this chapter, the scientific basis of global warming is presented along with a technological overview of potential routes to "CO_2-free" energy production from fossil fuels. Special attention is given to hydrogen production from fossil fuels. The rationale of this thesis is presented at the end of the chapter.

1.1 Fossil fuel combustion

While the detailed science is complex, the basic premise of global warming is relatively simple. The earth's atmosphere contains so-called greenhouses gases (GHG) in a delicate balance with other gases. These GHG gases, which include water vapor, carbon dioxide, methane, ozone and nitrous oxide, serve to regulate the earth's temperature by allowing sunlight through to heat the earth's surface and then trapping and absorbing some of that heat as it is reflected back into space as infra-red radiation - this is the greenhouse effect. Without this natural greenhouse effect, earth surface temperatures would be much lower than they are now, and life as known today would not be possible. Instead, thanks to greenhouse gases, the earth's average temperature

is a more hospitable 15.6°C [1]. However, problems may arise when the atmospheric concentration of greenhouse gases increases.

1.1.1 Greenhouse gas emissions

Statistics from the Intergovernmental Panel on Climate Change (IPCC) reveal that the overall world's temperature has increased by 0.6°C over the past century, and is projected to increase by a further 1.6 to 5.5°C by 2100 [2]. Many scientists believe that the observed global warming is mainly due to changes in human activities and related increases in greenhouse gas emissions. Long droughts, severe cyclones, storm surges and abnormally high and low temperatures are becoming increasingly common and are causing a significant threat to people and their environments world-wide. These extreme weather conditions are considered by IPCC to be caused by global warming and climate change. Climate change is not a new phenomenon. The earth has undergone significant variations in climate during its estimated five billion year life. However, of particular concern is that the warming of today is occurring more rapidly than in any of the previous climate changes that the earth has experienced. Unlike previous climate changes this global warming has a very clear human component. The third assessment report of IPCC [2] gives a very comprehensive scientific overview on global warming and greenhouse gas emissions, and reports:

- The atmospheric concentration of carbon dioxide (CO_2) has increased by 31% since 1750.
- About 75% of the anthropogenic CO_2 emissions to the atmosphere during the past 20 years are due to fossil fuel burning.
- The atmospheric concentrations of methane, nitrous oxides and ozone have significantly increased since year 1750.

Historically, CO_2 emissions have come mainly from industrialized countries, but the trend is now shifting. Population growth in developing nations in Asia, the Middle East and Africa is increasing the energy demand, and economic growth is expected to cause a continued rise in emissions unless fundamental technology changes occur in the world's energy systems. The contribution of renewable energy sources are likely to increase in the future, but fossil fuels will continue to be the most important energy source for

many decades to come. It has been forecasted that, for a "business as usual"-scenario, global emissions of CO_2 could more than triple over this century, from 7.4 billion tons of carbon per year in 1997 to approximately 26 billion tons per year in 2100 [3]. This means that development of zero emission technologies for fossil fuel utilization will be critical in order to reverse the very clear trend of increased atmospheric CO_2 concentrations.

1.1.2 CO_2-free energy production from fossil fuels

Emissions from fossil based fuels can be reduced by switching to fuels with lower carbon content, increasing the fuel conversion efficiency or capturing and storing the carbon dioxide emitted. Natural gas, which has a somewhat lower carbon content than oil, will continue to take market shares from oil over the next decades. However, coal will maintain its position as an abundant and cheap fuel in the global electricity generation for the same period. Therefore, the development of energy efficient combustion processes and carbon capture and storage (CCS) will be of great importance.

Most of the emissions of CO_2 to the atmosphere are in the form of flue gas from combustion processes with typical CO_2 concentrations of 4-15% by volume [4]. In principle, flue gas could be stored to avoid emissions of CO_2 to the atmosphere, it then would have to be compressed to a pressure of typically more that 10 MPa which would require an excessive amount of energy. In addition to this, the high volume of flue gas would mean that storage reservoirs would be filled up quickly. For these reasons it is preferable to produce relatively pure CO_2 for transport and storage. There are three main routes to CO_2 capture from combustion processes, which are visualized in Figure 1.1, and briefly described below:

i) Post-combustion

ii) Oxy-fuel combustion

iii) Pre-combustion

Post-combustion

Post-combustion is a downstream process, capturing CO_2 after the combustion, where the most used process is to scrub the flue gas with a physical or chemical solvent. *Chemical absorption*, with monoethanolamine (MEA) being the most used solvent, is a

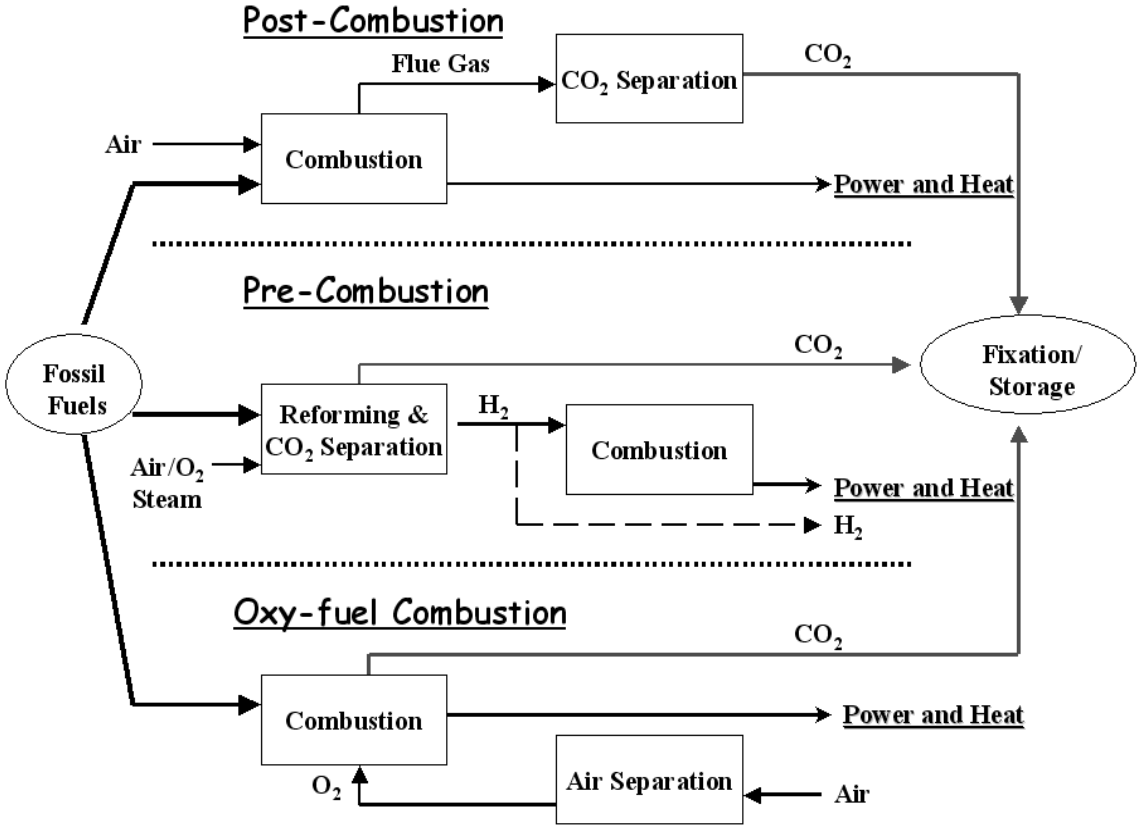

Figure 1.1: Schematic representation of main CO_2 capture routes [5].

relative mature technology. However, high degradation rates of the solvents in presence of SO_x, NO_2 and O_2, and the large amount of energy needed for regeneration are the major disadvantages making this technology very costly. Also, low CO_2 concentration in the power plant flue gas means that large volume of gas has to be treated, resulting in large equipment sizes. A number of novel solvents with higher selectivity for CO_2 and lower energy requirements for regeneration are therefore currently being investigated [6], in order to reduce the size of absorption towers and capital and operation costs.

Gas separation membranes are likely to be applied in CO_2 capture systems in the future. The driving force for separation is given by differences in partial pressure of gas species between the feed side and permeate side of the membrane. Developing membranes with both high selectivity and permeability for separation of carbon dioxide from flue gas is the major challenge. The cost of CO_2 capture from the exhaust gas of a coal fired power plant, using a polymer membrane, was found to be 30% more

expensive than for a conventional MEA absorption process [7]. However, the cost of the membrane process was significantly reduced when the CO_2 concentration in the flue gas was increased from 13% to 27%. In addition to gas separation membranes, *gas absorption membranes* offer high capture potential. These membranes work as contacting devices between the gas and the liquid phase, increasing the contact area, thus reducing the size of the scrubbing equipment [8]. They will potentially also reduce the mass transfer of undesirable gas phase components such as oxygen and nitrous oxide, which are known to degrade the alkanolamine solvent.

Cryogenic separation offers high recovery of CO_2, but the large amount of energy required to provide the refrigeration necessary for the process, particularly for dilute gas streams, is the major disadvantage. Some solid materials with high surface areas, such as zeolites and activated carbon, can be used to separate CO_2 from gas mixtures by *adsorption*. These processes operate on repeated cycles with the basic steps being adsorption and regeneration. The regeneration can be done by reducing the pressure, by so-called pressure swing adsorption (PSA), or by increasing the temperature, in temperature swing adsorption (TSA). Currently, adsorption is not considered attractive for large-scale separation of CO_2 from flue gas because the capacity and CO_2 selectivity of available adsorbents are low.

Oxy-fuel combustion

Using concentrated oxygen rather than air for combustion has the advantage of increasing the CO_2 concentration in the flue gas (>80%), eliminating the need for expensive downstream separation equipment. Oxygen can be supplied from cryogenic air separation and fed to either a boiler or a gas turbine. In order to avoid too high flame temperatures, the CO_2-rich flue gas is often recycled to make the flame temperature similar to a normal air blown combustor [4]. NO_x formation is also suppressed by using oxygen rather than air. The main disadvantage of oxy-fuel combustion is the large amount of O_2 required, which is very energy consuming and expensive to produce.

Pre-combustion

As the name indicates, the pre-combustion route captures CO_2 before the combustor by separating it from a synthesis gas mixture (H_2/CO). The fossil fuel is mainly converted to CO and H_2 by gasification, partial oxidation or reforming. CO is reacted with

steam and catalytically converted to CO_2 and more H_2 in a water gas shift (WGS) step. CO_2 is then separated from hydrogen by chemical or physical absorption, membranes or pressure swing adsorption. The advantage of doing the separation before the combustor relates to the much higher partial pressure of carbon dioxide obtained compared to post-combustion, hence reducing the size of the equipment. This approach gives valuable hydrogen as product, as indicated on Figure 1.1, which in turn can be used to generate electricity in fuel cells. The flexibility of such a system, which can both produce electricity and hydrogen, is very useful as the ratio of produced hydrogen to electricity can be adjusted based on the demand.

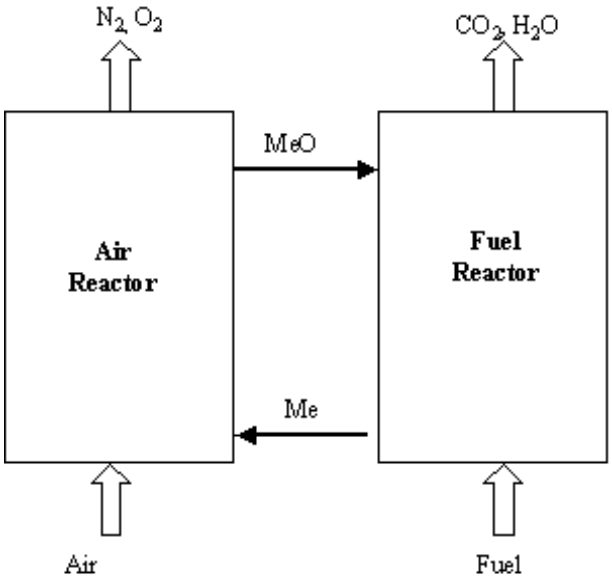

Figure 1.2: The process of chemical looping combustion [9].

In addition to the mentioned CO_2-free energy production routes there are novel concepts emerging, which cannot easily be categorized into the above groups. Chemical looping combustion (CLC) is a novel method for facilitating CO_2 separation from flue gases [10]. The process is composed of two fluidized reactors, an air and a fuel reactor, as shown in Figure 1.2. The fuel is introduced to the fuel reactor in a gaseous form where it reacts with an oxygen carrier to CO_2 and H_2O. The reduced oxygen carrier is transported to the air reactor, where it is oxidized back to its original state by air [9]. As for the oxy-fuel combustion process, NO_x formation is eliminated as oxygen is supplied to the combustor in the form of a metal oxide without any nitrogen present,

also giving pure CO_2 out. The principle of the CLC process is the same as for the oxy-fuel process, where pure oxygen is supplied to the combustor, and it has the same absorption-regeneration nature of post-combustion.

Carbon can also be transferred between two reactors, and in another novel concept CaO is used for capturing CO_2 from the flue gas at elevated temperatures (typically ∼600°C), and the carbonate formed is regenerated in the calciner at ∼900°C [11, 12]. High temperature separation of CO_2 has the advantage of efficient heat recovery from regeneration, compared to low-temperature absorption or adsorption systems. The major limitation of this concept is that the reactivity of CaO is reduced significantly with the number of carbonation-calcination cycles [13].

1.1.3 Carbon capture and storage (CCS)

Figure 1.1 shows the different routes to separation of CO_2 from fossil fuels, but does not indicate how it can be stored and secured from reaching the atmosphere. Efforts made to capture and separate CO_2 from flue gases in efficient ways are worthless unless it can be stored on a permanent basis.

CO_2 can be stored in geologic formations, e.g. deep coal seams, depleted oil and gas reservoirs, salt domes, the ocean or aquifers [14]. Once injected into a geological formation for storage, physical trapping blocks upward migration of CO_2 caused by an impermeable layer, known as the "cap rock". Geological storage of CO_2 is ongoing in three industrial scale projects; the Sleipner project in the North Sea (operated by Statoil), the Weyburn project in Canada and the In Salah project in Algeria [5]. Re-injecting CO_2 into oil wells for enhanced oil recovery (EOR) and simultaneously store it underground is also a potential way of utilizing CO_2.

Mineral carbonation and industrial usage are other ways of utilizing the captured CO_2. Mineral carbonation refers to the fixation of CO_2 using alkaline and alkaline-earth oxides, such as MgO and CaO, which may be present in naturally occurring silicate rocks. For industrial use, CO_2 is considered a reactant and can be used for urea and methanol production. CO_2 can also be used in technological applications such as in beverages and fire extinguishers. However, industrial usage of CO_2 does not contribute to the net reduction of CO_2 as it in most industrial processes has storage times of only days or months, before it again will be emitted to the atmosphere. Table 1.1 shows typical cost ranges for the different components of CCS [5]. In most CCS systems,

Table 1.1: Cost ranges for CCS components [5]

CCS system component	**Cost range**	**Remarks**
Capture from coal or gas fired power plant	15-75 US$/tCO$_2$ net captured	Compared to the same plant without capture
Transportation	1-8 US$/tCO$_2$ net transported	Per 250 km pipeline or shipping 4-40 MtCO$_2$/year
Geological storage	0.5-8 US$/tCO$_2$ net injected	Excluding potential revenues from EOR
Geological storage: monitoring and verification	0.1-0.3 US$/tCO$_2$ net injected	Covers injection and monitoring

the cost of capture (including CO_2 compression) is the largest cost component. This is attributed to the dilute concentrations of CO_2 and the large volumes of gas to be treated. Each capture technology has its advantages, and different technologies will be applied for different power generation systems in the future, e.g. post-combustion capture will be the likely choice for retrofitting of existing power plants, while the pre-combustion approach, through hydrogen production, is an appealing choice to those seeking to "kick-start" the hydrogen economy.

1.2 Hydrogen as energy carrier

> *We even believed them when they said that "hydrogen was the Second Coming - limitless, pollution-free energy that will soon replace oil !". We spent so much money on our military to make sure we had access to oil that our schools were falling apart, making everyone grow up dumb and dumber - and therefore, no one realized that hydrogen was not even a fuel at all !*
>
> Michael Moore (in "Dude, where's my country ?")

It is a common misconception that hydrogen is a clean source of energy, with water being the only byproduct when burned. Although abundant in the universe, hydrogen in a pure state does not occur in nature and must be synthesized, and should therefore be considered as an energy *carrier*, not a *source*. As electricity has been an important energy carrier in the last century, and will continue to be so, hydrogen is predicted to become an important energy carrier in the future "hydrogen society".

1.2.1 Towards the hydrogen society

A hydrogen society, also referred to as a hydrogen economy, is one where hydrogen is the main energy carrier along with electricity [15]. Hydrogen would be produced from renewable energy sources (*renewables*) such as solar energy, wind power or hydro power through water electrolysis or from biomass. In a hydrogen economy, electricity and hydrogen would be produced in large quantities and used where fossil fuels are being used today. Hydrogen is widely considered to be the transportation fuel of the future [8], and fuel cells are likely to replace energy inefficient combustion engines with time. It is obvious that fuel cell driven cars cannot be introduced to a market without any infrastructure for hydrogen supply in place. On the other side, a hydrogen infrastructure is worthless if the cost of hydrogen vehicles are too high for the customers to buy. It is a classical "chicken-egg" problem. Therefore, among the major short term challenges is to develop a hydrogen infrastructure and cost efficient fuel cells.

Hydrogen from renewables will be introduced in long term perspective, as the fossil fuel age may peak in 50-100 years. Then, the cost of fossil fuel, with CO_2 capture and storage costs included, will increase making renewables competitive. Today, however, H_2 from renewables is significantly more expensive than H_2 from natural gas, oil and

coal [16]. Hydrogen production from fossil fuels with CO_2 capture is therefore likely to be the first step towards the hydrogen economy.

1.2.2 Hydrogen from fossil fuels

Hydrogen can be synthesized from various fossil feed stocks through several reaction routes, and hydrogen production routes from natural gas (NG) are considered in this chapter. Natural gas is relatively abundant around the world and large pipeline systems are available within and from developed countries. In addition there is a large international trade of liquefied natural gas (LNG). With the proven reserves and established distribution system, natural gas is currently the most available primary fossil fuel for hydrogen production [17].

Table 1.2: Methane conversion routes

Process		$\Delta \mathbf{H}^0_{298}$ **[kJ/mole]**
Steam Methane Reforming (SMR)		
$CH_4(g) + H_2O(g) \leftrightarrow CO(g) + 3H_2(g)$	(1.1)	206
$CO(g) + H_2O(g) \leftrightarrow CO_2(g) + H_2(g)$	(1.2)	-41
$CH_4(g) + 2H_2O(g) \leftrightarrow CO_2(g) + 4H_2(g)$	(1.3)	165
Partial oxidation (POX)		
$CH_4(g) + 0.5O_2(g) \leftrightarrow CO(g) + 2H_2(g)$	(1.4)	-38

The chemical composition of natural gas varies according to the source, with the principal component being methane with small amounts of low molecular weight hydro-

carbons, nitrogen and CO_2. Small amounts of sulphur such as H_2S, COS or other organic sulphur compounds are also usually present in NG, which have to be removed if the gas is to be used as feed gas for steam reforming, a natural gas conversion route discussed later in this section, due to its poisonous effect on the reforming catalysts. There are two main reaction routes for conversion of methane to synthesis gas, i.e. steam reforming and partial oxidation. The reactions are listed in Table 1.2.

Steam methane reforming (SMR)

Steam reforming is a mature technology, which has been used industrially for several decades since its early developments in 1926 [18]. The reforming reactions, Eqs. (1.1-1.3), are normally carried out at 700-900°C and 15-30 bar, with nickel supported on a metal oxide, e.g. Ni/Al_2O_3, as the most preferred catalyst due to its cost efficiency. Rhodium, which also is used for catalyzing reforming reactions, has a lower tendency towards coking than nickel systems, but is a much more expensive catalyst. Steam is normally introduced in excess of the stoichiometric requirement, with typical steam-to-carbon-ratios (S/C) of 2-5, to promote the reforming reactions and avoid carbon deposition on the catalyst. Carbon can be formed through direct decomposition of methane, Eq.(1.5), or by the Boudouard reaction in Eq.(1.6):

$$CH_4(g) \leftrightarrow 2H_2(g) + C(s) \tag{1.5}$$

$$2CO(g) \leftrightarrow CO_2(g) + C(s) \tag{1.6}$$

Conventional steam methane reforming is carried out in multiple fixed bed tubes placed in a furnace. Heat is supplied indirectly to the tubes by burning natural gas in the furnace.

Partial oxidation (POX)

Partial oxidation, Eq.(1.4), is a slightly exothermic reaction, which occurs when the oxygen-to-carbon ratio is less than required for total oxidation to CO_2 and steam. This reaction may be non-catalytic or use a catalyst for catalytic partial oxidation (CPO), typically nickel on a metal oxide support. Without a catalyst present a reaction temperature over 1000°C is required, hence increasing coke formation due to methane decomposition, Eq.(1.5), and the need of expensive construction material for the reactor.

By comparing Eq.(1.4) with Eq.(1.1) it can be seen that less hydrogen is produced per mole methane for the POX reaction.

Autothermal reforming (ATR)

Autothermal reforming is a combination of partial oxidation and steam reforming. By mixing fuel, air/oxygen and steam, the heat required for the endothermic steam reforming is supplied by heat generated from oxidation reactions, hence operating at thermal neutral conditions. This eliminates the need of external heat addition, used in conventional steam reforming, where heat is supplied indirectly by burning fuel outside the reactor in a furnace. However, it will require pure oxygen to be supplied to the reactor in order to avoid diluting the hydrogen with nitrogen from the air. At present, production of pure oxygen is both expensive and energy intensive, but ATR is likely to be more attractive in the future when stricter CO_2 emission regulations are established by law. Then, in a pre-combustion system, relatively pure CO_2 is obtained ready for storage without any additional purification step required downstream.

High purity hydrogen

Regardless of reforming technology, additional process units downstream are required to further increase the hydrogen yield and upgrade the product quality. Figure 1.3 shows a schematic drawing of the total process for production of high purity hydrogen.

The product gas from the reformer contains carbon monoxide at relative high concentrations, which is reduced by the water gas shift (WGS) reaction where CO is reacted with steam to produce carbon dioxide and additional hydrogen. This is often done in two stages; the high temperature shift (HTS) and the low temperature shift (LTS). Most HTS reactors operate at about 350-400°C, and the catalyst used is often Fe-Cr-based. The LTS converter enables increased hydrogen yield by further moving the water gas shift equilibrium in favour of H_2 at lower temperatures (∼200°C). Cu-based catalysts are often preferred here. After H_2O is removed from the WGS product gas by condensation, the primary diluent is carbon dioxide. CO_2 can be removed in many ways, where scrubbing with an appropriate amine solution, such as MEA, being commonly used in the industry [19]. Table 1.3 shows typical concentrations of the gas streams in Figure 1.3 from steam methane reforming (F_1) followed by WGS (F_2) and CO_2 amine scrubbing (F_3) [20].

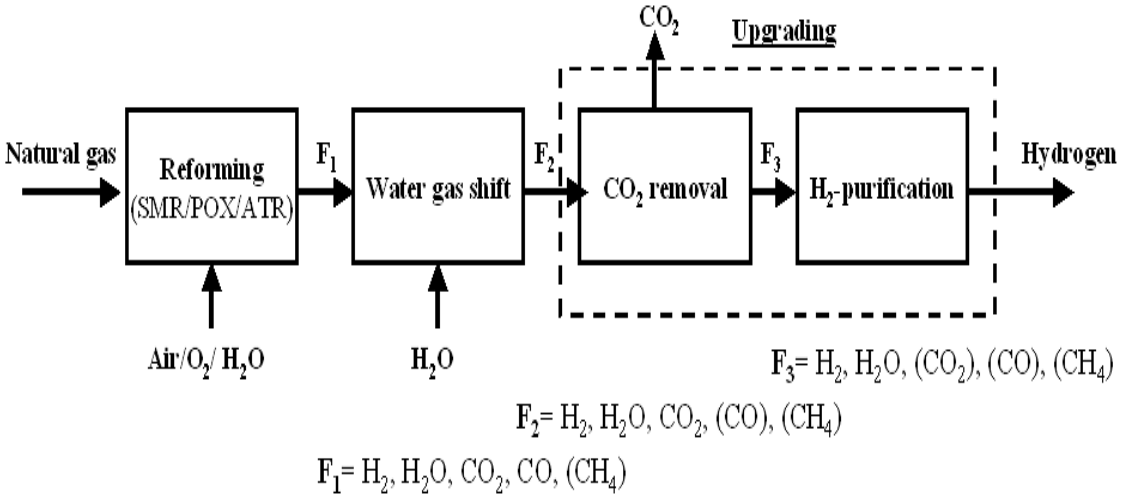

Figure 1.3: Process steps for high purity hydrogen production.

Table 1.3: Composition of gas streams in hydrogen production route [20]

Compound	$\mathbf{F}_1$ [**dry** %]	$\mathbf{F}_2$ [**dry** %]	$\mathbf{F}_3$ [**dry** %]
H_2	76	87.3	98.2
CO_2	10	10.7	0.01
CO	12	0.7	0.3
CH_4	1.3	1.3	1.5

Pressure swing adsorption (PSA) could also be used for obtaining high purity hydrogen. The PSA process reduces the number of units by replacing the LTS and CO_2 scrubber unit. The hydrogen purity is typically greater than 99%. However, there is a significant loss of hydrogen (∼20%) in the purge stream as a result of the countercurrent depressurization of impurities from the adsorbent. Other alternative separation processes, such as cryogenic fractionation and membrane separation, are currently not regarded competitive for industrial purpose. Figure 1.3 indicates a final purification step, and the process chosen is very dependent on the hydrogen purity requirement. If the hydrogen is used for combustion, this final step could be eliminated. However, if the hydrogen is to be used for a low temperature fuel cell application, a CO content lower than 50 ppm must be achieved. Methanation, selective oxidation or oxygen assisted water gas shift reaction are alternatives for reducing the CO content to this level.

1.3 Purpose

Novel concepts for hydrogen production from fossil fuels with CO_2 capture are emerging. Sorption-enhanced steam methane reforming (SE-SMR) is an example of such a concept. When a CO_2-acceptor (e.g. CaO) is mixed with a reforming catalyst, the CO_2 in the synthesis gas mixture is removed as soon as it is formed, causing the reforming and water gas shift reactions to proceed beyond the conventional thermodynamic limits. Moreover, when CO_2 is captured *in situ*, high purity CO_2 can be obtained from regeneration of the sorbent, eliminating costly separation steps downstream.

1.3.1 Thesis scope

Work related to SE-SMR to date, has mostly been conducted in small scale fixed bed reactors. However, fixed bed reactors are unlikely to be applied for the SE-SMR process on an industrial scale where continuous regeneration of sorbent is required. This work has been focusing on SE-SMR in fluidized bed reactors. Fluidized bed reactors are common in processes where catalysts must be continuously regenerated, and they also facilitate heat transfer, temperature uniformity and higher catalyst effectiveness factors. The "philosophy" behind this work has been to combine experimental work with modeling to obtain a detailed understanding of the continuous nature of the SE-SMR process in a fluidized bed reactor configuration. The results from experimental investigations of particle properties (micro model) are used as input for modeling of the fluidized bed reactor (macro model). The output from such a macro model can then be used for sensitivity analysis of the total process, and ultimately provide target values for sorbent properties, such as reaction rate and chemical stability, and be useful for the screening of new sorbents.

1.3.2 Thesis outline

The structure of the thesis can be related to the micro and macro scale of the process. *Chapter 2* contains a comprehensive literature overview of SE-SMR, covering sorbent characteristics and reactor concepts. *Chapter 3* deals with particle properties, such as kinetics, chemical and mechanical stability of the CO_2-acceptor. Also in this chapter, a carbonation rate expression is derived and kinetic parameters are found from fitting of experimental data. Arctic dolomite is the primary sorbent investigated, but potential

new synthetic sorbents for SE-SMR are also investigated, and this is discussed in this chapter. In *chapter 4*, a bubbling fluidized bed reactor is investigated and its feasibility as a reactor for SE-SMR is discussed based on experimental findings. *Chapter 5* deals with the whole process on a macro scale. Two interconnected bubbling fluidized beds are modeled using a two-phase bubbling bed model. Key parameters such as hydrogen purity, carbon capture efficiency and reformer efficiency are calculated from mole and energy balances. Experimentally derived carbonation kinetics, found in chapter 3, are used as input to the model. The major findings of the thesis are summarized in *chapter 6*, together with recommendations for future work.

1.3.3 List of publications

A list of international journal papers published during this work is presented below. The papers are found in Appendix D.

I Johnsen, K., Ryu, H-J., Grace, J.R., Lim, J. Sorption-enhanced steam reforming of methane in a fluidized bed reactor with dolomite as CO_2-acceptor, *Chemical Engineering Science*, 61:1195-1202, 2006

II Johnsen, K., Grace, J.R., Elnashaie, S.S.E.H., Kolbeinsen, L., Eriksen, D. Modeling of sorption-enhanced steam reforming in a dual fluidized bubbling bed reactor, *Industrial & Engineering Chemistry Research*, 45:4133-4144, 2006

III Johnsen, K., Grace, J.R. High-temperature attrition of sorbents and catalyst for sorption-enhanced steam methane reforming in fluidized bed reactors, submitted to Powder Technology

Paper I contains the results of the experimental work conducted at University of British Columbia in Vancouver during my five months stay at the Fluidization Research Center, Department of Chemical and Biological Engineering in 2004. Paper II contains modeling results from a dual fluidized bubbling bed reactor, and is a follow-up paper discussing reactor configuration and operational issues for the SE-SMR process.
Paper III considers mechanical attrition of sorbent and catalyst in fluidization environments, using a gas jet attrition test.

In addition to the journal papers, the following conference contributions have been made:

- Johnsen, K., Grace, J.R., Kolbeinsen, L. and Eriksen, D. Sorption-enhanced steam methane reforming in fluidized bed reactors, *AIChE Annual Meeting*, Cincinnati, 29th October-4th November 2005

- Johnsen, K., Meyer, J. and Yi, K.B. The selection, preparation and study of high temperature novel CO_2 sorbents for sorption-enhanced reforming, *8th International Conference on Greenhouse Gas Control Technologies*, Trondheim, 19th-22nd June 2006

Chapter 2

Sorption-enhanced steam methane reforming: An overview

Although steam methane reforming (SMR) is a mature technology that has been successfully used for decades in industrial large-scale hydrogen production, there are several aspects of the process that could be improved. Sorption-enhanced steam methane reforming (SE-SMR) represent a novel hydrogen production route that combines reaction and separation of CO_2 in a single step, breaking the thermodynamic limitation of conventional SMR. This chapter treats, in turn, methods for improving the SMR performance, thermodynamic analysis of SE-SMR, potential CO_2-acceptors for SE-SMR, and ends with reactor concept considerations.

2.1 Improving the SMR performance

During the last decades efforts have been made to make more efficient catalysts with higher reaction rates and increased resistance to carbon deposition. However, one of the major limitations is that the SMR reaction itself is limited by equilibrium conversion. There are currently a number of novel concepts for enhanced hydrogen production emerging in literature, that are based on shifting the equilibrium of conventional steam reforming to more favorable hydrogen yields.

2.1.1 Problems associated with conventional reforming

Conventional fixed bed reformers suffer from a number of limitations, making them inefficient [21, 22]. Improvements to the SMR process have been proposed in three major areas:

- Changing the reactor's operation from a fixed bed to a fluidized bed
- Changing the heat supply from external firing to direct heating
- Separation of one of the reaction products to drive the reaction beyond its thermodynamic equilibrium

In conventional steam reforming, the very endothermic reforming reaction is carried out in tubes layed out in a furnace. Heat is supplied to the tubes by burning natural gas in the furnace chamber. When heat is transferred from the furnace to the catalyst, the outer sections of the packed bed tend to insulate the inner sections, making the heat transfer inefficient. The catalyst is therefore packed in long narrow tubes of very costly superalloys, which contributes to increased production cost of hydrogen. In order to avoid excessive pressure drop along the fixed bed reformer tubes, relatively large catalyst pellets are used, causing catalyst intraparticle diffusion limitations. Elnashaie and Adris [23] were the first to propose the use of a bubbling fluidized bed steam reformer using a powdered catalyst, in order to overcome the diffusional limitations of the catalyst pellets. Fluidized beds offer good heat transfer between particles and the fluidizing gas, caused by the circulation of solids acting as internal heat carrier in the bed. Moreover, fluidized beds are excellent reactors for *in situ* oxidation of methane, providing heat for endothermic reforming reactions. Roy et al. [24] demonstrated that oxygen can be successfully introduced to a reforming fluidized bed providing the endothermic heat of reaction.

One of the most serious constraints of SMR relates to conversion of methane, which is limited by the thermodynamic equilibrium of the reversible reactions. For fixed bed reformers, reaction temperature has to be in the region of 800-900°C to achieve complete conversion of methane. At this elevated temperature the catalyst suffers deactivation due to carbon formation, also resulting in blockage of reformer tubes and increased pressure drops [25]. The thermodynamic equilibrium can be shifted to give more favorable yields at lower temperatures by removing either hydrogen or carbon dioxide.

2.1.2 Membrane enhancement

According to Le Chatelier's principle, the conversion of a reactant is increased when one of the reaction products is selectively removed from the gas mixture. Pure hydrogen can be extracted from the reformer reactor by perm-selective membranes made of palladium or its alloys. Nazarkina and Kirichenko [26] were the first to investigate the membrane selective separation technique for the reforming reactions. They used a fixed bed configuration with a palladium alloy as H_2-selective membrane at a reaction temperature of 700°C. The results showed a considerable shift in the thermodynamic equilibrium towards high reaction conversions, and very pure hydrogen was obtained on the membrane side. During the early 1990's, Adris et al. [27] investigated a fluidized bed reactor with immersed composite hydrogen perm-selective membranes, as a second generation fluidized bed reformer for further enhancement of the reforming reactions. Adris and Adris et al. further studied, validated and patented the Fluidized Bed Membrane Reformer (FBMR) after building a pilot plant and undertaking experimental and modeling studies of the system [28, 29, 30].

2.1.3 Sorption enhancement

Another way of shifting the equilibrium is by adding a CO_2-acceptor to the reactor, capturing carbon dioxide as it is formed, e.g. by CaO:

$$CaO(s) + CO_2(g) \leftrightarrow CaCO_3(s) \qquad \Delta H^0_{298} = -178\ kJ/mole \tag{2.1}$$

Carbon dioxide is then converted to a solid carbonate, shifting the reversible reforming, Eq.(1.1), and water gas shift, Eq.(1.2), reactions beyond their conventional thermodynamic limits. In this concept, catalyst and sorbent are mixed in the reformer, where sorption-enhanced steam reforming is performed. The combined chemical reactions are approximately thermally neutral. The product gas from the reformer mainly consists of H_2 and H_2O, with minor quantities of CO, CO_2 and unconverted CH_4. Carbonated sorbent is transferred to the regenerator where heat is supplied for the endothermic calcination reaction. Regeneration of the sorbent releases relatively pure CO_2 suitable for storage. A schematic illustration of a continuous SE-SMR process based on parallel fluidized bed reactors appears in Figure 2.1. A make-up stream of fresh sorbent must be included to maintain capture capacity. This addition could be to the calciner, with

withdrawal in the reformer, as indicated in Figure 2.1.

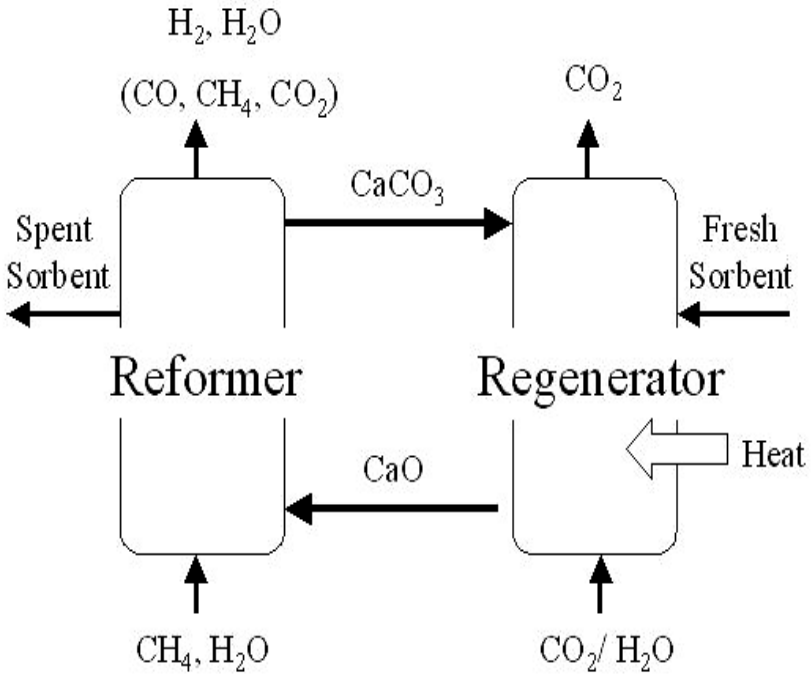

Figure 2.1: Simplified schematic of the sorption-enhanced SMR process.

The concept of a combined reaction and separation in hydrogen production is not new. Rostrup-Nielsen [31] reports that the first description of addition of a CO_2-acceptor to a hydrocarbon steam reforming reactor was published in 1868 (by Tessie du Motay and Marechal). In 1933, Williams [32] was granted a patent for a process in which steam and methane react in the presence of limestone and catalyst to produce hydrogen at a pressure in the range of 1 to 50 atm and temperatures of 300-550°C. This patent discusses a continuous process, where spent oxide is regenerated and sent back to the reactor for reforming and CO_2 removal, but limited data on the performance of the system is published. In 1963, Gorin and Retallick [33] patented a fluidized bed process using reforming catalyst and CO_2-acceptor. In their proposed reactor configuration, the catalyst is separated from the acceptor ($CaCO_3$) prior to regenerating the lime. The reaction vessel is divided into a hydrogen production zone and a regeneration zone, connected by a vertical standpipe. The reforming catalyst is packed as a fixed bed in such a way that interstices exist between the particles in order to make

acceptor particles circulate within the interstices. The catalyst particles ranged from 6.4 to 12.7 mm, while the acceptor particles ranged from 0.074 mm to 2.4 mm. The production zone is maintained at 760°C and 12.7 atm, while regeneration is accomplished at 925°C to 1100°C. Brun-Tsekhovoi et al. [34] described a similar process with continuous regeneration of a dolomite as CO_2-acceptor. The process was studied in a 0.1 m diameter fluidized bed reactor containing relatively large sized acceptor particles, facilitating separation from the catalyst. Pilot plant runs were conducted at 20 atm and temperatures around 600°C with catalyst and acceptor particles of 0.25 and 1.3 mm, respectively. A hydrogen content of 98% (dry basis) was reported, together with potential energy savings of about 20% compared to the conventional SMR process.

More recently, the sorption-enhanced reforming reaction and the use of calcium-based CO_2 sorbents has been demonstrated and intensively studied by a group at Louisiana State University (USA) resulting in several published papers [35, 36, 37, 38, 39, 40]. For example, Han and Harrison [35] used CaO to capture CO_2, overcoming the equilibrium limitation and achieving complete CO conversion. Dolomite was used as precursor and the combined shift and carbonation reactions were studied in a laboratory-scale fixed bed reactor. Balasubramanian et al. [39] added a calcium-based CO_2-acceptor to a commercial steam reforming catalyst producing >95% H_2 in a laboratory-scale fixed bed reactor. The effect of temperature, steam-to-carbon ratio, acceptor-to-catalyst ratio and feed gas flow rate were investigated. The combined reactions were sufficiently rapid above 550°C that equilibrium was closely approached at all reaction conditions studied.

Sorption enhancement can also be achieved with materials where an adsorption of CO_2 to form a weak bound to the adsorbent takes place. An example of such a type of material is hydrotalcite. For these materials to adsorb, a lower temperature must be applied, typically 400-450°C. Hufton et al. [41] have developed a novel concept called Sorption Enhanced Reaction Process (SERP) for hydrogen production, which uses a fixed packed column of an admixture of a SMR catalyst and a chemisorbent to remove carbon dioxide selectively from the reaction zone. Here the sorbent is periodically regenerated using the principle of pressure swing adsorption. The SERP process steps allow direct production of high-purity hydrogen (>95 mole%) at high methane to hydrogen conversion (>80%) with dilute methane (<5 mole%) and trace carbon oxide impurities (50 ppm) at a low temperature of 450°C.

2.2 Thermodynamic analysis

The advantages of combining chemical reaction and separation in one step can be understood from a thermodynamic analysis of the reactions, summarized below:

$$\text{Reforming: } CH_4(g) + H_2O(g) \leftrightarrow CO(g) + 3H_2(g) \tag{2.2}$$

$$\text{Shift: } CO(g) + H_2O(g) \leftrightarrow CO_2(g) + H_2(g) \tag{2.3}$$

$$\text{Carbonation: } CaO(s) + CO_2(g) \leftrightarrow CaCO_3(s) \tag{2.4}$$

$$\text{Overall: } CH_4(g) + 2H_2O(g) + CaO(s) \leftrightarrow CaCO_3(s) + 4H_2(g) \tag{2.5}$$

$$\text{Calcination/Regeneration: } CaCO_3(s) \leftrightarrow CaO(s) + CO_2(g) \tag{2.6}$$

A metal oxide, here CaO, is added to the reforming reactions, and the oxide will react with CO_2 and form a metal carbonate. CaO can also react with steam according to:

$$CaO(s) + H_2O(g) \leftrightarrow Ca(OH)_2(s) \tag{2.7}$$

However, the equilibrium partial pressure for H_2O equals 1 atm at ~450°C, and the hydration reaction is not thermodynamically favored at typical SE-SMR reaction condtions at atmospheric pressure.

Figure 2.2 shows the equilibrium hydrogen concentration as a function of reaction temperature at ambient pressure, a molar CaO/CH_4 ratio of 2, and a steam-to-carbon molar ratio (S/C) of 3. The predictions are calculated with the HSC thermodynamic software package (HSC Chemistry 5.1, Outokumpu Research Oy, Finland). The hydrogen concentration is predicted to reach a maximum of ~98 mole% at ~600°C, whereas the equilibrium concentration of conventional steam reforming is only ~74% at that temperature. The figure shows that sorption enhancement allows lower reaction temperatures, which may reduce catalyst coking and sintering, enabling use of less expensive reactor wall materials. In addition, the heat released by the exothermic carbonation reaction supplies most of the heat required by the endothermic reforming reaction. A H_2 concentration of more than 95% can be obtained for reaction temperatures in the range of 450-650°C, which makes the process rather flexible and insensitive to temperature fluctuations. Low reaction temperatures favor the water gas shift reaction, and low CO equilibrium concentrations. Yi and Harrison [40] operated at temperatures as

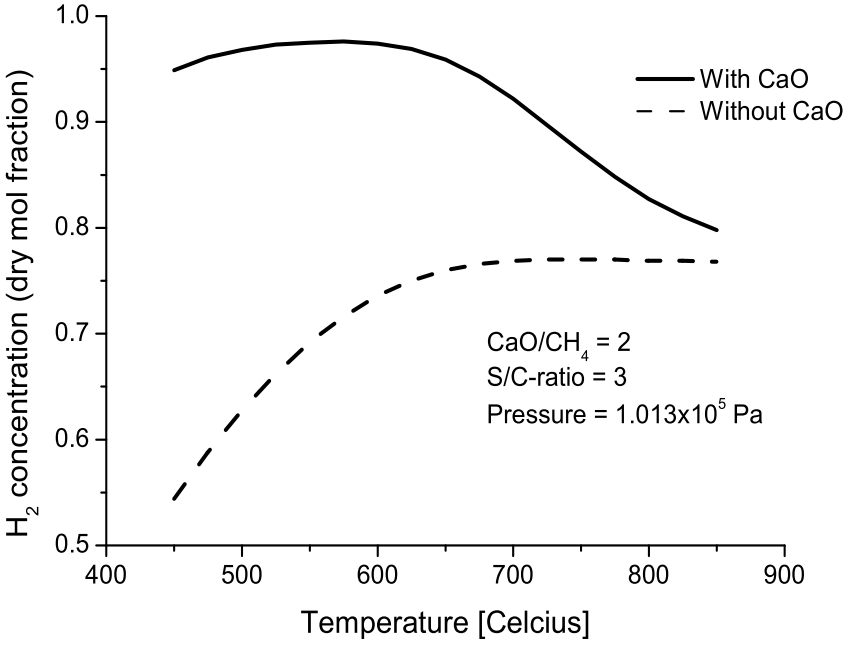

Figure 2.2: Hydrogen content at equilibrium as a function of temperature for a pressure of 1 atm, a S/C-ratio of 3 and a CaO/CH_4 molar ratio of 2 (calculated from HSC Chemistry 5.1, Outokumpu Research Oy).

low as 400-460°C producing 96 mole% H_2 and CO concentrations as low as 7 ppmv (dry basis), showing the potential of integrating an atmospheric PEM fuel cell with the SE-SMR process.

The hydrogen concentration drops at reaction temperatures above 650°C, due to the reverse calcination reaction. For pure CO_2, the decomposition temperature is ∼900°C, and calcination should therefore be performed in an inert atmosphere reducing the decomposition temperature. Figure 2.3 shows the equilibrium partial pressure of CO_2 as a function of calcination temperature, calculated from an equation proposed by Baker [42]:

$$P_{CO_2,eq} = \frac{1}{K_{CO_2,eq}} = 10^{7.079-\frac{8308}{T}} \qquad (atm) \tag{2.8}$$

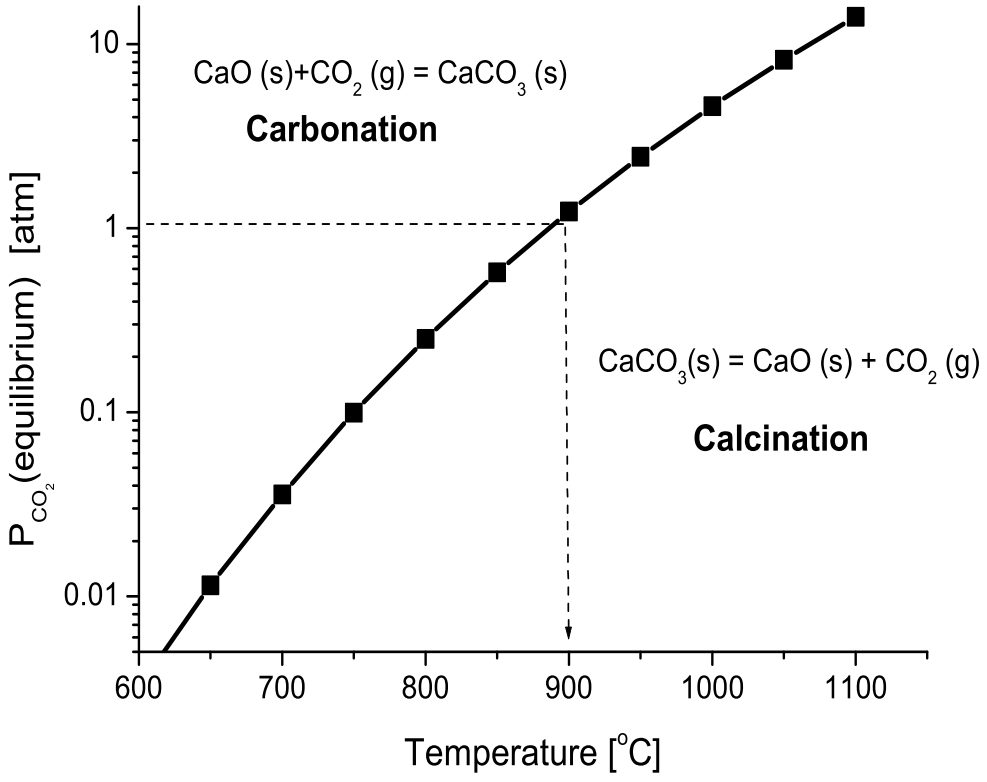

Figure 2.3: Equilibrium pressure of CO_2 over a $CaO/CaCO_3$-mixture as a function of temperature (based on an equation proposed by Baker [42]).

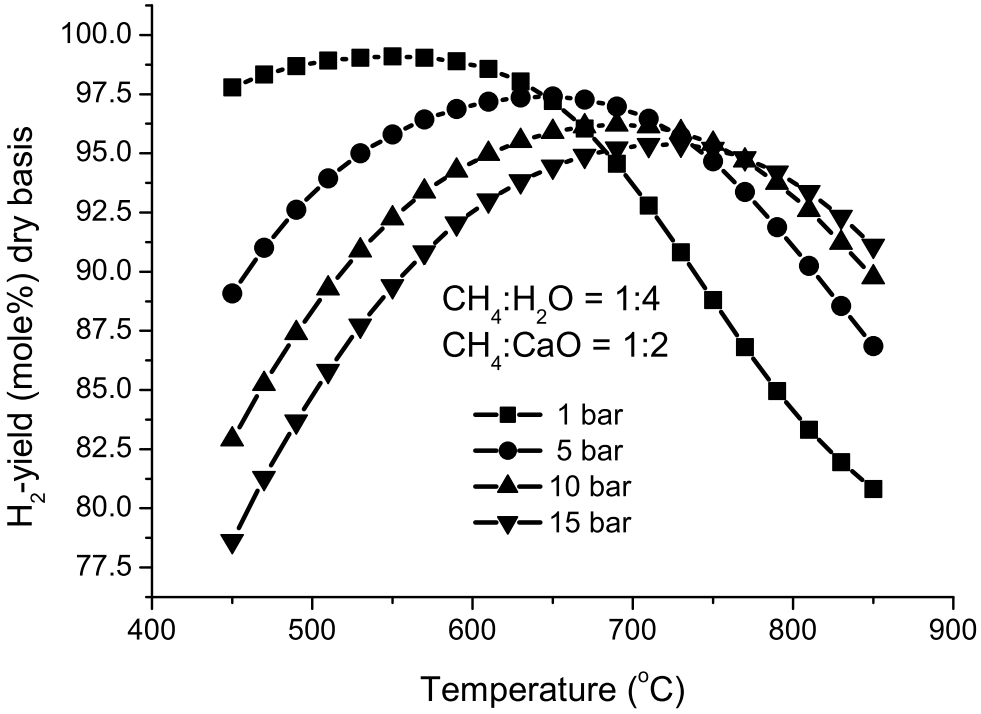

Figure 2.4: Hydrogen content at equilibrium as a function of temperature at different pressures, S/C=4, CH_4:CaO=1:2 (calculated from HSC Chemistry 5.1, Outokumpu Research Oy).

Figure 2.4 shows the variation of the H_2 concentration in the product gas as a function of the temperature at different pressures. The maximum H_2 concentration decreases as the pressure increases and it reaches values over 95% for pressures up to 15 bar. Moreover, the higher the pressure the higher is the temperature of the maximum H_2-yield point. From a thermodynamic point of view, operating the process at low pressure is advantageous for obtaining very high hydrogen concentrations ($> 98\%$) at relatively low temperatures. However, from a reaction kinetic point of view and the size of reactors, high-pressure operation is advantageous.

2.3 CO_2-acceptors

There are a number of criteria that should be fulfilled when evaluating potential sorbents for the SE-SMR process:

- High reaction rate (in the temperature range of 450-650°C)
- Sorbent stability
  - reversible CO_2 uptake/release
  - long term multi-cycle use
  - mechanical and thermal stability
- Small temperature gap between reaction and regeneration
  - energy saving
  - preventing thermal shock
- Low price and availability
- High sorption capacity

To date, no sorbents satisfy all these requirements. The sorbents that are mostly studied in the literature can be divided into natural and synthetic sorbents and are listed in Table 2.1. A detailed discussion on the different sorbents is provided in the following subsections.

2.3.1 Natural sorbents

Limestone and dolomite precursors are readily available world wide at low cost, and have been intensively studied because of their potential use for high temperature CO_2 capture and for SE-SMR, since proposed in the early works of Williams [32] and Gorin and Retallick [33]. A number of works, including Dedman and Owen [47], Bhatia and Perlmutter [48] and Silaban and Harrison [36], report that the carbonation reaction is rapid during the early stages, but undergoes an abrupt transition and becomes extremely slow before complete CaO conversion is achieved. Initial carbonation occurs preferentially near the exterior of the CaO particle and the surface porosity and permability may approach zero, thereby drastically reducing the rate at which CO_2 can reach unreacted CaO at the interior of the particle.

Table 2.1: Stoichiometric capacities and regeneration temperatures for various sorbents

Sorbent	**Stoich. capacity [g CO_2/g sorbent]**	**Regeneration temperature [°C]**
Limestone ($CaCO_3$)	0.79	900[a]
Dolomite ($CaCO_3 \times MgCO_3$)	0.46	900[a]
Huntite ($CaCO_3 \times 3MgCO_3$)	0.25	900[a]
Hydrotalcite	0.029 [b]	400 [c]
Lithium orthosilicate (Li_4SiO_4)	0.37	750[d]
Lithium zirconate (Li_2ZrO_3)	0.29	690 [e]
Sodium zirconate (Na_2ZrO_3)	0.24	790 [f]

[a] Temperature at which CO_2 equilibrium pressure is 1 bar [42]
[b] A capacity of 0.65 mole CO_2/kg, reported by Ding and Alpay [43]
[c] Regeneration is performed using pressure swing
[d] Reported by Essaki and Kato [44]
[e] Experimental findings of Yi and Eriksen [45] (regenerated in pure nitrogen)
[f] Experimental findings of L*ó*pez-Ortiz et al. [46] (regenerated in air)

The main problem associated with calcium-based absorbents is their rapid decay in capacity upon multiple re-carbonation. In principle, the pore volume created by the release of CO_2 during calcination should be sufficient to permit complete re-carbonation when the reaction is reversed. Sintering at high calcination temperatures tends to limit carbonation. Han and Harrison [35] report dolomite ($CaCO_3 \times MgCO_3$) as a superior sorbent compared to limestone, with higher achievable fractional conversion of CaO and better multi-cycle performance than that of limestone, although limestone has a greater CO_2 capacity per unit mass. The advantage of dolomite is attributed to the differences between the structural properties of calcined dolomite and calcined limestone. Initial calcination produces complete decomposition so that dolomite is converted to $CaO \times MgO$, while limestone is converted to CaO. Carbonation conditions were such that CaO, but not MgO, reacted with CO_2, and half-calcined dolomite ($CaCO_3 \times MgO$) was the product. The extra pore volume created by $MgCO_3$ decomposition is thought

to be responsible for the more favorable cycling performance. This stabilizing effect of inert MgO has been further studied by Bandi et al. [49], using other dolomite class minerals such as ankerite, barytocalcite, strontiantite and huntite. They found that the capacity losses after 45 cycles were approximately 60% for calcite, 40% for dolomite and less than 20% for huntite. In the case of huntite, each CO_2 absorption center (CaO) is surrounded by three MgO molecules, which do not participate in the absorption/desorption cycles but clearly attributes to improved multi-cycling capacity. The disadvantage of sorbents with large inactive parts is the increased energy demand for regeneration, as the inactive parts will be heated up during regeneration.

Abanades and Alvarez [13] have investigated the use of limestone as CO_2 regenerable sorbents by studying the maximum carbonation conversion during many carbonation/calcination cycles. In addition to their own data, they compared and reviewed previously published data from different sources. They found an unavoidable decay in activity that almost exclusively depended on the number of carbonation/calcination cycles, and to a lesser extent, on the reaction conditions. In additon, they found from some of the experimental series that the decay in conversion was much more rapid where severe sintering conditions were used during calcination. Silaban and Harrison [36] report that high temperature and presence of CO_2 in the calcination atmosphere affect the carbonation negatively. However, Ortiz and Harrison [38] report no significant difference in loss of multi-cycle durability for different regeneration atmospheres, using dolomite as sorbent, except when regeneration was carried out in pure nitrogen at 950°C.

Large quantities of limestone make-up are required in order to maintain capture capacity at an acceptable level, which can be justified to a certain extent due to the availability of low cost limestones. However, large make-up streams cause large amount of solid handling, therefore, attempts to improve multi-cycle durability have been made. For example, Salvador et al. [50] studied the use of Na_2CO_3 and NaCl to reactivate lime and enhance CO_2 capture in a fluidized bed combustor (FBC). Addition of both dopants failed to reactivate the CaO in the FBC environment, but doping with NaCl showed significant improvements in performance in a TGA reactor after several cycles. The reason for the different results in the two experimental set-ups is unclear. Also, according to the findings of Gullet and Bruce [51], a reaction pathway involving intermediate hydration would affect the chemical and physical properties of Ca-based sorbents. According to Kuramoto et al. [52], an intermediate hydration treatment was found to enhance the

reactivity and durability of Ca-based sorbents in their HyPr-RING process (hydrogen production by reactions integrated novel gasification). The presence of eutectics in the CaO-$Ca(OH)_2$-$CaCO_3$ ternary system was observed at elevated pressures at 923 and 973 K. Intermediate hydration was also carried out at atmospheric conditions, by a liquid-phsae hydration stage, where the sample was cooled to room temperature after calcination. This hydration step will, however, complicate the process layout.

Natural limestones and dolomites often contain trace amounts of sulphur, which is considered to be a severe catalyst poison. This calls for additional upstream process equipment for removing poisonous sulphur compounds before the sorbent is mixed with the catalyst, also complicating the process layout.

Also listed in Table 2.1 is the hydrotalcite (HTC), which is an anionic clay consisting of positively charged layers of metal oxide (or metal hydroxide) with inter-layers of anions, such as carbonate. The suitability of HTC as high-temperature CO_2 sorbent relates to the strong basic sites at the surface of the structure, which favors the adsorption of the acidic CO_2 according to the Lewis acid-base theory [53]. These materials capture carbon dioxide at a somewhat lower temperature than the metal oxides, at around 400°C, and regeneration is done at the same temperature using a pressure swing technique. Hydrotalcites are very stable under operation and do not lose capacity as CaO does, but the adsorption capacity is very poor, most likely restricting its potential as a sorbent on an industrial scale.

2.3.2 Synthetic sorbents

As limestones and dolomites fail to withstand numerous carbonation-calcination cycles, novel synthetic sorbents with potential high multi-cycle durability have become a subject of a number of recent investigations. Nakagawa and Ohashi [54] reported lithium zirconate (Li_2ZrO_3) as a promising sorbent capturing CO_2 over a temperature range of 450-550°C.

$$Li_2ZrO_3(s) + CO_2(g) \leftrightarrow Li_2CO_3(s) + ZrO_2(s) \qquad \Delta H^0_{298} = -163\ kJ/mole \quad (2.9)$$

Doping of lithium zirconate with sodium carbonate and/or potassium carbonate is reported to enhance the rate of reaction. This is attributed to the formation of an eutectic molten carbonate that reduces CO_2 diffusion resistance [55]. To date, the reported rate of reaction has been too slow to compete with calcium-based sorbents. However, efforts

are made to further increase the kinetics by modifying the preparation method. Yi and Eriksen [45] prepared Li_2ZrO_3 using a liquid based precipitation method, and found the CO_2 sorption rate to be ten times faster than for a solid-state preparation method. The precipitated Li_2ZrO_3 possessed a very small average aggregate size of 40 nm, which was believed to be responsible for the enhanced reaction rate. However, the reaction rate decreased significantly as the CO_2 partial pressure was reduced below 0.3 bar. Three absorption-desorption cycles were carried out, and both the reaction rate and the capacity were almost unchanged. Low reaction rates for Li_2ZrO_3 at low CO_2 partial pressures were also reported by Ochoa-Fernández et al. [56]. They simulated SE-SMR in a fixed bed reactor configuration using a reaction rate expression obtained from an oscillating microbalance. In addition to relatively slow reaction kinetics, lithium zirconate has the disadvantage of being a rather heavy material (low weight capacity) and also costly.

Kato and Nakagawa [57] studied a series of lithium silicates, as silicon dioxide (SiO_2) is an abundant material with light molecular weight. Replacing ZrO_2 with SiO_2 results in a reduced weight by 23%. The reversible reaction for CO_2 absorption by lithium orthosilicate (Li_4SiO_4) is described by the reaction:

$$Li_4SiO_4(s)+CO_2(g) \leftrightarrow Li_2SiO_3(s)+Li_2CO_3(s) \qquad \Delta H^0_{298} = -142\ kJ/mole \quad (2.10)$$

Kato et al. [58] claims lithium orthosilicate to be superior of lithium zirconate in terms of reaction rate, and report a reaction rate 30 times faster in 20% CO_2 at atmospheric pressure. Sodium-based sorbents are proposed as an alternative to the lithium sorbents. López-Ortiz et al. [46] compared the sorption rate of sodium zirconate (Na_2ZrO_3) to Li_4SiO_4 and Li_2ZrO_3 in a thermo gravimetric reactor at 600°C, and found Na_2ZrO_3 to have the highest reaction rate. However, regeneration was not easily achieved, which may limit the use of this sorbent for the SE-SMR process.

As the use of natural sorbents are limited by the loss of capacity upon multiple sorption-desorption steps, the introduction of synthetic sorbents seems to be mainly restricted by the reaction rate and cost. Different synthesis techniques are currently being investigated in order to "design" nano-sized particles with large surface areas. The cost of these sorbents will be dependent on both the compounds used and the preparation method. It is obvious that the cost of these sorbents will be significantly greater than for limestone and dolomite sorbents, and this will require them to sustain

$\sim$10,000 cycles to compete with natural sorbents [59]. At present, there are no multi-cycle data covering more than approximately 100 sorption-desorption cycles published.

Recently, a US company named Cabot Superior MicroPowders, claim they can synthesize artificial limestone and dolomite that do not degrade upon multi-cycling using a spray-based powder technique [60]. Unfortunately, there are very little experimental data published in the open literature yet on these synthetic calcium-based sorbents.

2.4 Reactor concepts

Interestingly, the original proposed patents and early works on sorption-enhanced reforming were based on fluidized bed reactors (e.g. Gorin and Retallick [33]), while recent experimental investigations have been conducted in small-scale fixed bed reactors. Useful data such as reaction rates, multi-cycle behavior and the effect of different operational parameters (e.g. S/C-ratios, sorbent-to-catalyst ratios, temperature etc.) on the combined reactions have been reported. However, fixed bed reactors will most likely not be applied for the SE-SMR process on an industrial scale where continuous regeneration of sorbent is required. For fixed beds to be applied, at least two reactors need to be operated alternatively and out of phase in reforming and sorbent regeneration modes. Synchronization of two reactors in different modes is likely to be very difficult as the sorbent capacity decreases with cycling, and there will be a mismatch between the production time and the regeneration time.

Several aspects of SE-SMR that have been extensively studied in fixed bed reactors in literature, like multi-cycle stability of sorbents, do not necessarily apply for fluidized beds. In a fixed bed batch reactor the whole sorbent should be utilized before switching to regeneration mode, while in a continuous system the degree of conversion will be dependent on solid residence time in the vessel. Moreover, the mechanical stability of the sorbent will important as fluidization will cause particle attrition and generation of fines.

2.4.1 Fluidized beds

Fluidized beds have a number of advantageous properties for industrial applications, such as good mixing of solids, good temperature control and transfer of particles between reactors making continuous operation possible. Some of these advantageous properties, relative to fixed bed reactors, are listed in Table 2.2. A possible reason for fixed beds being the predominant reactor configuration studied is that fluidized beds in general are considered a relatively immature reactor technology.

Fluidization occurs when solid particles are suspended in an upward flowing stream of fluid, which is either a liquid or a gas (only gas is considered here). A distributor plate distributes the gas evenly over the reactor cross section and at the same time acts as a support for the bed material. Fluidized beds can be operated in different flow regimes, e.g. in bubbling or fast fluidization, dependent on the velocity of the fluidizing

Table 2.2: Comparison of fluidized beds relative to fixed bed reactors [61]

Advantages relative to fixed beds	**Disadvantages relative to fixed beds**
Temperature uniformity (no hot spots)	Gas by-passing (limited gas-solid contacting)
Excellent bed-to-surface heat transfer	Substantial backmixing
Able to add/remove particles continuously	Attrition (wear/erosion)
Low pressure drops	Entrainment
Wide size distribution of particles	Design and scale-up are more complex

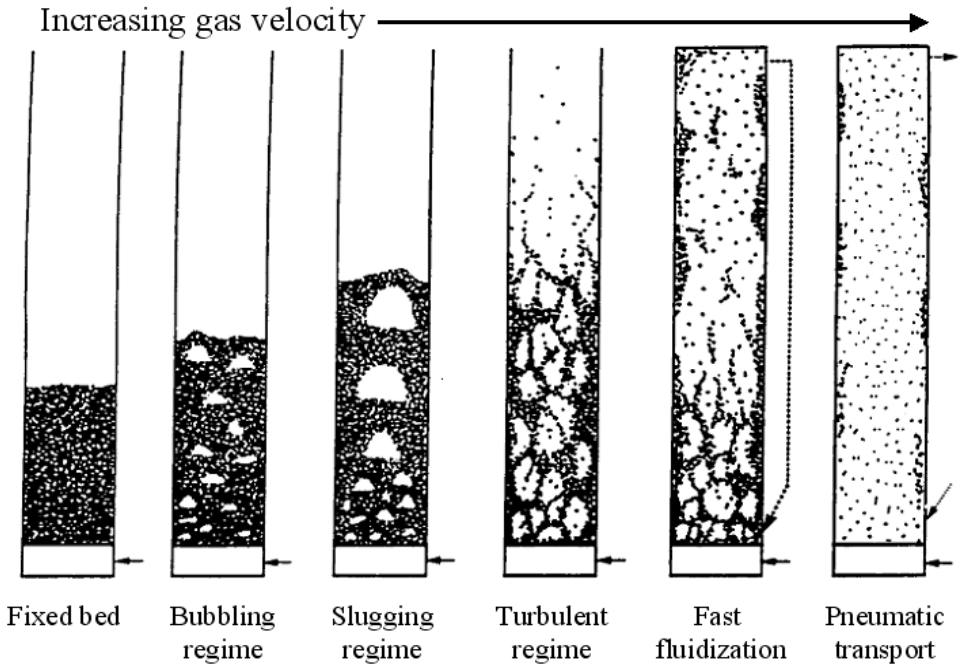

Figure 2.5: Fluidization regimes [62].

gas, as illustrated in Figure 2.5. The choice of operation conditions is dependent on the rate of reactions. For fast reactions, high-velocity fluidization, i.e. the fast fluidized regime is likely to be used. For slow reactions, operation in the low-velocity bubbling fluidization regime should be used. Both low and high velocity operations of fluidized beds can be conducted in a variety of reactor configurations [63].

Two potential fluidized bed reactor configurations have been identified for the SE-SMR process, shown in Figure 2.6. The dual bubbling bed configuration is inspired by

an early reactor configuration for fluid catalytic cracking (FCC) proposed by Exxon and described by Kunii and Levenspiel [64]. As highly active FCC catalysts were developed in the 1960s, upflow riser-crackers with higher gas throughputs replaced the bubbling bed reactor configuration.

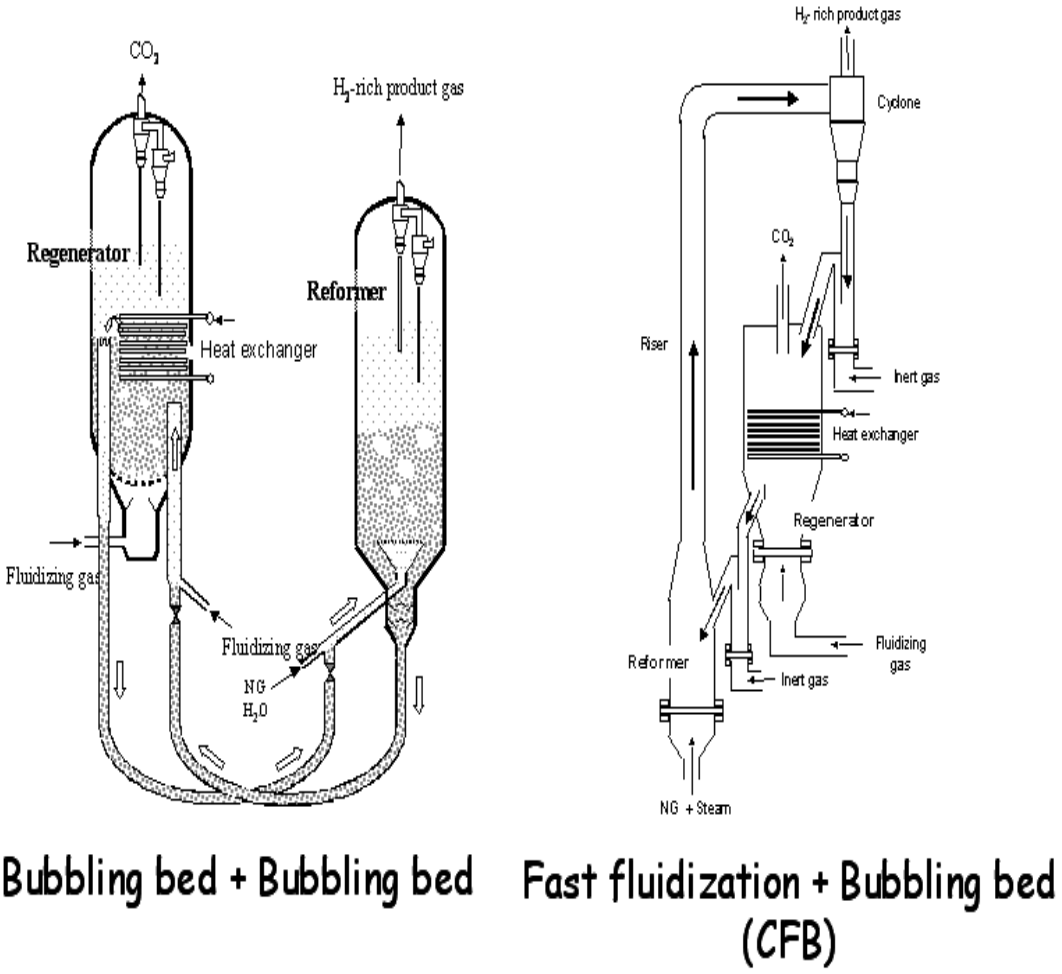

Figure 2.6: Proposed reactor configurations [64].

In the *bubbling bed-bubbling bed* configuration, solids are transferred between the reformer and regenerator/calciner by utilizing the difference in static pressure. The superficial gas velocity is kept at a moderate rate (typically 0.1-1 m/s) and both reactors are operating in the bubbling regime. In the other proposed reactor concept, the bubbling bed reformer is replaced by a riser. The *fast fluidized bed-bubbling bed* configuration is also referred to as a circulating fluidized bed (CFB). Here the gas ve-

locity is increased so that the particles are transported with the gas in the riser where reforming is occurring. The regenerator is also here a bubbling bed type of reactor. Typical gas velocities in the riser are in the range of 2-10 m/s. Therefore, the residence time in the riser is much lower than for the bubbling bed, requiring high reaction rate of reforming/carbonation. Moreover, the high velocity in the riser will also cause mechanical degradation of the particles by attrition. On the other hand, CFB reactors are relatively easy to operate and the gas throughput is much higher than for the bubbling bed. The choice of configuration should be made based on a number of criteria, and the most important ones are listed in Table 2.3.

Table 2.3: Comparison of reactor configurations

Parameters	**Bubbling bed-Bubbling bed**	**Fast fluidized bed-Bubbling bed**
Operation	Difficult	"Easy"
Attrition	Low	High
Gas throughput	Low	High
Reaction rate	Available at low reaction rate	High reaction rate required in riser

Another possible flow regime is turbulent fluidization. This regime is commonly considered to lie between bubbling fluidization and the fast fluidization regime [65], and has recently received increased attention because it combines high throughput with small interphase mass transfer resistance and manageable attrition. Typical gas velocities are in the range of 0.5-1.5 m/s.

Chapter 3

Sorbent investigation

High reaction rate in diluted CO_2 atmosphere, long term chemical and mechanical stability are important properties for potential CO_2-acceptors used in the SE-SMR process. First in this chapter, the chemical stability of Arctic dolomite, chosen as the primarty sorbent of investigation, is investigated by thermo gravimetric analysis (TGA) at various carbonation-calcination conditions. Furthermore, the mechanical stability with respect to generation of fines is investigated in an air jet attrition unit. Also, a rate expression, describing the rate of carbonation for the dolomite, has been developed based on a shrinking core model. In the closing section of the chapter, the multi-cycle performance of two novel synthetic sorbents, Li_2ZrO_3 and Na_2ZrO_3, are investigated and compared with the dolomite.

3.1 Multi-cycle tests

Arctic dolomite SHB, supplied by Franzefoss A/S, was chosen as the primary sorbent of investigation, due to the previously reported advantageous properties of dolomites in general [35]. In addition, X-ray diffraction (XRD) analysis indicated it being free of sulphur, eliminating the need for any pretreatment. Composition data of Arctic dolomite are given in Table 3.1.

3.1.1 Experimental

TGA was used to study carbonation/calcination of Arctic dolomite to evaluate its multi-cycle sorption properties. The principle of TGA is based on measuring the weight

Table 3.1: Analysis of Arctic dolomite, data from Franzefoss AS

Species	**CaO**	**MgO**	**SiO_2**	**Al_2O_3**	**Fe_2O_3**	**Na_2O**	**TiO_2**	**K_2O**	**Loss on ignition**
Conc. [wt%]	32	20.3	0.7	0.1	0.1	0.003	0.005	0.004	46.3

change of solids placed in a gaseous environment at the temperature under study, for a given length of time. For example, as calcined dolomite is put into a CO_2 atmosphere at temperatures ~500-650°C, carbonation of CaO will occur and the weight will increase as $CaCO_3$ is formed, registered by a micro-balance. The experimental set-up of the thermo gravimetric analyzer (TGA, CI electronics) is shown in Figure 3.1.

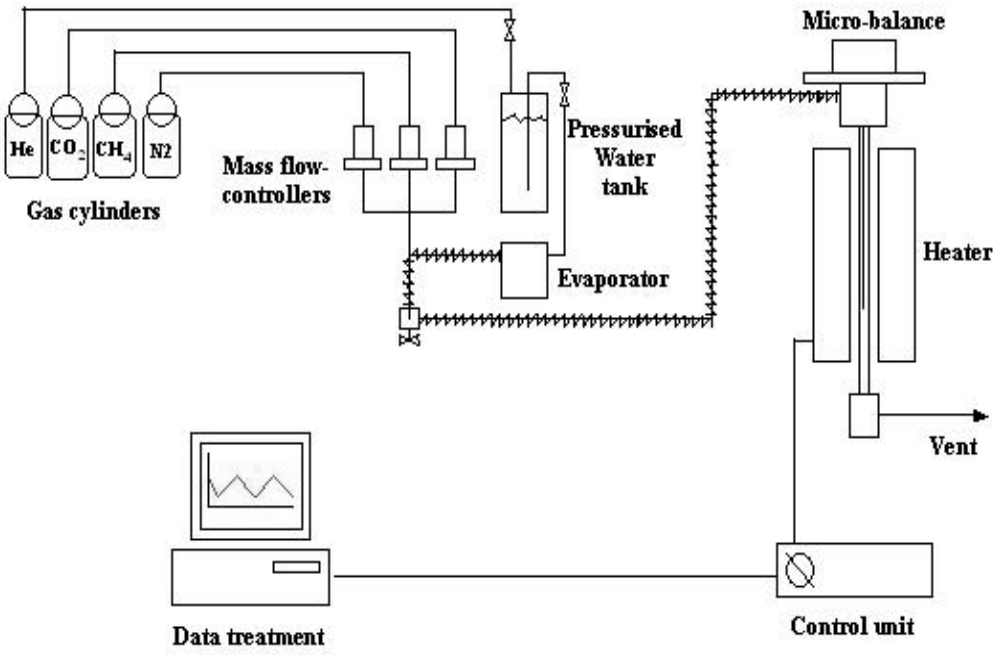

Figure 3.1: Experimental TGA set-up.

The TGA tests were initiated by heating the dolomite to 900°C in nitrogen for obtaining the calcined dolomite form (CaO×MgO), and then cooling down to the desired carbonation temperature. The flow rate of N_2 (99.99%) and CO_2 (99.9992%) were con-

trolled by mass flow controllers (Bronkhorst, EL-FLOW, Digital series). When steam was used the flow was controlled by a liquid flow controller (Bronkhorst, Liquid flow), and mixed with the gas flow in a controlled evaporation mixing system (Bronkhorst, CEM). The gas mixture entered the reactor at top and flowed downward over the solid sample, before it was vented at the bottom of the reactor.

Several multi-cycle runs using Arctic dolomite as sorbent have been performed. Table 3.2 lists the reaction conditions for all runs, and these tests are denoted *Dolo*. Dolo 1-3 are multi-cycle tests where carbonation and calcination time and atmosphere were varied. In Dolo 4 the effect of partial carbonation was investigated. A run with ten cycles, where the dolomite was exposed to 10% CO_2 for 80 minutes, was utilized as a reference case (Dolo 1). Next, a new batch of dolomite was placed in the TG reactor and exposed to 10% CO_2 for only 8 minutes (with 100% N_2 for the remaining 72 minutes in order to give the same total time of exposure) for the first 9 cycles, while for the 10th cycle the carbonation time was 80 minutes (referred to as Dolo 4a, where Dolo 4b is a reproduction test). The carbonation temperature was 600°C.

The following relationship has been used for calculating conversion of Arctic dolomite from thermo gravimetric data:

$$X_{CaO}(t) = \frac{\Delta w(t)}{w_0 \cdot \frac{Y_{CaO}}{Y_{Total}} \cdot (\frac{M_{CaCO_3}}{M_{CaO}} - 1)} = \frac{\Delta w(t)}{w_0 \cdot 0.472} \tag{3.1}$$

where $\Delta w(t)$ is the weight increase at any time, w_0 is the initial weight of calcined dolomite, Y_{CaO} is the CaO content in the dolomite (from Table 3.1), $Y_{Total} = \mathrm{Y}_{CaO} + \mathrm{Y}_{MgO} + \mathrm{Y}_{Impurities}$, M_{CaO} and M_{CaCO_3} are the molecular weights of CaO and $CaCO_3$ respectively.

3.1.2 Results and discussion

Effect of time of exposure

The results of the multi-cycle tests (Dolo 1-3) are presented in Figure 3.2. It can be seen that the rate of decay is different for the three reaction conditions employed.

Due to problems with the temperature program, the sample Dolo 2 was exposed to CO_2 at calcination conditions (925°C) for a period of 12 hours rather than 2 hours, at three stages during the 192 hours run. The sorbent will probably suffer great degradation at this elevated temperature due to sintering, which can explain the very rapid

Table 3.2: TGA experimental conditions for multi-cycle runs

		Carbonation			Calcination			
Sample ID	**D_p**	**Temp.**	**Atm.**	**Time**	**Temp.**	**Atm.**	**Time**	**Total Duration**
Dolo 1	100-200μm	600°C	10%CO_2 90% N_2	80 min.	850°C	100% N_2	80 min.	$\sim$ 46 h
Dolo 2	100-200μm	850°C	100%CO_2	180 min.	925°C	100% CO_2	120 min.	$\sim$ 192 h
Dolo 3	100-200μm	820°C	100%CO_2	20 min.	920°C	100% CO_2	20 min.	$\sim$ 50 h
Dolo 4a[a]	100-200μm	600°C	10%CO_2 90% N_2	8 min.[b]	850°C	100% N_2	80 min.	$\sim$ 46 h
Dolo 5[c]	100-200μm	820°C	100%CO_2	20 min.	920°C	50% N_2 50% H_2O	20 min.	$\sim$ 115 h
Dolo 6	100-200μm	820°C	100%CO_2	20 min.	920°C	50% CO_2 50% H_2O	20 min.	$\sim$ 70 h

[a] A reproduction is provided, denoted 4b
[b] Exposed to nitrogen for 72 minutes after carbonation, giving a total of 80 minutes at carbonation temperature (making comparison with Dolo 1 possible)
[c] Initial calcination in 50% H_2O/N_2 mixture

decay in capacity compared to the two other runs. It is also evident from Figure 3.2 that nitrogen for calcination has a positive effect on the sorbent stability for the first 8 cycles, where Dolo 1 has a greater conversion than Dolo 3. As the number of cycles is increased further, the sample Dolo 3 shows better resistance to loss of capacity. This can probably be explained by the difference of 60 minutes in calcination time at elevated temperature between the samples. Therefore, residence time rather than calcination atmosphere seems to be more critical when it comes to sintering and loss of sorption capacity. The total exposure time at elevated calcination temperatures seems to be critical for the lifetime of the sorbent. Abanades and Alvarez [13] claim the number of cycles to be the most important factor, which can be explained by the increased cumulative calcination time. However, from the above findings, their claim of reaction conditions to influence the decay to a lesser extent could only be true if the sorbents are calcined for the same amount of time.

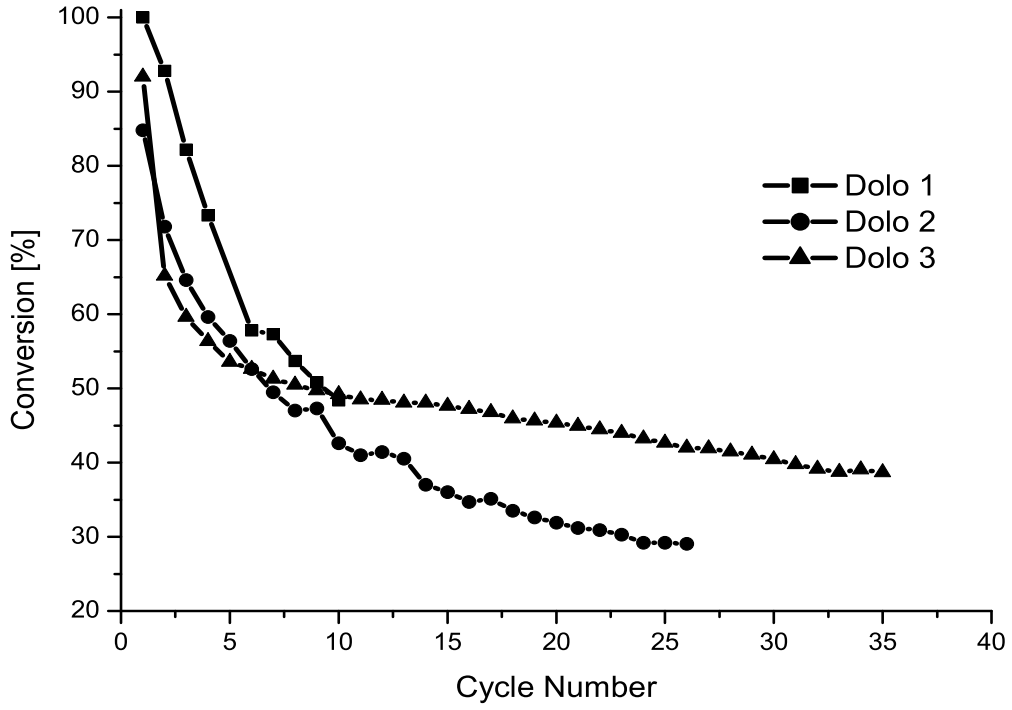

Figure 3.2: Conversion of dolomite as function of carbonation/calcination cycles.
Dolo 1(−■−): Carb.: 600°C, 10% CO_2. Calc.: 850°C, 100% N_2(80 min);
Dolo 2(− • −): Carb.: 850°C, 100% CO_2. Calc.: 925°C, 100% CO_2(120 min);
Dolo 3(−▲−): Carb.: 820°C, 100% CO_2. Calc.: 920°C, 100% CO_2 (20 min).

Effect of partial carbonation

In a continuous fluidized bed reformer-calciner system the degree of carbonation is very dependent on the circulation rate of solids. Therefore, it is interesting to investigate how partial carbonation affects multi-cycle conversion. The results from a test where only ∼30% of the sorbent was carbonated are shown in Figure 3.3.

The characteristic decay of conversion as a function of number of cycles is observed for the reference case Dolo 1, with a final conversion of 48.4% for the 10th cycle. For Dolo 4, where carbonation time was set to 8 minutes, a small decay in conversion is observed for the 9 first cycles. This is probably due to a somewhat slower reaction kinetics as the number of cycles is increased. When carbonation was allowed to proceed for 80

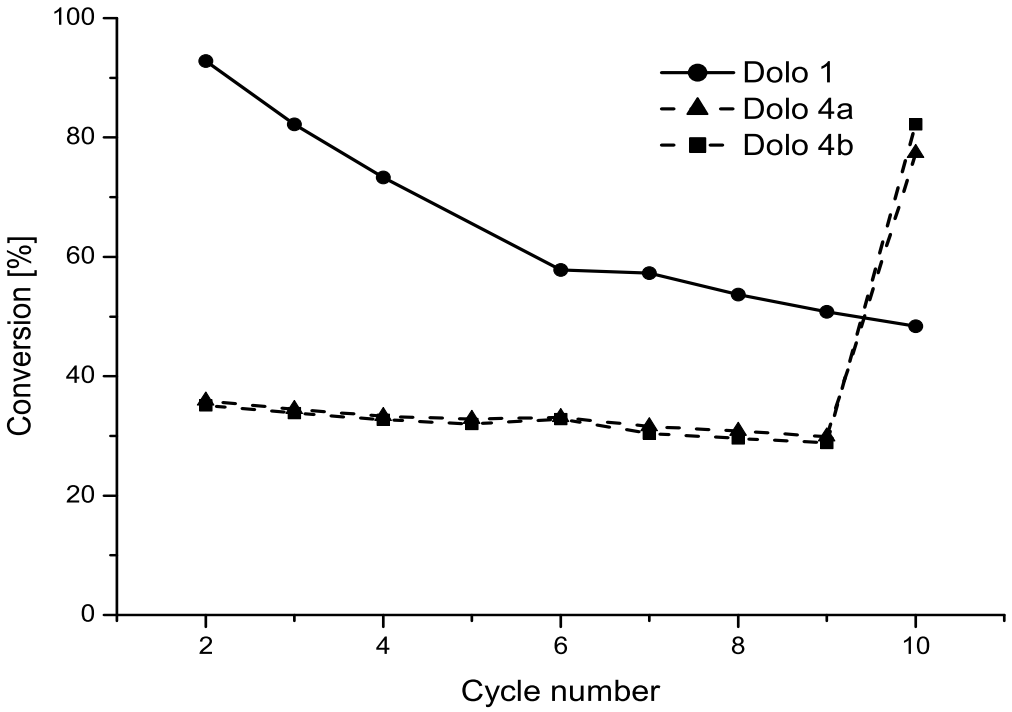

Figure 3.3: Effect of partial conversion on the multi-cycle capacity of dolomite. Carbonation at 600°C in 10% CO_2 for 80 min and 8 min for Dolo 1 and Dolo 4, respectively, for the 9 first cycles. Carbonation for 80 minutes in the 10th cycle for both Dolo 1 and Dolo 4. Calcination in pure N_2 at 850°C.

minutes in the 10th cycle, the CaO conversion increased to 77.4% and 82.2% for Dolo 4a and Dolo 4b respectively, which is significantly higher than the observed conversion of 44.8% of Dolo 1 after the same number of cycles. The sorbent conversion appears to be strongly dependent on the carbonation history of the sample, with partial carbonation of the sorbent being favorable for maintaining the sorption capacity. The reason for this may be attributed to structural properties of the dolomite, which experiences mechanical stress when alternating between the oxide and fully carbonated state, with very different molar densities. This finding is important when evaluating sorbents for circulating systems where circulation rates are relatively high, because it suggests that the sorbent can maintain its capacity much better, with partial carbonation, than if the whole sorbent is utilized.

The residence time of CaO, and then the degree of conversion, is dependent on the fluidization regime. For a reactor operated in the fast fluidization regime, a fractional CaO conversion as low as 1-2% has been reported based on modeling [66] using the kinetics of carbonation found by Bhatia and Perlmutter [48]. A bubbling fluidized bed configuration, with lower gas throughput, will reach higher solid conversions, but the residence time of solids will in any case be too short for complete conversion to be achieved. The chosen partial conversion of 30% is assumed to be representative for a bubbling fluidized bed.

Calcination atmosphere

The effect of different calcination atmospheres was studied. 100 cycles were performed for Dolo 5 with calcination in a mixture of steam and nitrogen, and the result is shown in Figure 3.4.

It can be seen that the degree of conversion drops dramatically during the first 20 cycles. However, the degree of conversion stabilizes at a value of ∼30% that remains throughout the run of 100 cycles. This means that addition of steam in the calcination step has a very positive effect on the multi-cycle capacity, when compared to calcination in pure nitrogen for Dolo 3. The "noisy" baseline of Figure 3.4 is caused by water condensation, which gave some fluctuations in the flow rate which again was registered by the micro balance. Calcination in a H_2O/N_2 atmosphere corresponds to heat supply by burning hydrogen in air in the regenerator. However, if pure CO_2 is to be obtained from the regenerator, calcination has to be performed in either H_2O or CO_2 itself. Therefore, nitrogen was replaced by CO_2 in the calcination atmosphere of Dolo 6, and a comparison is shown in Figure 3.5. Calcination in pure nitrogen, Dolo 3, served as a reference.

The multi-cycle tests were not performed for the same number of cycles, but the trends observed in Figure 3.5 are clear. There is a rapid drop in conversion for the first 20 cycles when steam is introduced compared to calcination in pure nitrogen. However, steam seems to stabilize the carbonation conversion level as the number of cycles are further increased for the H_2O/N_2 mixture, whereas the capacity for Dolo 3 is still decreasing after 35 cycles. However, when nitrogen is replaced by carbon dioxide the multi-cycle capacity is reduced to ∼18% after 60 cycles, and seems to be still decreasing. The presence of CO_2 in the calcination atmosphere has previously been reported by Silaban and Harrison [36] to affect the subsequent carbonation negatively,

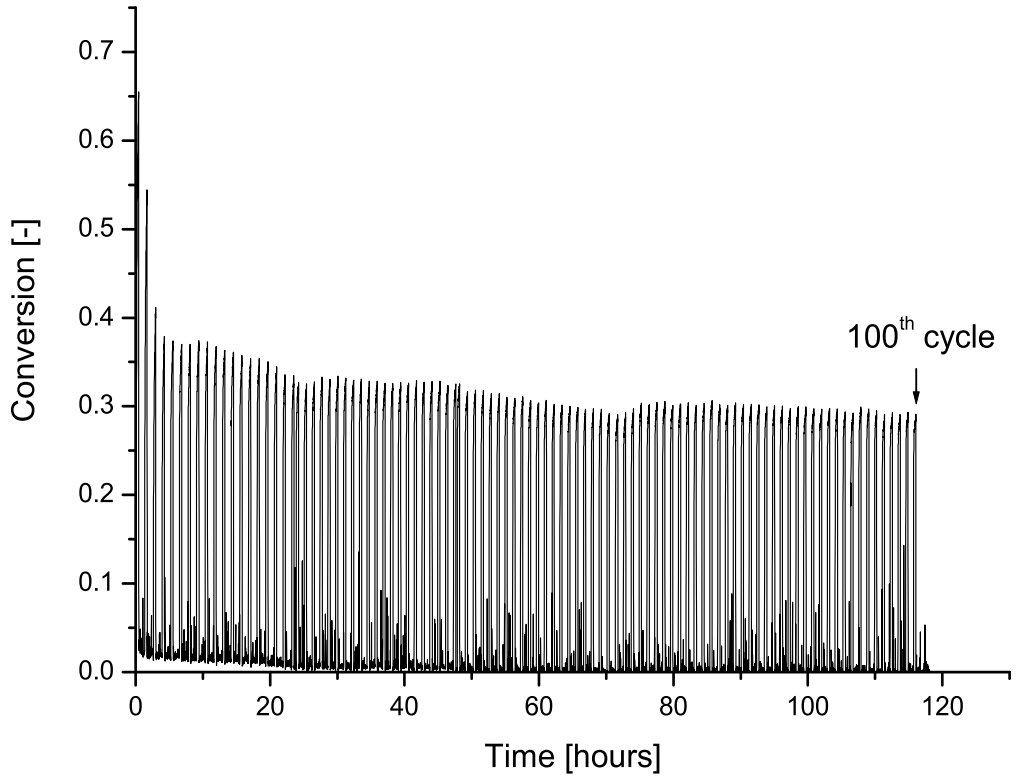

Figure 3.4: Multi-cycle conversion of Arctic dolomite. Carbonation: 100% CO_2 at 820°C, Calcination: 50% H_2O in nitrogen at 920°C.

due to enhanced sintering rates. They report that calcination should be carried out at the mildest possible conditions, i.e. in a nitrogen atmosphere at low temperatures.

It should be noticed that both the carbonation temperature (820°C) and the calcination temperature used here (920°C) are high. Also, the time of exposure at elevated temperature is high making the conditions rather severe. Still, after more than 100 hours of operation, a multi-cycle sorption capacity of ∼30% is achievable when calcined in a steam/nitrogen mixture. Calcination in pure steam was not performed as a carrier gas always needed to be present in the controlled evaporator mixing (CEM) unit. As previously discussed, this finding is valuable as the typical residence time of solids in a continuous reformer/regenerator system in any case might be too short for complete conversion to be reached. However, it will require additional energy to be supplied for

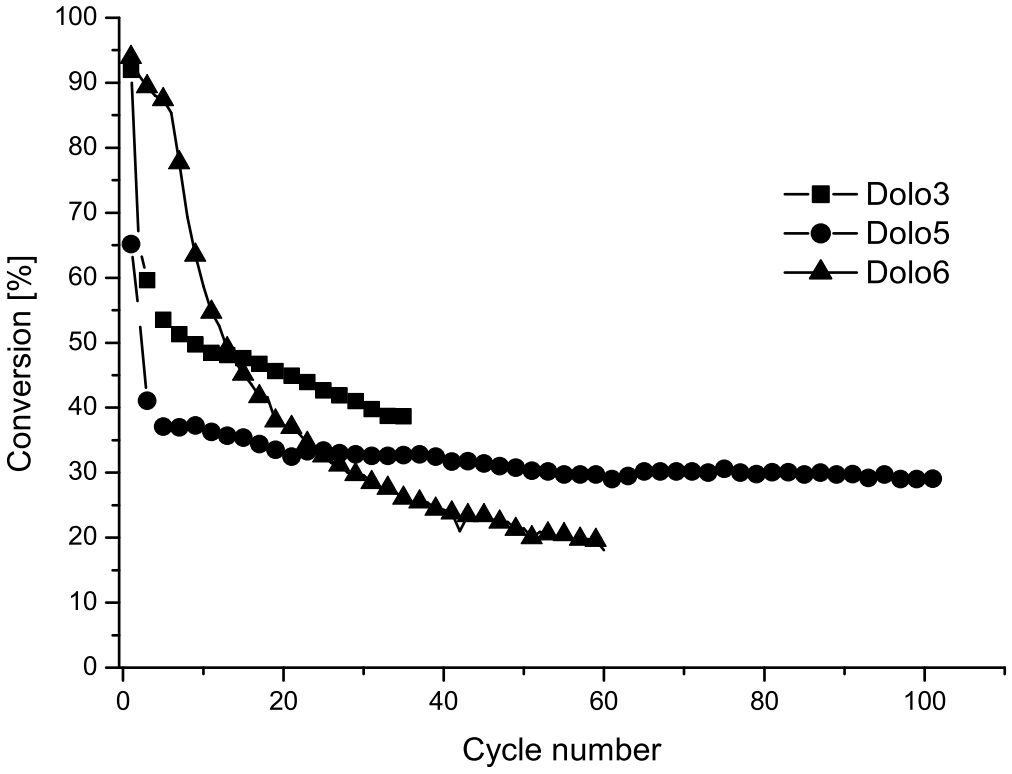

Figure 3.5: Conversion of dolomite as function of carbonation/calcination cycles. Dolo 3(−■−): Carbonation: 820°C, 100% CO_2. Calcination: 920°C, 100% CO_2; Dolo 5(− • −):Carbonation: 820°C, 100% CO_2. Calcination: 920°C, 50% N_2/H_2O; Dolo 6(−▲−): Carbonation: 820°C, 100% CO_2. Calcination: 920°C, 50% CO_2/H_2O.

heating of inactive sorbent.

The rate of carbonation as a function of cycles is shown in Figure 3.6. The final conversion after 20 minutes of carbonation decreases with cycle number. The rate of carbonation is, however, not significantly affected during the initial stage of carbonation as the number of cycles is increased. This is evident from the slope at the initial period. This also indicates that CO_2 only reacts with the outer region of the dolomite, as a surface reaction, and the interior of the dolomite becomes inaccessible due to pore blockage by the formed product layer. Although only 30% of the dolomite can be utilized for CO_2 capture, the fact that the reactivity is maintained in the presence of

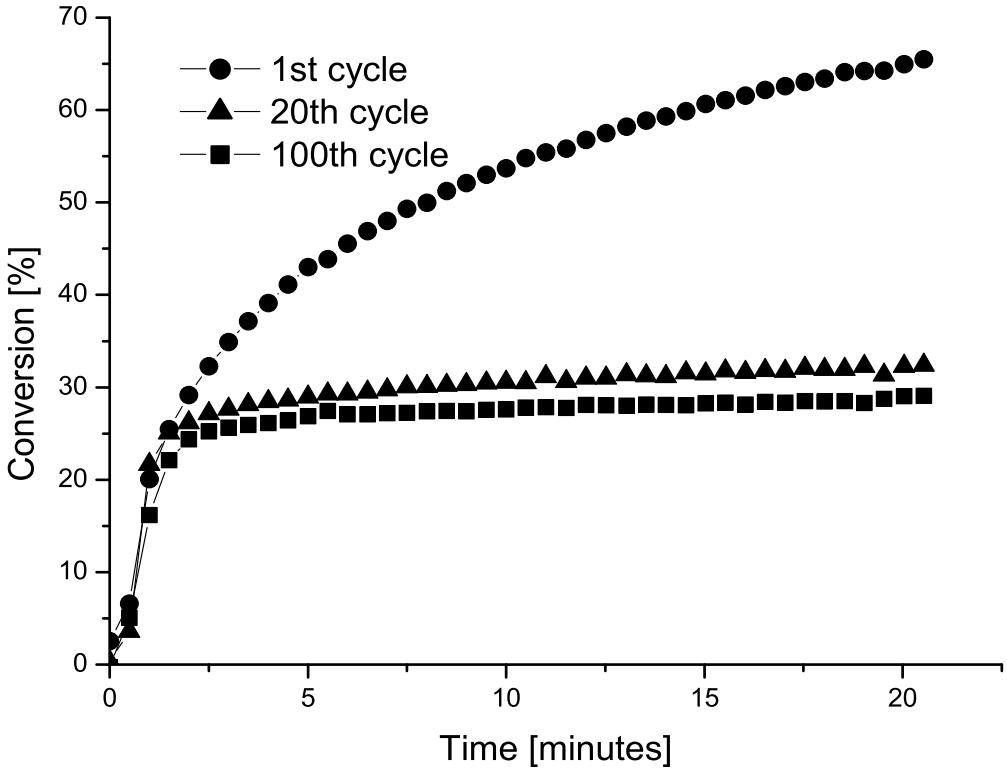

Figure 3.6: Rate of carbonation as function of cycle number for Dolo 5 (Carbonation: 820°C, 100% CO_2 for 20 min).

steam in the regeneration step makes the use of dolomite attractive and it should not be disregarded as a sorbent for the process of SE-SMR. Figure 3.7 shows SEM images of Dolo 5 after 100 cycles and dolomite after initial calcination in nitrogen. It is evident that the morphologies of the two samples are different. Calcined dolomite has a porous structur where grains can been seen, whereas Dolo 5 contains cracks and the presence of grains is not observed.

3.2 Attrition tests

One of the major disadvantages of fluidized beds relative to fixed beds is the generation of fines. In addition to chemical degradation, discussed in the previous section, there

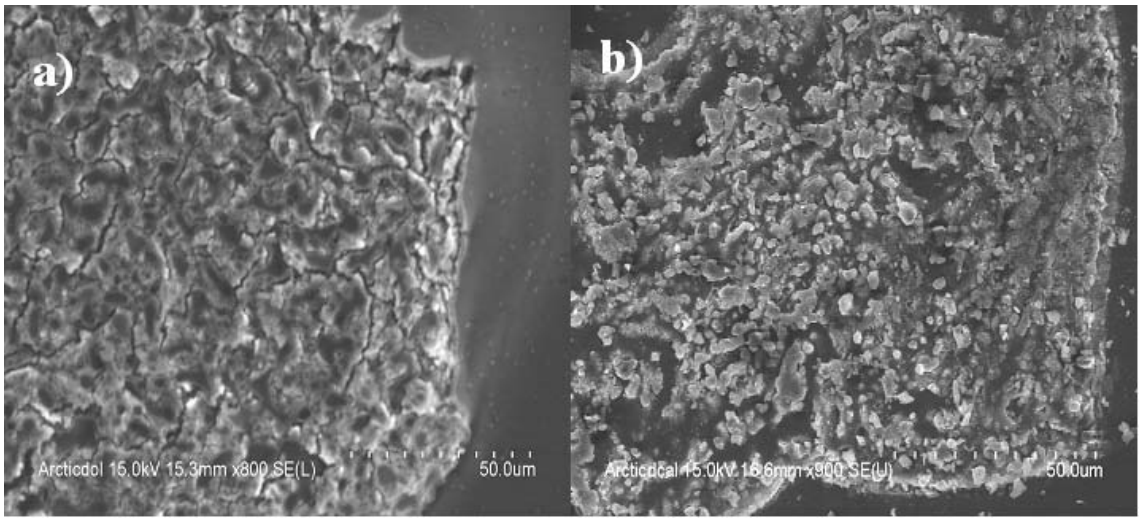

Figure 3.7: SEM image of; a) calcined dolomite after 100 cycles (Dolo 5), b) calcined dolomite after 1 cycle (calcined in nitrogen).

will be mechanical degradation due to attrition of solids caused by fluidization of the particles. The source of attrition is the mechanical motion between a particle and another body, which may be the wall of a container or another particle. The degree of attrition will be dependent on which fluidization regime one is operating in, with attrition increasing with increasing superficial gas velocity. The presence of baffles and internals will also cause increased attrition. A multitude of scenarios for fines generation from an individual particle can be conceived, and the mechanism can be discussed in terms of two extremes (illustrated in Figure 3.8):

- **Particle breakage**. The particle is broken up into smaller fragments due to the severe impact of the particle against a solid surface or other particles. These smaller fragments subsequently break down into increasingly smaller bits, into fines.

- **Abrasion**. In this case, particle wear is the result of the particle rubbing against other particles or a solid surface, eroding the particle at the outer surface. Fines are directly produced as a result of the erosion, and no fragments of intermediate size are produced.

In fluidized beds, the particles are normally required to remain in the bed for considerable periods. Attrition to smaller particle sizes will change fluidization properties

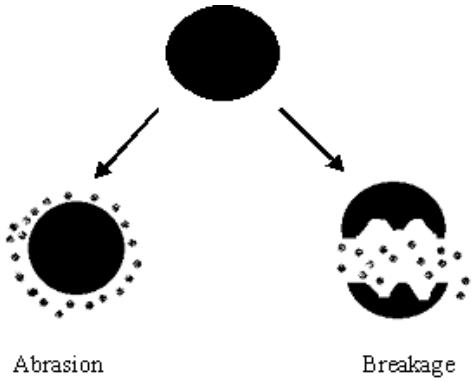

Figure 3.8: A schematic presentation of attrition through abrasion and breakage.

as well as causing loss of fines. This is of course a major problem when dealing with expensive catalysts, and significant loss of fines will constitute a major cost of operation. Bemrose and Bridgwater [67] sum up in which part of the fluidized bed attrition is most likely to occur. Within the bed, attrition will have the following sources:

- bubbling
- grid jets
- splashing of ejected particles

Some attrition will also occur when new particles are injected to the bed, due to thermal shock. It is also reported that the attrition rate is proportional to the difference between the superficial velocity and the minimum fluidization velocity (U-U_{mf}). Attrition has two major effects on fluidization processes:

i) Particle properties change as a result of attrition. Surface area, bulk density and particle size distribution are affected by attrition.

ii) Loss of material due to change of particle size will represent an additional process cost and may also cause a dust pollution problem.

A major concern about dolomites and limestones is the fact that the particles are relatively fragile, and co-fluidization with the much harder catalyst particles may cause additional attrition.

3.2.1 Experimental

The degree of attrition of both sorbent and catalyst was investigated using an Air Jet Attrition System, using the experimental facilities at MRT (Membrane Reactor Technologies Ltd., Vancouver, Canada). This attrition test unit is based on the standard D 5757 [68], a standard test method for determination of attrition of powdered catalysts by air jets. In a properly constructed air jet system the interaction between particles will be dominant. The test determines the relative attrition characteristics of powders by means of air jet attrition and intends to provide information about the ability of a powder to resist particle size reduction during use in a fluidized environment. The following definitions are used in describing particle attrition:

Fines Particles less than 20 μm are usually considered fines.

Air Jet Index (AJI) Unitless value that is numerically equal to the percent attrition loss after 5 hours; AJI=$\frac{M_{fines}}{M_{initial}}$

Recovery Defined as the percentage of total sample weight recovered;
Recovery=$\frac{M_{fines}+M_{rest}}{M_{initial}} \times 100\%$

Apparatus

The air jet attrition system consists of:

i) Stainless 710 mm long attrition tube with an inside diameter of 35 mm

ii) 3 nozzles with a diameter of 0.381 mm placed equidistant from each other, 10 mm from center

iii) Settling chamber, a 300 mm long cylinder with inner diameter of 110 mm and conical ends

iv) Fines collection assembly, filtering the fines from the gas

The overall arrangement of the attrition unit is shown in Figure 3.9.

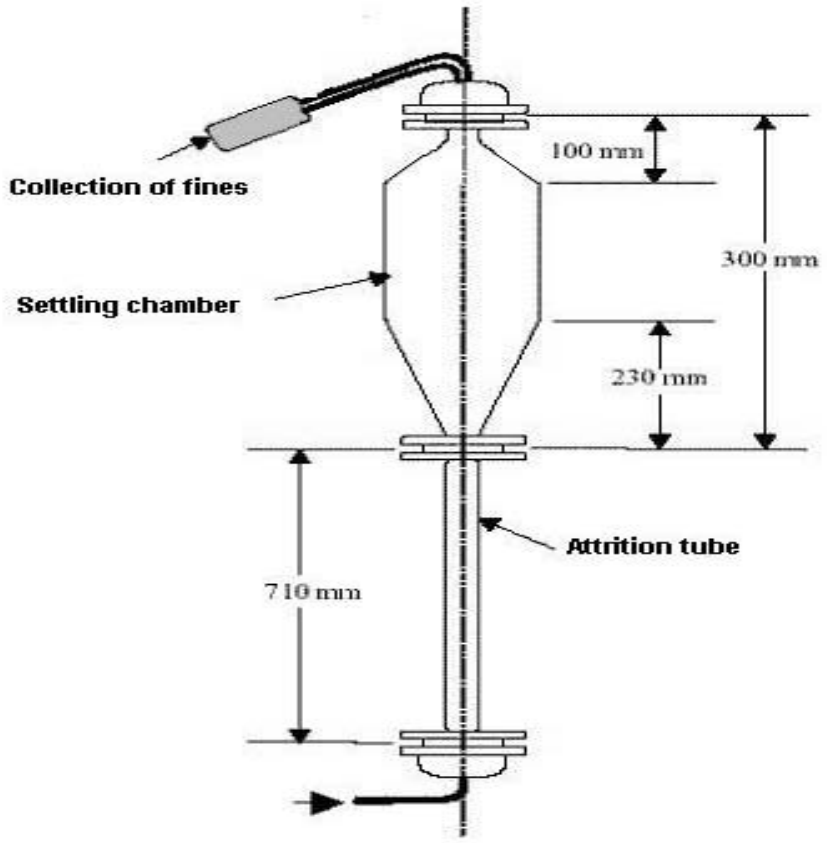

Figure 3.9: Air jet attrition apparatus.

Experimental plan

When the gas velocity in the settling chamber is greater than the terminal velocity for a given particle size, the particles will be transported to the fines collector. Both catalyst and sorbent attrition were evaluated. The superficial gas velocity in the settling chamber is calculated to be 0.052 m/s in pure nitrogen at 550°C. Terminal velocities for the particles at different sizes were calculated using the Ergun software (Ergun 6.0, Divergent S.A., France). For calcined dolomite, with an apparent density of 1560 kg/m^3, terminal velocities were found to be 0.015 m/s and 0.057 m/s for 20μm and 45 μm respectively. The terminal velocities of the catalyst, with an apparent density of 2200 kg/m^3, were calculated to be 0.017 m/s and 0.075 m/s for the same particle sizes. Therefore, it is evident that particle sizes somewhere between 20-45 μm will define the upper cut of the fraction leaving the settling chamber. It was desirable to conduct the

tests under realistic conditions, which will be as representative as possible for sorption-enhanced steam reforming. However, due to possible formation of hydroxides, which complicates weight calculations, pure nitrogen was used rather than steam at a gas flow rate of 10 L/min (STP). At this flow rate and with a back-pressure of 170-200 kPa, air jets are formed in the small orifices at choked flow conditions giving a gas jet velocity of ∼450 m/s. The calcined form of dolomite was used in all tests. The total sample weight was ∼50 g, particle sizes in the range of 45-180 μm and the tests were run for 5 hours before fines were collected and weighted. All experiments are listed in Table 3.3.

Table 3.3: Experimental conditions for Air jet attrition tests

Sample ID	**Particle type**	**Size range [μm]**	**Temperature [°C]**	**Atmosphere**
AJ-Dolo	Arctic dolomite	45-180	550	Nitrogen
AJ-Cat	Catalyst[a]	45-180	550	Nitrogen
AJ-Mix	Arctic dolomite/Catalyst[b]	45-180	550	Nitrogen
AJ-Lime	Limestone[c]	45-180	550	Nitrogen

[a] Reforming catalyst (Haldor Topsoe A/S, R-67-7H)
[b] A 50 wt% mixture of dolomite and catalyst
[c] Strassburg limestone (from the US)

3.2.2 Results and discussion

The percentage attrition loss after 5 hours, known as the Air Jet Index (AJI), is calculated from the elutriated fines to give a relative estimate of attrition resistance of the different samples. The index number is empirical and can only be applied under limited conditions of use and testing, but it provides a useful parameter for comparing different materials, or the same material in different environments. The results from the tests are listed in Table 3.4. There was some loss of solid material associated with disassembly of the attrition tube, but sample recoveries over 95% were obtained for all samples.

The dolomite showed the poorest resistance to attrition with a AJI value of 0.23, meaning that 23% of the initial sample was lost by generation of fines. A limestone (AJ-Lime) was also tested, and a significantly lower AJI value of 0.14 was found. From

Table 3.4: Results of air jet attrition tests

Sample ID	Initial weight [g]	Fines [g]	Rest [g]	Recovery [%]	AJI
AJ-Dolo	47.6	11.1	35.7	98.3	0.23
AJ-Cat	51.3	8.0	41.1	95.7	0.16
AJ-Mix	51.2	9.0	41.1	97.9	0.18
AJ-Lime	50.3	7.2	42.9	99.6	0.14

this test is seems like the limestone withstands a fluidization environment better than the dolomite. A possible explanation to this is that the initial decomposition of $MgCO_3$ and the creation of extra pore volume makes the dolomite more fragile than the limestone, partially nullifying the favorable multi-cycle properties of dolomites compared to limestones. However, it is hard to make any general conclusions based on the results from these two samples, as each limestone and dolomite is unique in terms of composition and structural properties.

The catalyst showed better resistance to attrition than the dolomite with an AJI value of 0.16. Still, the degree of loss of fines is significant, especially when taking the price of the catalyst into account. Loss of fines by attrition from natural cheap sorbents is more acceptable than loss of expensive catalyst. The catalyst tested was a commercial steam reforming catalyst from Haldor Topsoe, which is designed for fixed bed applications. Commercial Ni catalysts are not mechanically robust and are designed primarily for use in fixed bed reactors. This calls for developing catalysts that are suited for fluidized bed operation. The air jet attrition tests were conducted at a constant temperature of 550°C and the effect of temperature swing operation was not investigated. Alternating between carbonation and calcination will most likely cause thermal stress on the particles and increase the degree of attrition.

The AJ-Mix sample, where catalyst and dolomite were mixed, had an AJI value of 0.18. This value is between the AJI values of the pure compounds, indicating that co-fluidization of catalyst and dolomite will not lead to additional attrition. It must be emphasized that the AJI value does not say anything about the expected loss of fines in a real fluidization reactor, where fluidization regime of operation and the presence of internals will influence the degree of particle erosion.

3.3 Reaction rate

The non-catalytic gas-solid reaction between CaO and CO_2 is known to proceed through two rate-controlling regimes [48, 69, 70]. Initially, a rapid chemically controlled stage is rate determining, before the rate of reaction decreases due to diffusion limitations caused by the very slow diffusion through the product layer. This is illustrated for Arctic dolomite in Figure 3.10.

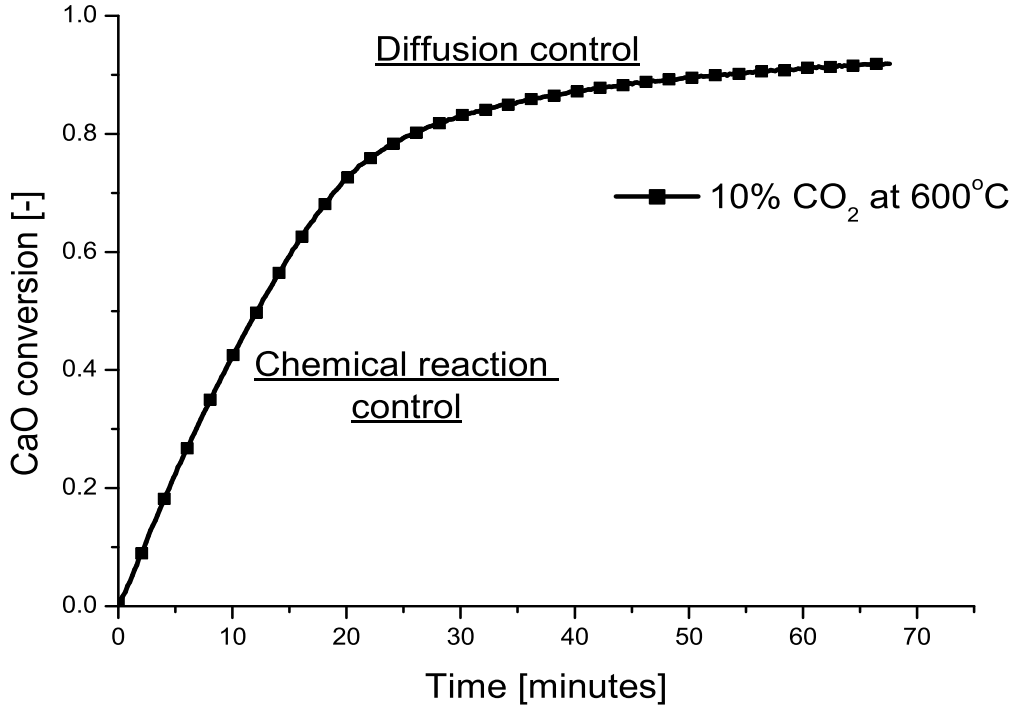

Figure 3.10: CaO conversion as a function of time for Arctic dolomite (Carbonation in 10% CO_2 at 600°C).

Interestingly, a number of previously published works on the reaction rate of carbonation are focusing on the slow product layer diffusion controlled regime [48, 71], which is unlikely to be utilized in an industrial application. Bhatia and Perlmutter [48] used a random pore model to describe the diffusion controlled stage and found activation energy to be 88.9±3.6 kJ/mole (for T<515°C) and 179.2±7 kJ/mole (for T>515°C)

for this region. While in the case of the rapid chemically controlled initial stage they report an activation energy of zero in the temperature range of 823-998 K.

Lee [69] proposes the simple rate expression:

$$\frac{dX}{dt} = k \times (1 - \frac{X}{X_U})^2 \tag{3.2}$$

where k is a kinetic rate constant, X is the conversion and X_U is the ultimate conversion. Experimental data from Bhatia and Perlmutter [48] and Gupta and Fan [70] were used to fit the apparent kinetic parameters in both the fast initial regime and the diffusion-controlled regime. For the chemically controlled regime activation energies of 72.2 kJ/mole and 72.7 kJ/mole were found, respectively, for the data from Bhatia and Perlmutter and Gupta and Fan.

Kyaw et al. [72] studied the reaction rate for both calcite and dolomite, and the rate of reaction was described by:

$$\frac{dX}{dt} = k_x \times (1 - X)^{\frac{2}{3}} \times (P - P_e)^n \tag{3.3}$$

where k_x is a reaction rate constant, X is conversion, P is pressure of CO_2 and P_e is equilibrium pressure of CO_2. They found the reaction order to be n=0.1, and activation energy of calcite and dolomite to be about 78 kJ/mole and 35 kJ/mole respectively. Dedman and Owen [47] report an apparent activation energy of 39.7 kJ/mole, using calcite as sorbent, in the temperature range of 200-600°C. However, they believe that the true activation energy is twice this value, i.e. 79.4 kJ/mole, due to intra-particle diffusion limitations.

The value of ultimate conversion reported in literature for calcium-based sorbents varies from 60-100%. This great variation is associated with the different morphology of the sorbents. Gupta and Fan [70] report the rate of carbonation in the diffusion controlled regime and the ultimate conversion both to be largely dependent on pore structure of the sorbent. Pore blockage and the build-up of a solid product layer make the reaction very slow, and complete conversion will not be achieved for some sorbents. Because of the unique morphology of different sorbents, rate expressions have to be developed for the specific sorbents. Using literature values, e.g. diffusion constants and activation energies, for prediction of the rate of reaction of other sorbents will most likely lead to huge errors. Therefore, a rate expression describing the rate of carbonation for Arctic dolomite has been developed.

3.3.1 Carbonation model

A model should predict conversion as a function of time matching real data without too many mathematical complexities. Different models for carbonation have been proposed in the literature, everything from the rather simple model of Lee, Eq.(3.2), to the more complex random pore model employed by Bhatia and Perlmutter [48] have been proposed. For non-catalytic reactions, two simple idealized models are widely used; the Progressive-Conversion Model (PCM) and the Shrinking unreacted-Core Model (SCM) [73].

The PCM model assumes that intra-particle diffusion is fast compared to chemical reaction, making a uniform reacting particle. It is well known that carbonation proceeds through a slow diffusional limited regime at higher conversion levels, making the PCM model not suitable for describing this regime. The classic SCM model assumes a sharp reaction front advancing from the exterior of the particle towards the center. A sharp boundary between the unreacted core and the product layer is an idealized situation, and the real situation is probably something in between the two reaction mechanisms.

Model choice

Scanning electron microscopy (SEM) with energy dispersive spectrometer (EDS) was found to be a convenient tool for analyzing the dolomite particles, in order to get an idea of which of the two previously mentioned models that is closest to reality for describing carbonation of calcined dolomite.

Calcined Arctic dolomite was first placed in a TG apparatus and exposed to 10% CO_2 in N_2 at 550°C for a period sufficiently long to observe a weight increase of the sample. The CO_2 flow was then stopped and the sample removed, and cross-sectional cuts of the partially carbonated dolomite particles were prepared for SEM/EDS analysis. Figure 3.11 shows the different positions chosen for EDS analysis. Position 1 was located in the center of the particle, while position 4 was located close to the exterior. The sample was coated with carbon, and oxygen concentration (rather than carbon) was used as indication of whether CO_2 had reacted with CaO. A typical EDS spectrum is shown in Figure 3.12. Every peak in the EDS spectrum was normalized to the highest intensity peak, and oxygen intensities at the different positions are listed in Table 3.5.

If carbon dioxide reacts with calcined dolomite throughout the whole particle, one will expect oxygen concentration to be equal at all points. If the reaction proceeds as a

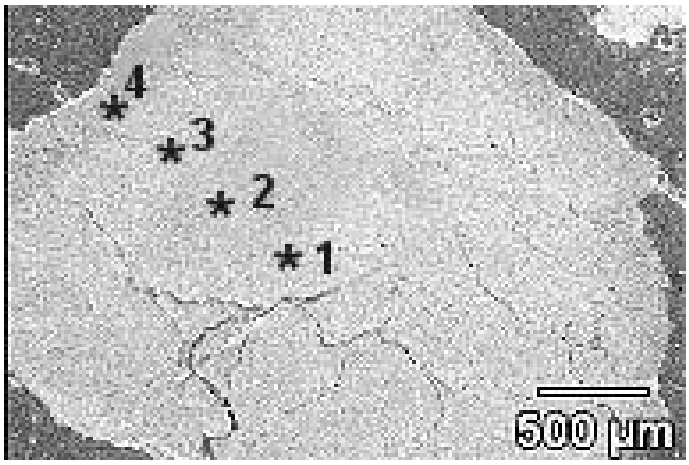

Figure 3.11: EDS analysis selection of partially carbonated Arctic dolomite.

Table 3.5: Normalized oxygen intensity from EDS analysis of Arctic dolomite

Position	Normalized oxygen intensity
1	0.2266
2	0.2212
3	0.2166
4	0.3922

shrinking unreacted core, there should be a lower concentration of oxygen at the interior for a partially carbonated particle. It can be seen from Table 3.5 that the oxygen content at position 1-3 is almost constant, while the intensity at position 4 is approximately twice the value of the previous points, indicating that CO_2 has not reacted uniformly throughout the particle. Oxygen will mainly be found as CaO and MgO in the unreacted core, while in the reacted product layer oxygen is present as $CaCO_3$ and MgO (MgO does not react with CO_2 at this high temperature). If the difference in oxygen content is related to the carbonation reaction, the oxygen ratio between carbonated dolomite and calcined dolomite should be approximately 2 (assuming equal quantities of Mg and Ca). The oxygen intensity at position 4 relative to the other positions is $\sim$1.8, supporting the assumption of CO_2 reacting with CaO at exterior of the particle first, leaving an unreacted core. From this observation, a shrinking core model is chosen for describing the reaction between carbon dioxide and calcined dolomite.

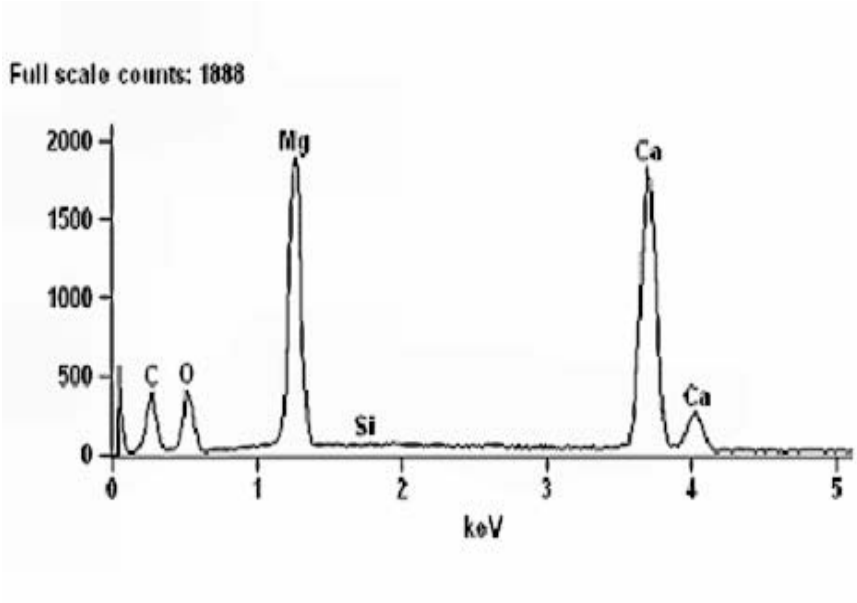

Figure 3.12: EDS spectrum of dolomite at position 3.

Shrinking unreacted Core Model (SCM)

There are three resistances to reaction for the gas-solid reaction between CO_2 and calcined dolomite:

i) External mass transfer

ii) Intra-particle diffusion

iii) Chemical reaction

The three resistances occur in series and the algebraic combination of them is simply handled by the classic Ohm's law treatment of resistances in series, eliminating intermediate concentration terms, and yielding a relationship for the rate of reaction with the driving force expressed in terms of bulk concentration. Each case where one of the three resistances is dominant is considered separately.

Assumptions for derivation

i) It is assumed that CaO and inert material (mainly MgO) are uniformly distributed in the dolomite pellet. Carbonation of MgO is thermodynamically unfavorable at temperatures above 500°C at ambient pressure, and is therefore considered inert. However, it still makes up a great part of total volume of the particle, and the derivation is for the particle of dolomite.

ii) Single spherical particle.

iii) Constant particle size.

A detailed derivation, based on the original shrinking core model from Levenspiel [73], is provided in Appendix A.1 and only the final rate expression is presented in Eq.(3.4):

$$\frac{dX}{dt} = \frac{\frac{3}{R_p} \cdot (1-X)^{2/3} \cdot \frac{b}{\rho_B \cdot R \cdot T} \cdot (P_{Ag} - P_{Ae})}{\frac{1}{k} + \frac{R_p \cdot [(1-X)^{1/3} - (1-X)^{2/3}]}{D_e} + \frac{(1-X)^{2/3}}{k_g}} \tag{3.4}$$

A first order reaction constant, k, is assumed in the derivation of Eq.(3.4), making elimination of interfacial pressures possible, arriving at a linear dependency of CO_2 partial pressure. However, Kyaw et al. [72] have found the difference between partial pressure and equilibrium pressure to be nonlinear (Eq.(3.3)). It was therefore decided to modify the rate equation by including a nonlinear partial pressure difference, n. Note that n accounts for the nonlinear partial pressure difference between CO_2 in the bulk phase and the equilibrium pressure, and should not be considered as a reaction order. The final rate equation can then be written as:

$$\frac{dX}{dt} = \frac{\frac{3}{R_p} \cdot (1-X)^{2/3} \cdot \frac{b}{\rho_{CaO} \cdot R \cdot T} \cdot (P_{CO_2} - P_{CO_2,e})^n}{\frac{1}{k} + \frac{R_p \cdot [(1-X)^{1/3} - (1-X)^{2/3}]}{D_e} + \frac{(1-X)^{2/3}}{k_g}} \tag{3.5}$$

where R_p is the particle radius (m), b is the stoichiometric coefficient ($\frac{\text{mole CaO}}{\text{mole CO}_2}$) equal to unity, ρ_{CaO} is the molar density of CaO in dolomite ($\frac{\text{mole CaO}}{\text{m}^3 \text{ dolomite}}$), P_{CO_2} and $P_{CO_2,e}$ are the partial pressures (Pa) in the bulk phase and at equilibrium respectively, n is nonlinearity factor, k is the reaction rate constant ($\frac{m}{s}$), D_e is the effective diffusivity ($\frac{m^2}{s}$), k_g is the external mass transfer coefficient ($\frac{m}{s}$) and X is conversion.

The reaction rate constant, k, is expressed as:

$$k = k_0 \cdot exp(\frac{E_a}{R \cdot T}) \tag{3.6}$$

where k_0 is a Arrhenius pre-exponential constant ($\frac{m}{s}$) and E_a is the activation energy ($\frac{\text{kJ}}{\text{mole}}$). By inspection of the form of Eq.(3.4), regardless of the mathematics, one can see it contains a driving force in the numerator represented by the difference between partial pressure of CO_2 and its equilibrium pressure at the reaction temperature. The denominator contains the three resistances to the reaction in series, and the relative importance of these individual resistances varies as conversion progresses.

A major problem with the shrinking unreacted core model is to obtain the value of the effective diffusivity, D_e. Zevenhoven et al. [74] modeled the particle conversion of limestone and dolomite sulfidation, using a variable effective diffusivity. Because of the build-up of a solid product layer as the reaction proceeds, intra-particle transport of CO_2 is strongly affected by the progress of conversion. Their effective diffusivity takes into account two mechanisms:

i) Diffusion in the pores of the particle (gas phase diffusion and Knudsen diffusion)

ii) Diffusion through a solid product layer

These two mechanisms occur in series, and CO_2 has to diffuse through the pores in the particle and in addition diffuse through the product layer before it can react with the solid reactant. It is shown that the effective diffusivity can be expressed as:

$$D_e = D_e(X) = D_{eff,0} \cdot \frac{(1 + A \cdot X)}{(1 + B \cdot X)} \tag{3.7}$$

$$A = \frac{1-\epsilon_0}{\epsilon_0}, \qquad D_{eff,0} = D_{pore} = \frac{\epsilon_0}{\tau} \cdot D_{mol+Kn} \quad \text{and} \qquad B = \frac{A \cdot D_{pore}}{D_{pl}}$$

where ϵ_0 is the initial particle porosity, τ is the tortuosity factor, D_{mol+Kn} is the combined molecular and Knudsen diffusivity in the gaseous phase inside the porous solid and D_{pl} is the product layer diffusivity. The effective diffusivity, D_e, is constant only when the product layer diffusivity, D_{pl}, becomes of the same order of magnitude as the pore diffusivity. More details on the diffusivity calculations are found in Appendix A.2.

3.3.2 Experimental approach

Studies of carbonation reaction rates are usually done by thermo gravimetric analysis. A small amount of sample is placed in a sample pan in an oven, and the sample pan is connected to a microbalance. The weight change is recorded continuously during the carbonation, and conversion-versus-time plots are then obtained. Typically, reaction constants at various temperatures are then plotted versus reciprocal temperature, and the activation energy can the be found. However, there are two major disadvantages with this kind of experimental set-up:

i) Assuming constant temperature. A small sample amount is used to assure that the temperature variation within the sample is minimized. However, the carbonation reaction is a very exothermic reaction and heat is produced during the reaction, even for a small amount of sample, and temperature variation during the course of reaction should therefore be taken into account. The design of a conventional TG apparatus makes temperature measurements in the sample very difficult, and it is common to make the assumption of constant temperature.

ii) Flow pattern. Most of the reactant gas by-passes the sample pan, and each pellet in the sample is not in direct contact with the bulk of the flowing gas. This may cause situations where external mass transport is the rate limiting step.

The assumption of constant temperature in the sample of a converional TG reactor was checked by inserting a thermocouple into the sample during carbonation. Weight change could not be registered as this thermocouple interferred with the microbalance. A sample of 200 mg calcined dolomite was put in the sample pan, and exposed to nitrogen to obtain a temperature baseline before changing to 100% CO_2 and recording the temperature change in the sample, as shown in Figure 3.13. A maximum temperature rise of $\sim$60°C was observed during the course of carbonation. The temperature drops as the exothermic reaction ceases upon complete carbonation. It is evident that assuming isothermal conditions is a poor assumption. One might accept gradients when investigating the reversible carbonation reaction in multi-cycle tests, but when evaluating the kinetics, temperature control is much more critical. Therefore, efforts have been made to overcome the above mentioned weaknesses of conventional TGA.

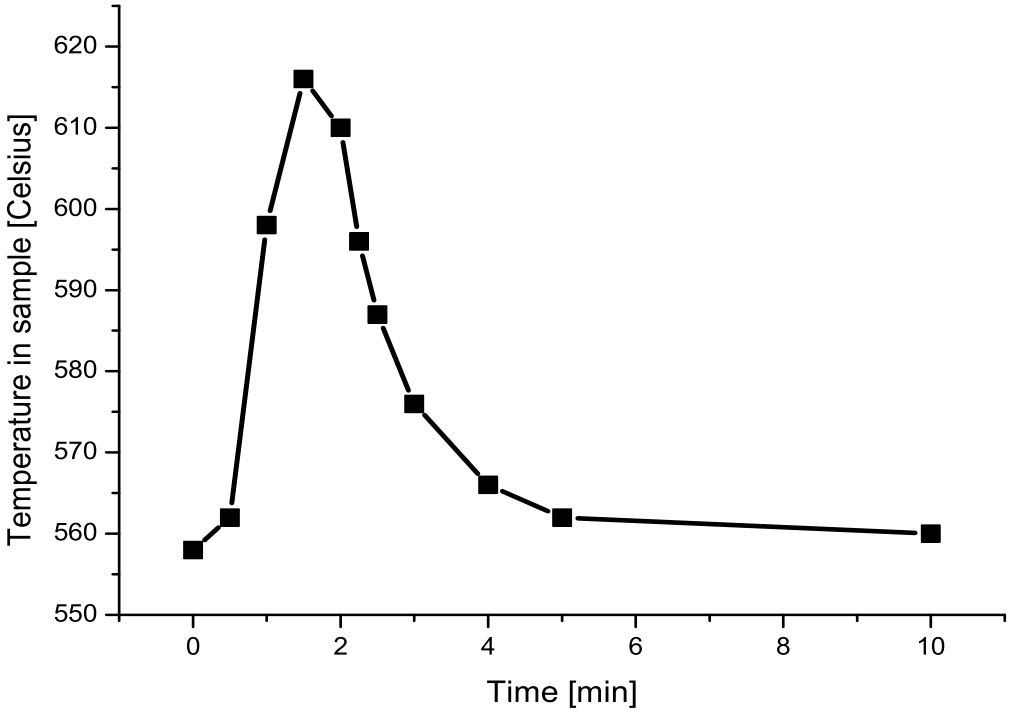

Figure 3.13: Temperature profile of Arctic dolomite during carbonation in conventional TGA (200 mg sample was exposed to 100% CO_2 at 550°C).

Experimental set-up and conditions

Instead of trying to eliminate the temperature gradients, an approach where both temperature and weight change could be recorded simultaneously during the course of reaction, was chosen. A novel thermo gravimetric reactor was used for this study, and schematic drawings of the experimental set-up and the reactor are shown in Figure 3.14 and Figure 3.15, respectively. The reactor was connected to a balance that recorded weight change (like the sample pan of a conventional TG reactor) and placed in an oven. The gas is pre-heated in the double-walled reactor before it flows upwards through a sinter, on which the sample is placed. A thermocouple (K-type) was placed in the sample, and the temperature was registered continuously together with weight change during the carbonation of calcined dolomite.

A series of five runs were performed with Arctic dolomite as sorbent. The experi-

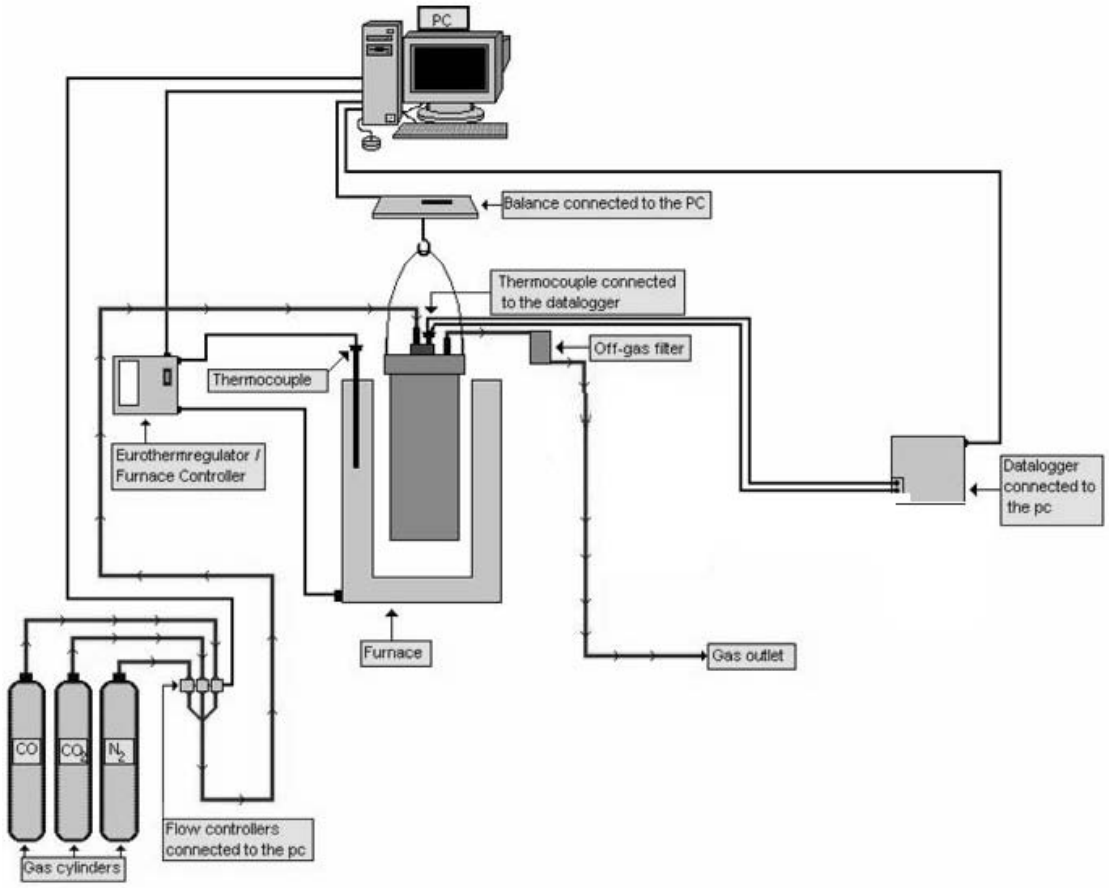

Figure 3.14: Experimental TGA set-up used for the study of carbonation kinetics.

mental conditions are listed in Table 3.6. A total flow rate of 2 NL/min was used. The amount of dolomite used in each experiment was approximately 10 grams, with particle diameters in the range of 200-300 μm. The flow rate corresponds to a superficial velocity of 0.042 m/s at 550°C (reactor cross-sectional area of 24 cm^2). The minimum fluidization velocity at the same temperature with an average particle size of 250 μm is calculated to be 0.017 m/s for fully calcined dolomite, and 0.024 m/s for the half calcined dolomite, based on calculations from the Ergun software (Ergun 6.0, Divergent S.A). Hence, the gas velocities used were always above the minimum fluidization velocity, utilizing the advantageous temperature uniformity caused by mixing. The effect of fluidization on the scale was checked with inert particles to make sure that the weight increase registered during carbonation was entirely caused by CO_2-uptake.

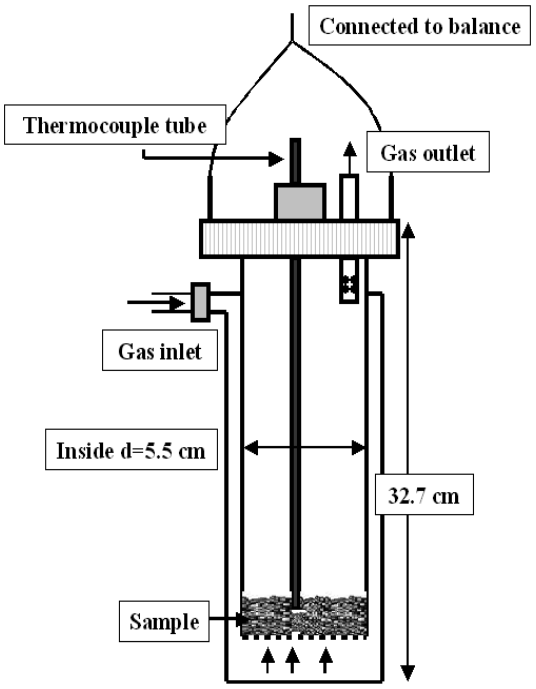

Figure 3.15: Reactor used for studying carbonation kinetics.

Table 3.6: Experimental operating conditions for reaction rate investigation

Sample ID	**Initial sample temperature** [a][°C]	**CO_2 partial pressure [atm]**
Kin-Dolo1[b]	550	1
Kin-Dolo2	550	0.8
Kin-Dolo3	550	0.5
Kin-Dolo4	730	1
Kin-Dolo5	650	1

[a] Sample temperature at t=0 in argon, before switching to the carbonation atmosphere

[b] Particle diameter in the range of 150-200 μm

3.3.3 Kinetic analysis and discussion

A typical experimental response curve, where both conversion and sample temperature are plotted against time, is shown in Figure 3.16. The sampling rate was set to 1 second. However, some sample points are left out in this figure for better visual illustration while raw data for all runs are presented in Appendix B.1.

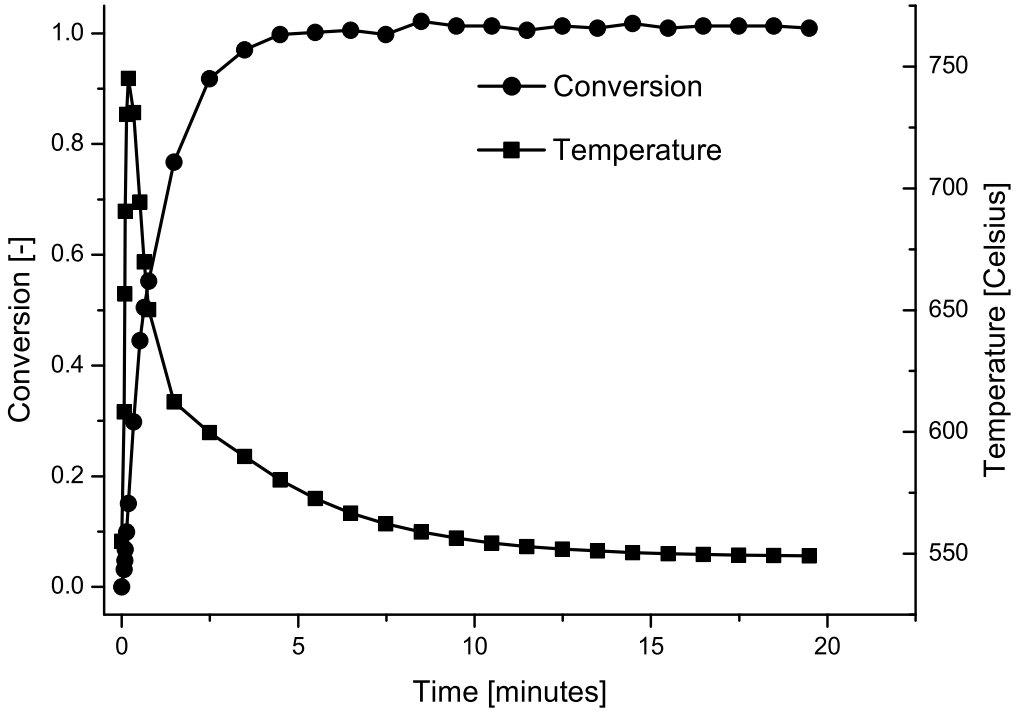

Figure 3.16: Temperature and conversion of the sorbent as a function of time for sample Kin-Dolo1 (100% CO_2 at 550°C).

Figure 3.16 shows a remarkable temperature rise in the sample as CO_2 is introduced at a initial temperature of 550°C, caused by the heat released from the exothermic carbonation reaction. In this non-isothermal approach, kinetic parameters can be obtained by fitting conversion as function of time with multiple experimental temperatures as input. Temperature uniformity within the sample is assumed.

Model equations

The rate expression Eq.(3.5) has the unit of s^{-1}. A more useful expression is obtained by multiplying by the molar density

$$R_{dolo}(X) = \frac{dX}{dt} \cdot \rho_{CaO} = \frac{\frac{3}{R_p} \cdot (1-X)^{2/3} \cdot \frac{b}{R \cdot T} \cdot (P_{CO_2} - P_{CO_2,e})^n}{\frac{1}{k} + \frac{R_p \cdot [(1-X)^{1/3} - (1-X)^{2/3}]}{D_e} + \frac{(1-X)^{2/3}}{k_g}} \tag{3.8}$$

where $R_{dolo}(X)$ has the unit of $\frac{\text{mol CaO}}{\text{m}^3 \text{ dolomite} \cdot s}$. The bed of solids in the reactor (Figure 3.15) is modeled as a batch process

$$\frac{1}{V_{dolomite}} \cdot \frac{dn_{CaO}}{dt} = -R_{dolo}(X) \tag{3.9}$$

Expressed as conversion, using the relationship $n_{CaO} = n_{CaO,0} \cdot (1 - X)$

$$\frac{dX}{dt} = R_{dolo}(X) \cdot \frac{V_{dolomite}}{n_{CaO,0}} \tag{3.10}$$

where $n_{CaO,0}$ is the initial molar amount of CaO. The volume of solids in the reactor, $V_{dolomite}$, is calculated from $V_{dolomite} = V_{bed} \cdot (1 - \epsilon)$, where ϵ is the bed voidage. The rate of carbonation is dependent on the partial pressure of carbon dioxide, and a mole balance for the consumption of CO_2 must also be included:

$$\frac{dn_{CO_2}}{dt} = n_{CO_2,feed} - n_{CO_2} - R_{dolo}(X) \cdot V_{dolomite} \tag{3.11}$$

Numerical procedure

Parameters to be estimated by fitting:

i) Arrhenius pre-exponential constant, k_0 [m/s]

ii) Activation energy, E_a [kJ/mole]

iii) Product layer diffusion constant, D_{pl} [m^2/s]

iv) Nonlinearity factor , n [-]

The conversion dependent effective diffusion constant, D_e, accounts for all diffusion effects inside the solid particle. Product layer diffusivity, D_{pl}, was chosen as fitting

parameter, while pore diffusion was calculated using correlations listed in Appendix A.2.

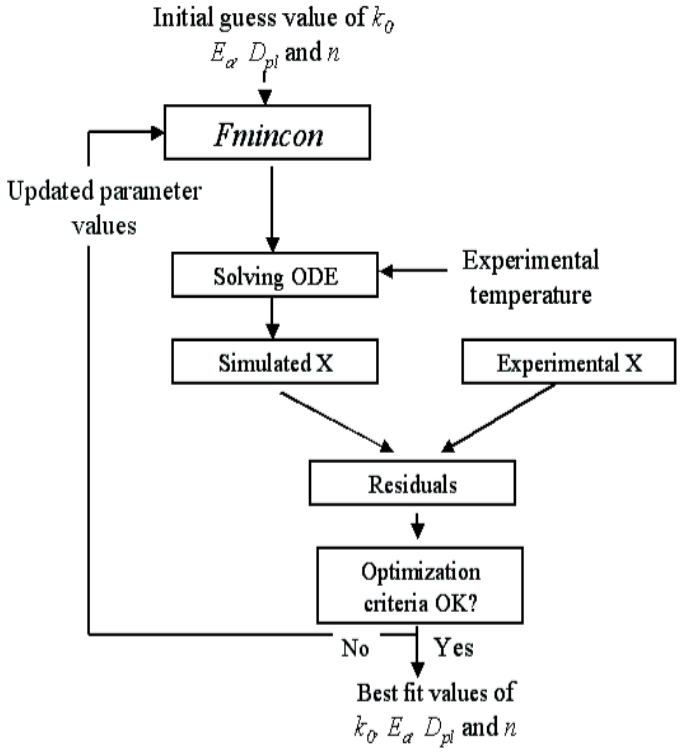

Figure 3.17: Numerical procedure for fitting kinetic parameters to experimental data.

A in-built optimization function in MATLAB (MATLAB 6.5, The MathWorks, Inc.), *fmincon*, was used for determining the best-fit parameters. The model equations, Eqs.(3.10-3.11), are described by ordinary differential equations (ODE) that can be solved numerically by using ODE solvers in MATLAB (e.g. ode45). However, using experimental temperatures as input required a constant time-step solution method, therefore a simple Euler approximation was used for solving the ODEs. Arbitrary initial values of the fitting parameters are used as input for solving the rate equation, and the simulated time-versus-conversion data are evaluated and compared with experimental data. Figure 3.17 shows the iterative procedure for obtaining the best-fit parameters. More details regarding the solving procedure, including MATLAB-scripts, are found in Appendix B.2. The optimization procedure, *fmincon*, is based on minimization of a user-defined function, and the sum of squared residuals was chosen for minimization:

$$F_{min} = \sum_{k=1}^{m} \sum_{t=0}^{n} (X_{k,t,predicted} - X_{k,t,experimental})^2 \tag{3.12}$$

where F_{min} is the sum of residuals from *t=0* up to *t=n* of m data sets. Three data sets (m=3) were used for fitting and obtaining kinetic parameters, while two data sets (Kin-Dolo2 and Kin-Dolo4) were used for prediction purpose. The number of sample points, n, was set to 240, which corresponds to 4 minutes.

Fitting to rate expression

The reaction rate parameters obtained from fitting are presented in Table 3.7. A comparison of the model with experimental data is shown in Figure 3.18.

Table 3.7: Carbonation rate parameters

$\mathbf{k}_0$ $[\frac{m}{s}]$	$\mathbf{E}_a$ $[\frac{kJ}{mole}]$	$\mathbf{D}_{pl}$ $[\frac{m^2}{s}]$	**n** [-]
3.05	32.6	$7.7 \cdot 10^{-9}$	0.66

The activation energy of 32.6 kJ/mole, obtained from the current work, is somewhat lower than the activation energy found by Kyaw et al. [72] of 35 kJ/mole using dolomite as sorbent, but still in good agreement with this previously reported value. The proposed model tries to include both the rapid chemically controlled and the slow diffusion layer controlled regimes using a conversion dependent effective diffusivity. Therefore, the activation energy obtained from fitting should be considered an apparent activation energy rather than intrinsic. Also, the value of the product layer diffusion constant, D_{pl}, is close to the range of previously reported diffusivities from Zevenhoven et al. [74], which report values of $1.5\text{-}3.5 \cdot 10^{-10}$ $\frac{m^2}{s}$ for five different limestones.

In general, the proposed rate expression describes the experimental data reasonably well. The degree of conversion at the initial stage of carbonation is modeled very well for all five sets, but the shift in the rate determining mechanism (from chemical to diffusion controlled) is not well predicted for Kin-Dolo4 by using the conversion dependent effective diffusivity, where only the first ∼30% is predicted satisfactory. Prediction of the other data set left out when obtaining fitting parameters (Kin-Dolo2) is very good up to 50-60%, but is somewhat poorer after that. However, from a practical point of view,

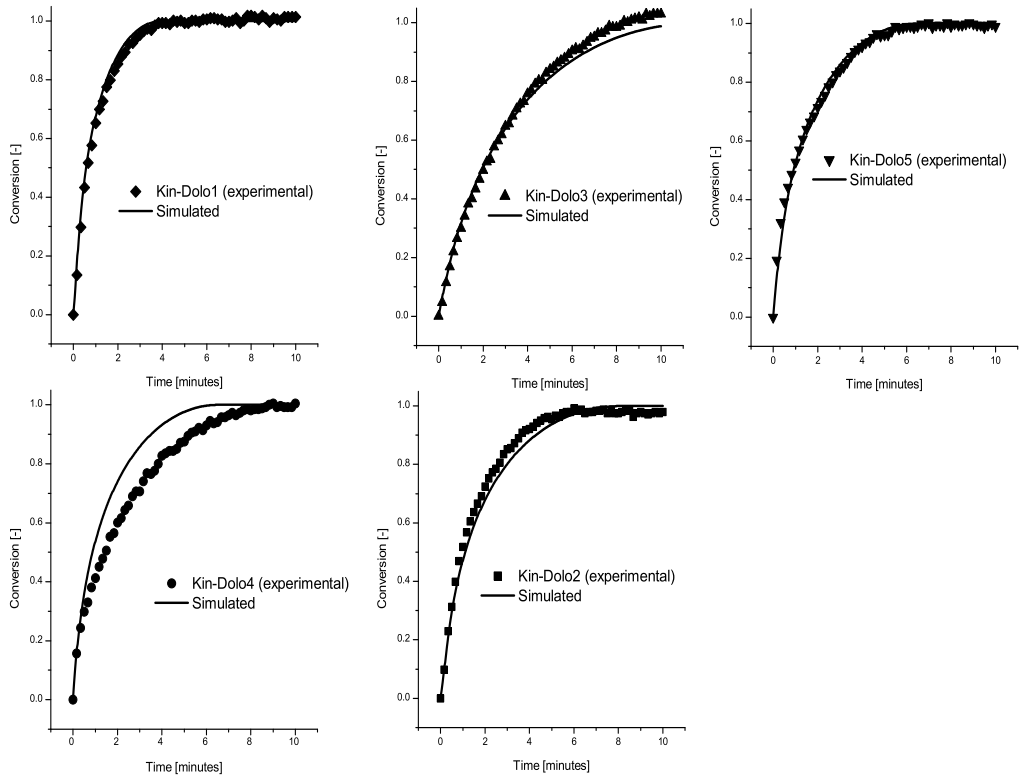

Figure 3.18: Comparison of experimental conversion (points) and model predictions (solid lines) for carbonation of Arctic dolomite.

only the rapid initial stage of carbonation is of interest when capturing CO_2 with CaO in an industrial application. It is therefore believed that the model is well suited for prediction of typical conversion levels expected in a continuous reforming-regeneration system, e.g. circulating fluidized beds.

Another model approach in which the energy balance was included, failed to predict both the conversion and temperature profiles. This was probably due to heat losses, which should be accounted for, but were difficult to quantify. Experiments with lower partial pressures of CO_2 than 0.5 atm could not be conducted due to flow rate restrictions of the mass flow controllers, and the current model is strictly speaking only valid for CO_2 partial pressures down to 0.5. However, it is assumed that the model can be extrapolated to be valid for partial pressures typically present in SE-SMR, making the

rate expression useful for the purpose of process design and modeling.

The non-isothermal approach applied in the current study is based on the elimination of the previously mentioned limitations of conventional TGA. However, the experimental set-up of the novel thermo gravimetric reactor in Figure 3.15 introduces new assumptions when evaluating the kinetics. For example, the temperature measured is assumed to be uniform within the bed of solids, by using gas velocities just above the minimum fluidization velocity of the sample, hence utilizing the excellent heat transfer caused by mixing. However, the formation of gas bubbles should be avoided as this will cause significant by-passing of gas. Therefore, a very shallow bed of solids has to be used, which again makes temperature measurements more difficult. Ideally, several thermocouples should bed inserted in the bed, to see if radial temperature variations are present. Anyway, it evident that the assumption of constant temperature during carbonation is poor, and the non-isothermal approach used here is believed to represent an improved methodology for studying the kinetics of gas-solid reactions.

3.4 Novel sorbents

There are a number of criteria that needs to be fulfilled for synthetic sorbents to be able to compete with natural sorbents. Two synthetic sorbents, Li_2ZrO_3 and Na_2ZrO_3, were prepared and tested by TGA with respect to reaction rates and multi-cycle behaviour and compared to the performance of Arctic dolomite.

3.4.1 Synthesis

A low-temperature liquid phase co-precipitation method, as described and patented by Yi and Eriksen [45, 75], was used for the synthesis of Li_2ZrO_3 and Na_2ZrO_3.

Lithium nitrate ($LiNO_3 \cdot xH_2O$, ca 78% $LiNO_3$, Merck) and zirconium oxynitrate hydrate ($ZrO(NO_3)_2 \cdot 2H_2O$, Merck) were used as precursors. Sufficient starting materials, to produce a Li/Zr molar ratio of 2, were dissolved in distilled water in separate beakers. The solutions were mixed and aged overnight at room temperature accompanied by stirring with a magnetic bar. The mixed oxide was precipitated by dropwise addition of aqueous ammonia (NH_3, 25%, Merck), followed by filtering, drying and calcination. The same procedure was used for the synthesis of Na_2ZrO_3, with sodium nitrate ($NaNO_3$, Aldrich) and zirconium oxynitrate hydrate ($ZrO(NO_3)_2 \cdot 2H_2O$, Merck) as precursors.

3.4.2 Results and discussion

The prepared samples were put in the TGA and exposed to a simulated reforming atmosphere of 10% CO_2, 30% steam and balanced with nitrogen at a temperature of 550°C. The CO_2 uptake curves for the first 20 minutes are shown in Figure 3.19.

Na_2ZrO_3 has a superior reaction rate compared to the other two samples, with an uptake of 0.17 g CO_2/g sorbent after 15 minutes, corresponding to ∼70% conversion, based on its theoretical stoichiometric capacity of 0.24 g CO_2/g sorbent (listed in Table 2.1). The dolomite has a somewhat slower reaction rate, and will require about 70 minutes to come to full conversion. The reaction rate of Li_2ZrO_3 is found to be rather poor in the diluted CO_2 atmosphere used, most likely restricting its potential as a sorbent for the SE-SMR process. The very rapid reaction rate of Na_2ZrO_3 is in accordance with the findings of L*ó*pez-Ortiz et al. [46], who rated the reaction rates, from higher to lower, in pure CO_2 atmosphere at 600°C: $Na_2ZrO_3 > Li_4SiO_4 > Li_2ZrO_3$.

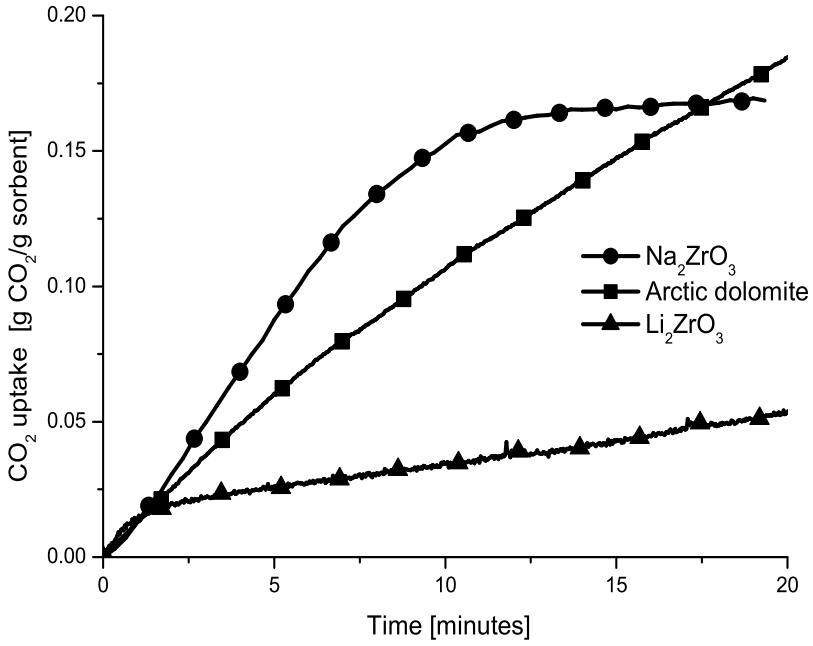

Figure 3.19: Rate of CO_2 removal (T=550°C, P_{CO_2}=0.1 atm, P_{H_2O}=0.3 atm and P_{N_2}=0.6 atm).

Ochoa-Fernández et al. [56] report the slow sorption kinetics of Li_2ZrO_3 at low partial carbon dioxide pressures to be caused by a second order concentration dependency.

Multi-cycle TGA tests of the synthetic sorbents were performed, and the experimental conditions are listed in Table 3.8. Figure 3.20 shows how Li_2ZrO_3 maintains its capacity, after ∼40 cycles, at a constant value of approximately 0.22 g CO_2/g Li_2ZrO_3, which corresponds to 80% of the theoretical sorption capacity for this sorbent. The carbonation time of 20 minutes was set too low for full conversion to be reached in each cycle, confirming the rather slow kinetics of carbonation for this sorbent. Moreover, the theoretical sorption capacity is based on pure compound to be produced from the synthesis, which is unlikely from the co-precipitation method used. Figure 3.21 shows that Na_2ZrO_3 is able to maintain its sorption capacity in the same manner as the Li_2ZrO_3, with a CO_2-uptake of ∼18 g CO_2/g Na_2ZrO_3.

From the above findings it is evident that Na_2ZrO_3 is a very promising sorbent, with both very fast carbonation kinetics and stable multi-cycle capacity. Nitrogen was used

Table 3.8: Multi-cycle conditions for the synthetic sorbents

		Carbonation			Calcination			
Sample	**D_p**	**Temp.**	**Atm.**	**Time**	**Temp.**	**Atm.**	**Time**	**Total Duration**
Li_2ZrO_3	100-200μm	550°C	75%CO_2 25% H_2O	20 min.	700°C	50% N_2 50% H_2O	20 min.	$\sim$ 60 h
Na_2ZrO_3	100-200μm	600°C	75%CO_2 25% H_2O	20 min.	850°C	100% N_2	40 min.	$\sim$ 80 h

as calcination atmosphere in the multi-cycle test, and regeneration was performed at 850°C, where complete regeneration was achieved within 40 minutes.

From a practical point of view, nitrogen is unlikely to be used for calcination, and regeneration in other atmospheres was tested. The sodium zirconate was successfully regenerated when 50% steam was added to the calcination atmosphere, as illustrated in Figure 3.22. The nitrogen was then replaced by carbon dioxide in the subsequent cycle, without any CO_2 being released at regeneration temperature of 850°C. Moreover, increasing the temperature to 950°C did not enhance the decomposition of the carbonate, indicating that the presence of CO_2, even at very high temperatures, inhibit the calcination reaction. The effect of lowering the carbon dioxide partial pressure was further investigated, and the results are shown in Figure 3.23. It was not possible to calcine Na_2CO_3 in the presence of 10% CO_2 at 850°C, while complete regeneration was achieved for 4% CO_2 at the same temperature within 40 minutes. Moreover, regeneration in a steam/nitrogen mixture is faster than when CO_2 is present. This means that very low partial pressures of CO_2 is required in the calciner to be able to regenerate the sorbent. Fluidized beds have substantial backmixing of gas and a certain partial pressure of carbon dioxide, dependent on fluidization velocity, will be present in the vessel during calcination. Given the adverse effect of CO_2 on regeneration rate, this is likely to restrict the use of the sorbent for the SE-SMR process. However, more detailed studies are required for understanding the reaction mechanisms of Na_2ZrO_3. Addition of promotors to enhance the rate of reversibility, as proposed by L*ó*pez-Ortiz et al. [46], could be investigated.

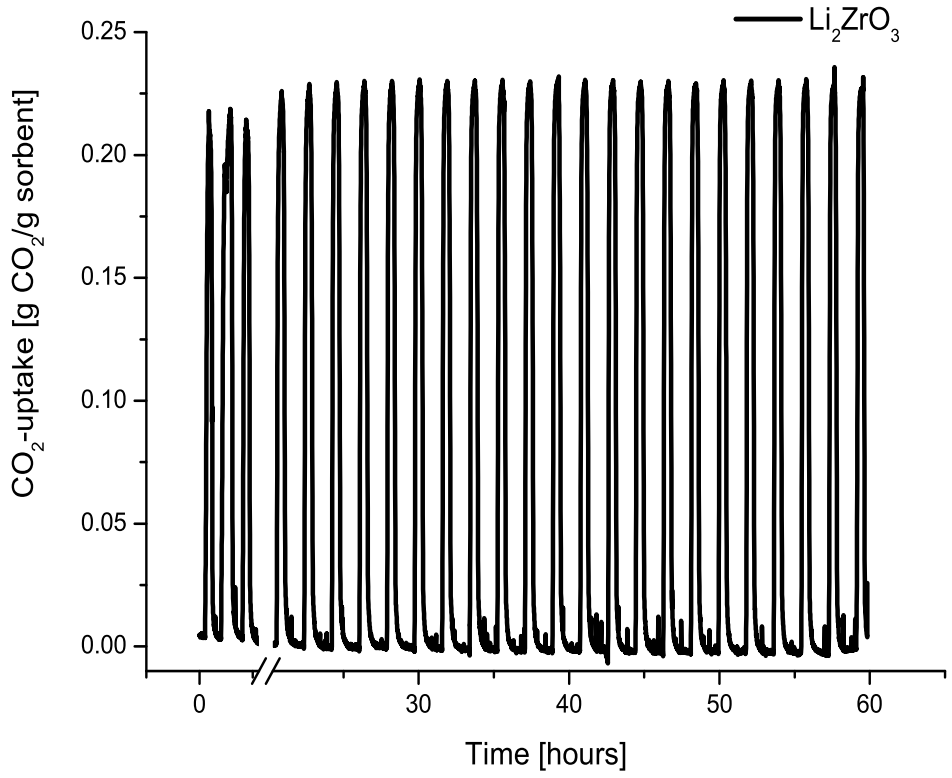

Figure 3.20: Multi-cycle conversion of Li_2ZrO_3 (Carbonation: T=550°C, P_{CO_2}=0.75 atm and P_{H_2O}=0.25 atm; Calcination: T=700°C, P_{N_2}=0.5 atm and P_{H_2O}=0.5 atm).

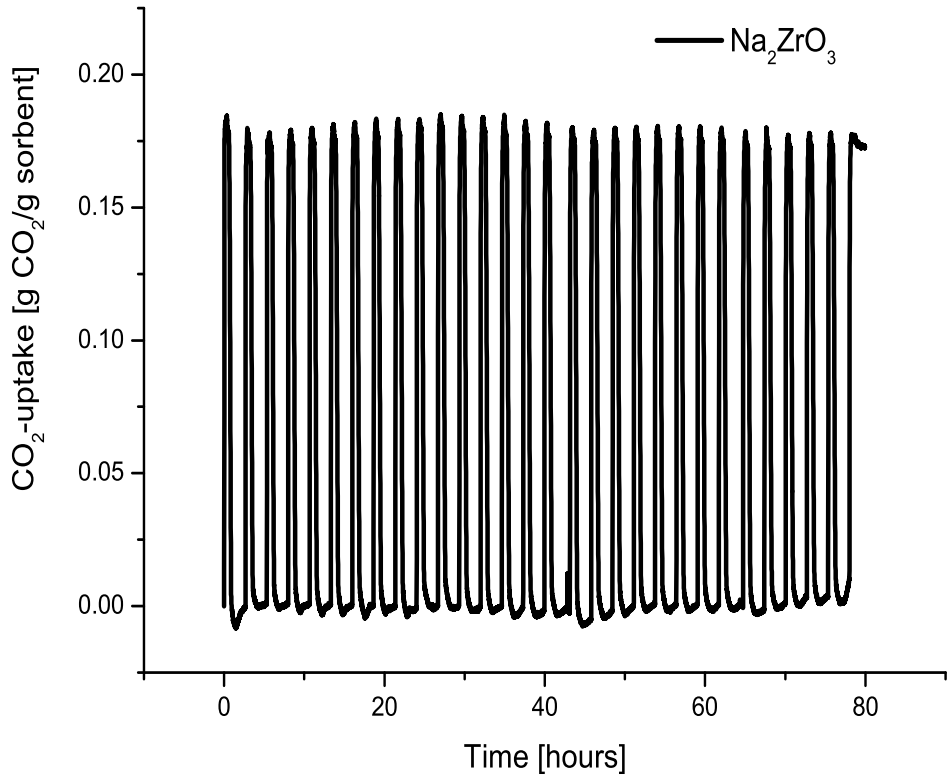

Figure 3.21: Multi-cycle conversion of Na_2ZrO_3 (Carbonation: T=600°C, P_{CO_2}=0.75 atm and P_{H_2O}=0.25 atm; Calcination: T=850°C, P_{N_2}=1 atm).

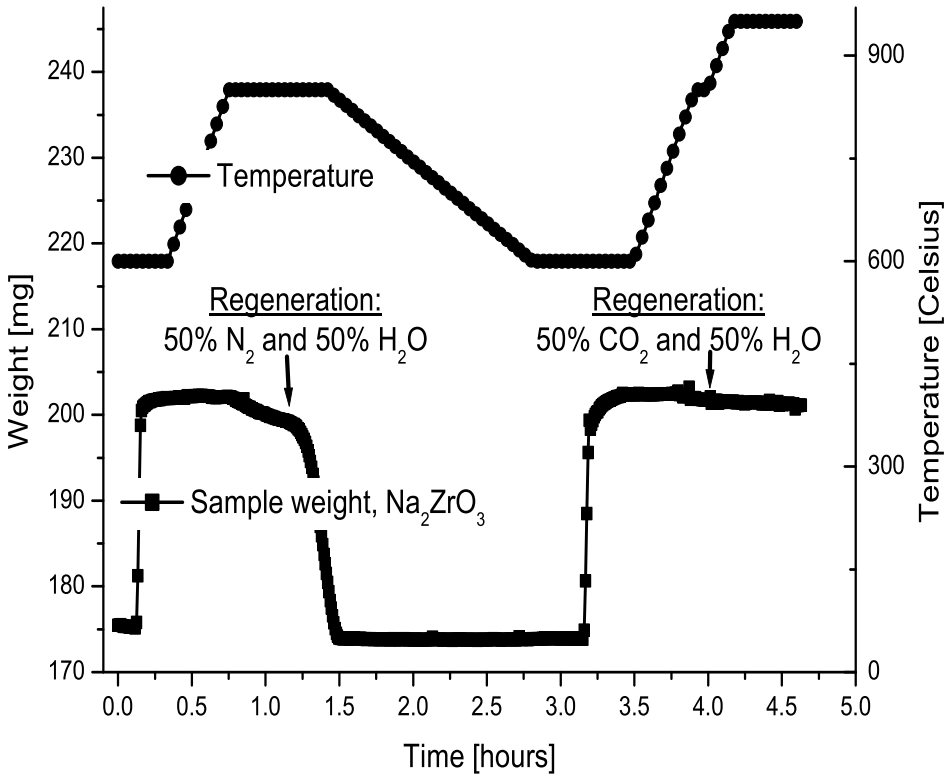

Figure 3.22: Regeneration of Na_2ZrO_3 with and without the presence of carbon dioxide in the regeneration atmosphere.

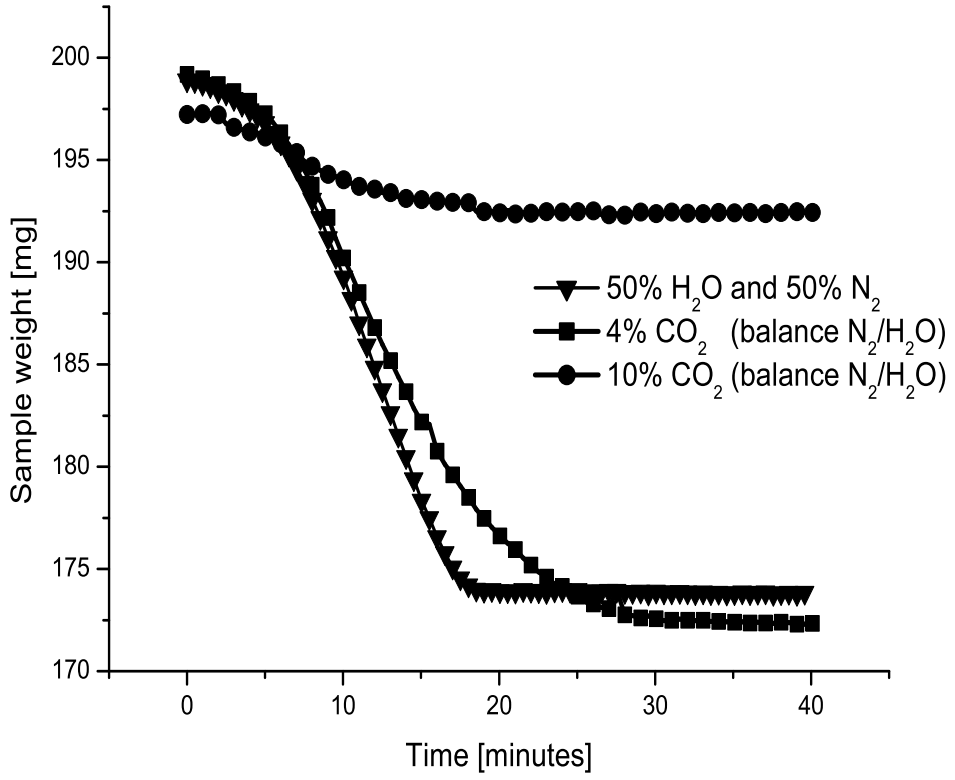

Figure 3.23: Regeneration of Na_2ZrO_3 at 850°C without the presence of CO_2 (−▼−), 4% CO_2 (−■−) and 10% CO_2 (− • −) in the regeneration atmosphere.

Summarizing, synthetic Na_2ZrO_3 and Li_2ZrO_3 for high-temperature CO_2 capture were produced from a simple low-temperature liquid phase co-precipitation method, with Na_2ZrO_3 showing the highest carbonation rate in addition to good multi-cycle stability. However, regeneration could not easily be done in the presence of >10% CO_2 at 850°C. Moreover, a regeneration temperature of 950°C was not sufficient to decompose the sodium carbonate in 50% CO_2. The lithium zirconate was found to be regenerable in the presence of carbon dioxide and very stable during multi-cycling, but the rate of reaction in a diluted CO_2 atmosphere was very slow. Mechanical tests of attrition resistance or crushing strength were not performed, but the produced powders were seemingly rather fragile based on visual observations and sieving of the samples. Additional coating with a porous "shell" around the CO_2-acceptor, e.g. Al_2O_3, is likely to be required in order to avoid excessive loss of fines upon fluidization of these fragile synthetic sorbents.

Chapter 4

Bubbling fluidized bed reformer

Continuous reforming with CO_2 removal requires either that there be parallel reactors operated alternatively and out of phase in reforming and sorbent regeneration modes, or that sorbent be continuously transferred between the reformer/carbonator and regenerator/calciner. Fluidized bed reactors allow transfer of solids between reactors and are commonly used in processes where catalysts must be continuously regenerated. Coupling of two bubbling beds will have the advantage of low rates of attrition due to low gas and particle velocities, and the relatively slow carbonation reaction rate will be facilitated in this flow regime. In this chapter, a bubbling fluidized bed is used for sequential sorption-enhanced steam methane reforming and regeneration of sorbent. Due to the lack of experimental data in the open literature on the performance of the overall process in such reactor configuration, special attention is given to the multi-cycle performance of both the sorbent and the catalyst. The rate of the combined reactions is also evaluated using different superficial gas velocities within the bubbling regime.

4.1 Experimental

4.1.1 Reformer unit

A schematic of the reactor is shown in Figure 4.1. This reactor was used previously [76] in studies of fluidized bed roasting of zinc concentrates, and was modified for the purpose of SE-SMR. Among the most significant modifications were including a water feed line and a sampling line for outlet gas analysis.

The major components of the reactor consist of a pre-heater, a 0.66 m high and

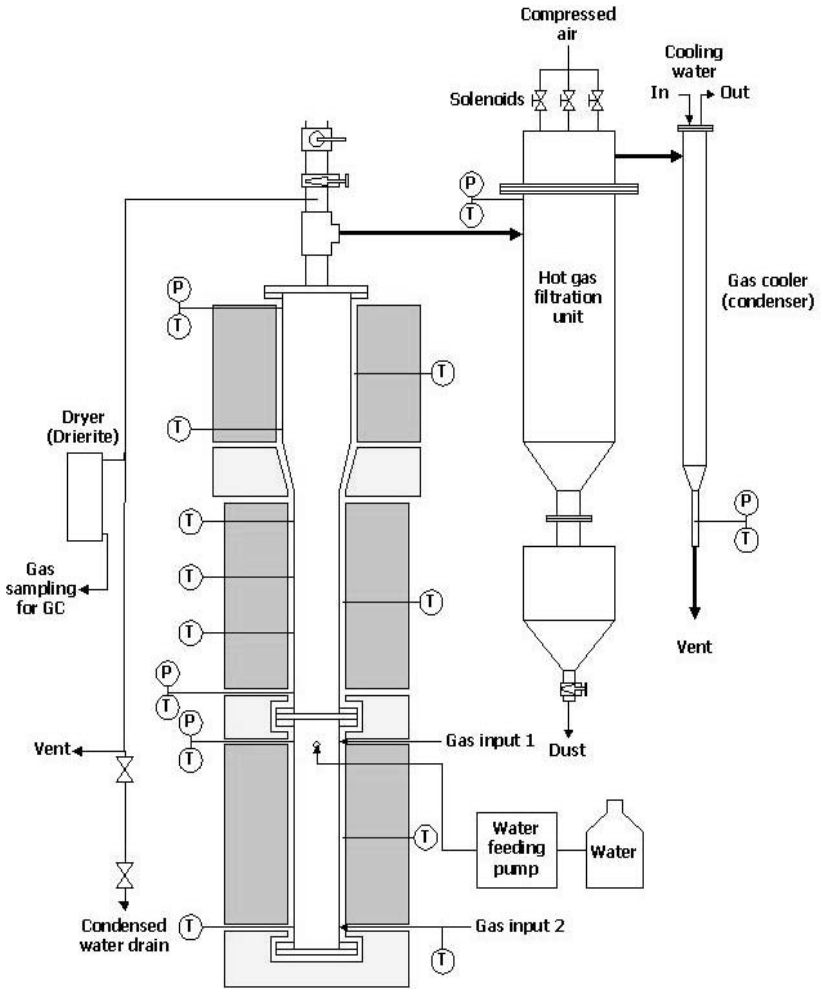

Figure 4.1: Schematic of reformer unit.

0.1 m ID stainless steel fluidized bed reactor with freeboard, a filtration unit and a gas cooler unit. Methane was fed to the upper part of the pre-heater where it was mixed with steam. A removable stainless steel gas distributor plate, with 34 drilled 1.2 mm holes on a hexagonal grid, was placed between the pre-heater and the reactor. The pre-heated reactant gas passes through a mixture of commercial Ni-based steam-reforming catalyst (Haldor Topsoe A/S, R-67R-7H) and calcined dolomite (Franzefoss A/S, Arctic Dolomite). Dolomite was used in preference to limestone because of initial tests indicating better ability to sustain performance in cyclical operation. Three different zones of the reactor were heated by electrical furnaces, which could be controlled individually. Temperatures and pressure drops were recorded by a data acquisition system. Teflon

bags were used for gas sampling from a sampling line at the outlet of the freeboard zone. The sampling line was placed before the filtration unit to eliminate additional carbonation reactions occuring on the filters. The gas composition of the samples was determined using a gas chromatograph (Shimadzu GC-8A, TCD detector).

4.1.2 Sample preparation

The composition of the dolomite is provided in Table 3.1. This dolomite was chosen because it did not contain sulphur, which is poisonous to the reforming catalyst. Prior to the experiments, dolomite and catalyst were sieved to ensure particle sizes between 125-300 μm and 150-250 μm, respectively. The dolomite had to be first calcined to obtain the desired oxide form. This was accomplished at 850°C in N_2 without the catalyst present. A portable gas analyzer (Horiba PG-250) was used to determine complete calcination, corresponding to the disappearance of CO_2 in the product gas. The reactor was then cooled, and part of the calcined dolomite removed and stored in a dessicator for later use, while the rest was mixed with catalyst and re-injected into the reactor.

Table 4.1: BFBR experimental conditions

Parameters	**Values**
Total mass of particles in bed (kg)	3.1
Catalyst-to-calcined dolomite mass ratio (-)	2.5
Static bed height (m)	0.3
Bulk density of mixture (kg/m^3)	1300
Catalyst particle size range (μm)	150-250
Dolomite particle size range (μm)	125-300
Reforming temperature (°C)	600
Superficial velocity (m/s)[a]	0.032[b], 0.064, 0.096
Steam-to-carbon molar feed ratio	3
Calcination temperature (°C)	850
Calcination atmosphere	N_2

[a] Corresponding to flow rates of 5, 10 and 15 NL/min
[b] Gas velocity for multi-cycle test

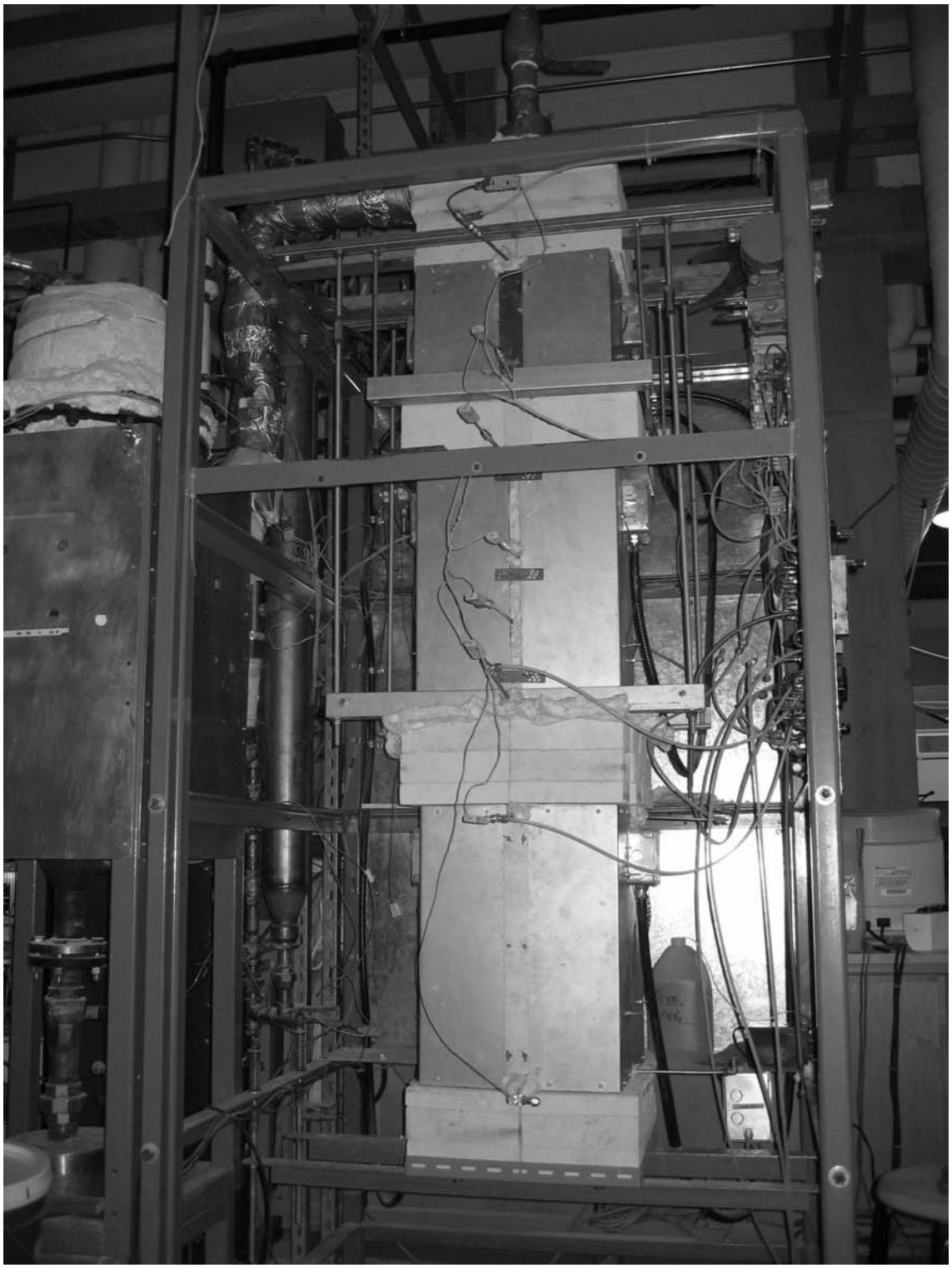

Figure 4.2: Picture of fluidized bed reactor used for studying SE-SMR.

4.1.3 Experimental procedure

The reactor had no feeding lines for solids, and was therefore operated batchwise, with periodic calcination at higher temperatures to regenerate the dolomite. The experimental investigation can be divided into two parts: multi-cycle tests and tests where the superficial gas velocity was varied. Fresh dolomite and catalyst were used for the investigation of the effect of gas velocity in order to make the results for different gas velocities comparable.

The total initial bed mass was 3.1 kg for all runs, with a catalyst-to-calcined dolomite mass ratio of 2.5. During the calcination stages of the multi-cycle tests, pure N_2 was fed to the reactor. No effort was made to separate the catalyst from the dolomite between cycles. To ensure that the catalyst was active, reduction of the catalyst was performed in a H_2/N_2 mixture at 650°C for 1-2 hours prior to each reforming period. The reforming reaction was always carried out at 600°C and ambient pressure. The experimental conditions for the BFBR unit are summarized in Table 4.1. A picture of the reactor system is shown in Figure 4.2.

4.2 Results and discussion

4.2.1 Fluidization

Investigation of fluidization properties of both the catalyst and the dolomite was done in a plexiglass reactor prior to the reforming runs, to ensure operation in the bubbling regime with no particle segregation. A transparent reactor with a diameter of ∼0.1 m, equipped with pressure taps for measuring the pressure drop over the bed of solids, was used for experimental determination of the minimum fluidization velocity, U_{mf}.

The gas velocity was increased and the pressure drop over the bed was registered. First the pressure drop increases linearly as the gas velocity is increased, and the bed behaves like a fixed bed. At a certain velocity, a further increase in the velocity will not lead to increased pressure drop, and gas will bubble through the bed. This point is called the minimum fluidization velocity. The experimentally found minimum fluidization velocities of the catalyst and the dolomite are shown in Figure 4.3.

Dolomite has the higher minimum fluidization velocity of the two particles with 0.032 m/s compared to 0.021 m/s for the catalyst at ambient conditions. The average particle sizes are similar with 200 μm and 215 μm for the catalyst and the dolomite

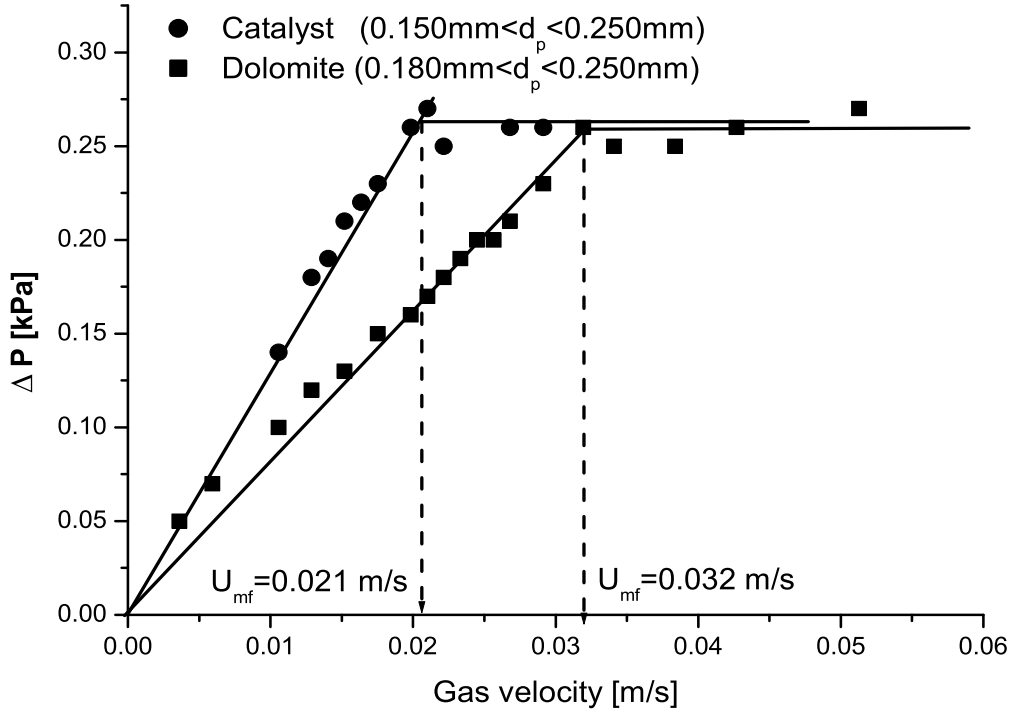

Figure 4.3: Experimental determination of the minimum fluidization velocity of the dolomite and the catalyst (using air at ambient temperature and pressure as fluidizing gas).

respectively, and the difference in minimum fluidization velocity is related to the particle densities, which are listed in Table 4.2. Calcined dolomite will have a lower minimum fluidization velocity than uncalcined dolomite due to lower apparent density caused by initial calcination.

A qualitative investigation of co-fluidization of the dolomite and the catalyst was performed in order to see if segregation would occur. This was easily done due to the fact that the dolomite was a white powder while the catalyst was black, and segregation would visually be observed if present. The catalyst, with an average particle size of 150 μm, was initially added to the bed of calcined dolomite particles of 215 μm, as shown in Figure 4.4. The gas velocity, at ambient conditions, was then increased until bubbling occurred. It was evident that complete mixing of the two particles was achieved, and

Table 4.2: Particle densities

Particle	**Apparent density [kg/m^3]**
Catalyst	2200
Dolomite	2870[a]
Calcined dolomite	1540
Half-calcined dolomite	2220[b]

[a] Data from Franzefoss A/S
[b] Density is calculated from a molar ratio of Ca/Mg=1.1 in Arctic dolomite

no segregation was observed for all gas velocities investigated.

4.2.2 Bubbling bed reformer

Based on the findings from the transparent cold bed reactor, a gas flow rate of 5 Nl/min, corresponding to a superficial gas velocity of 0.032 m/s at 600°C, was chosen as basis. The reaction conditions corresponded to operation in the bubbling bed flow regime. With 0.9 kg calcined dolomite present, the time required for complete carbonation of CaO in dolomite was calculated to be 170 minutes for a superficial gas velocity of 0.032 m/s, based on the assumption that all carbon fed reacted with CaO to yield $CaCO_3$. The total time of operation was 5 hours for each run. A typical response curve is shown in Figure 4.5, with the dry gas composition plotted as a function of time.

The hydrogen concentration is stable at 98-99 volume% on a dry basis for a period of 150-180 min, often referred to as the pre-breakthrough period by previous authors (e.g. Han and Harrison [35]), before there is sudden drop in concentration to ∼72-74%. The opposite trend is observed for the CO_2 concentration, where there is a sudden increase from ∼0.3% to 13-14% after the same interval. CH_4 concentration increases from ∼1.0% to 5-6%, while CO concentration increases from ∼0.4% to 7-8% in the same interval. This characteristic breakthrough occurs when the amount of CO_2 produced by steam reforming exceeds the sorption capacity of the CaO. Figure 4.5 clearly shows the marked enhancement of hydrogen production achieved by in situ capture of CO_2. The shape of the curve is typical for sorption-enhanced steam reforming. Due to the limited number of sample points, the time of the breakthrough cannot be given precisely, but it seems to correspond to a time between 150 and 180 minutes, in good agreement with

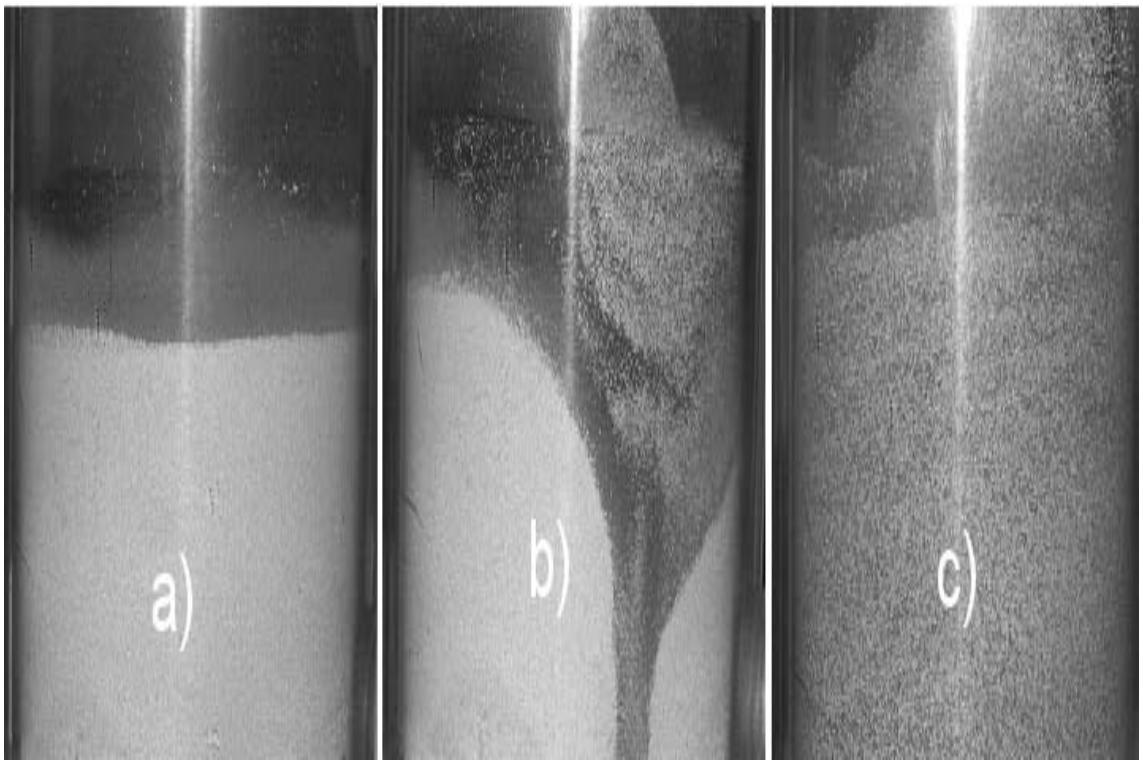

Figure 4.4: Co-fluidization of dolomite (white powder) and catalyst (black powder) at ambient temperature and pressure using air as fluidizing gas; a) Start (no gas flow), b) Bubbling starts, c) Complete mixing.

the calculated time for complete carbonation (assuming 100% calcium utilization) of 170 minutes. After complete carbonation, the hydrogen concentration dropped to a value corresponding to equilibrium of steam methane reforming of ∼73 volume% on a dry basis. At this point, no CaO was left to react with CO_2, so that the reaction enhancement was lost. This period is often referred to as the post-breakthrough period, and re-calcination has to be performed to reactivate the sorbent.

Temperature distribution

Combining the strongly endothermic steam reforming with the exothermic carbonation reaction makes the overall reforming reaction almost thermally neutral. Carbonation of CaO is a reversible reaction, and temperature control is very important to prevent the undesired reverse calcination reaction in the reformer. Temperature uniformity promoted by rapid mixing of the solids makes fluidized beds well suited for processes

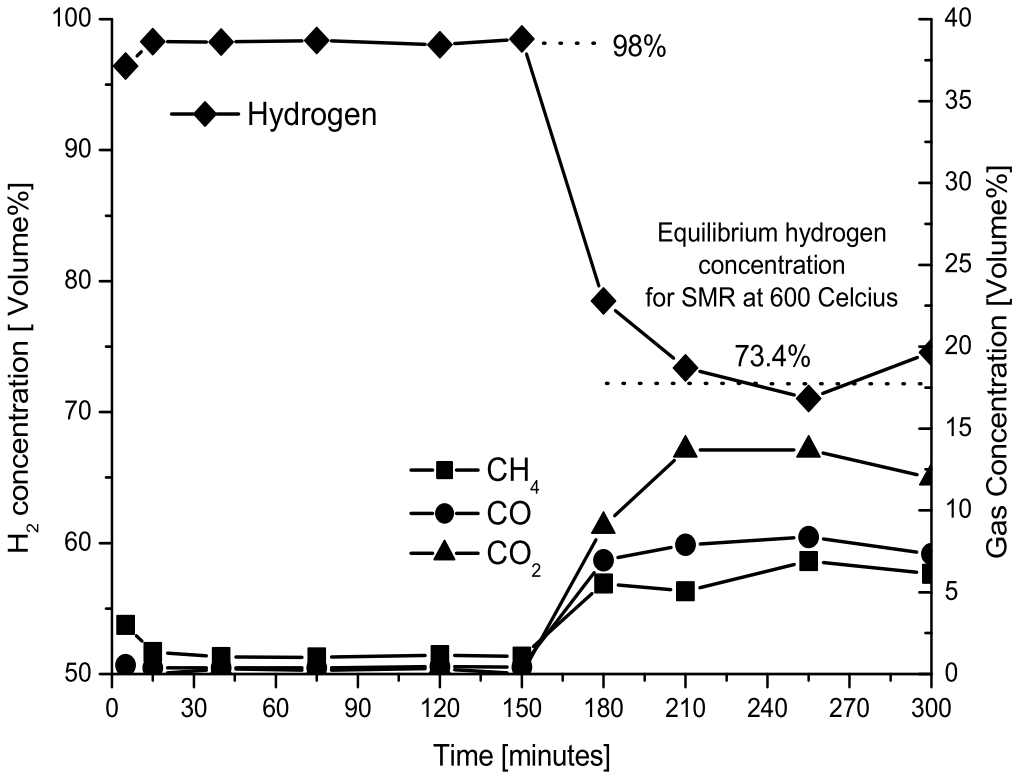

Figure 4.5: Reformer outlet composition (dry gas) as a function of time (S/C=3, U=0.032 m/s at 600°C).

where temperature uniformity is important. Two thermocouples were placed in the dense bed zone, one (T1) just above the distributor and the other (T2) 0.19 m above. Typical temperature traces for one run are shown in Figure 4.6.

The difference in temperature between the two positions, T1 and T2, was nearly constant at 3-4°C during the entire course of reaction, confirming the excellent temperature uniformity of the bubbling fluidized bed. Another feature observed from Figure 4.6 is the temperature drop after 150 minutes. This corresponds to the start of the breakthrough period also observed in Figure 4.5, caused by the diminishing exothermic carbonation reaction, while the endothermic reforming reaction continues.

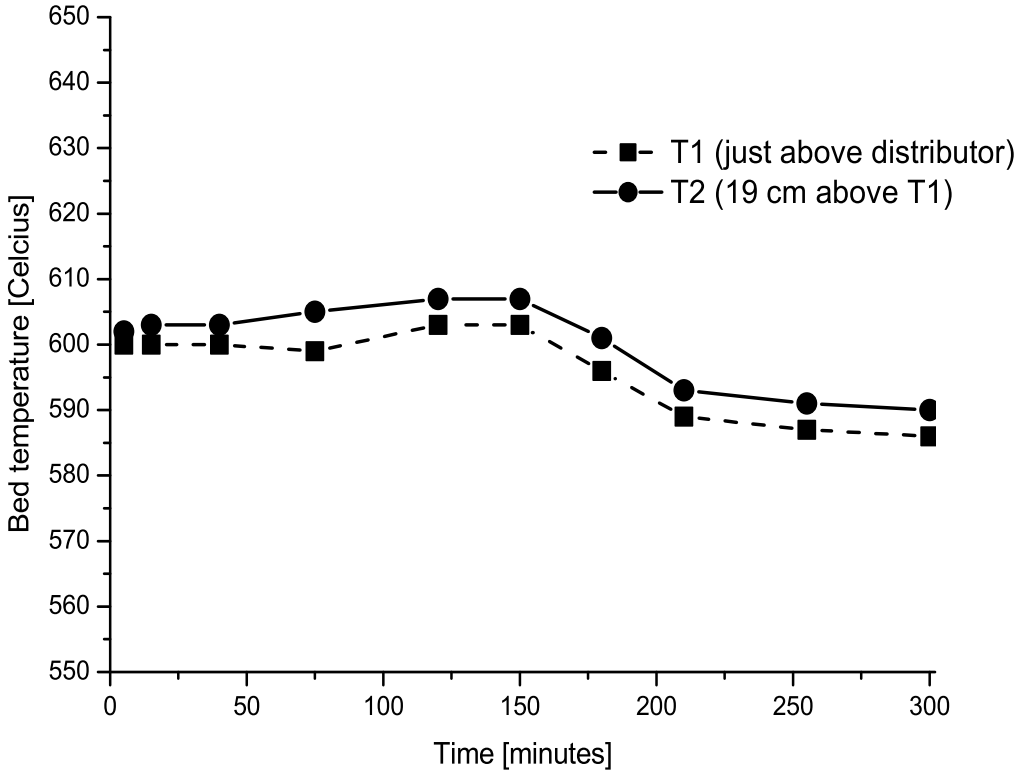

Figure 4.6: Time variation of temperature in bed zones.

Multi-cycle

In order to make the process continuous, the sorbent must be regenerated after completion of the carbonation stage. Several previous workers (e.g. Li et al.[77], Ortiz and Harrison [38], Silaban and Harrison [36]) have investigated the multi-cycle performance of CaO-based sorbents. Abanades and Alvarez [13] included previously published multi-cycle results when they reported an unavoidable decay in carbonation conversion that was dependent on the number of cycles. Most of these investigations have been carried out using TGA, either in pure CO_2 or in simulated reforming environments. There is little information on how sorption enhancement is affected by carbonation-calcination cycling in a fluidized bed.

The BFBR was operated batchwise, with periodic regeneration of sorbent without

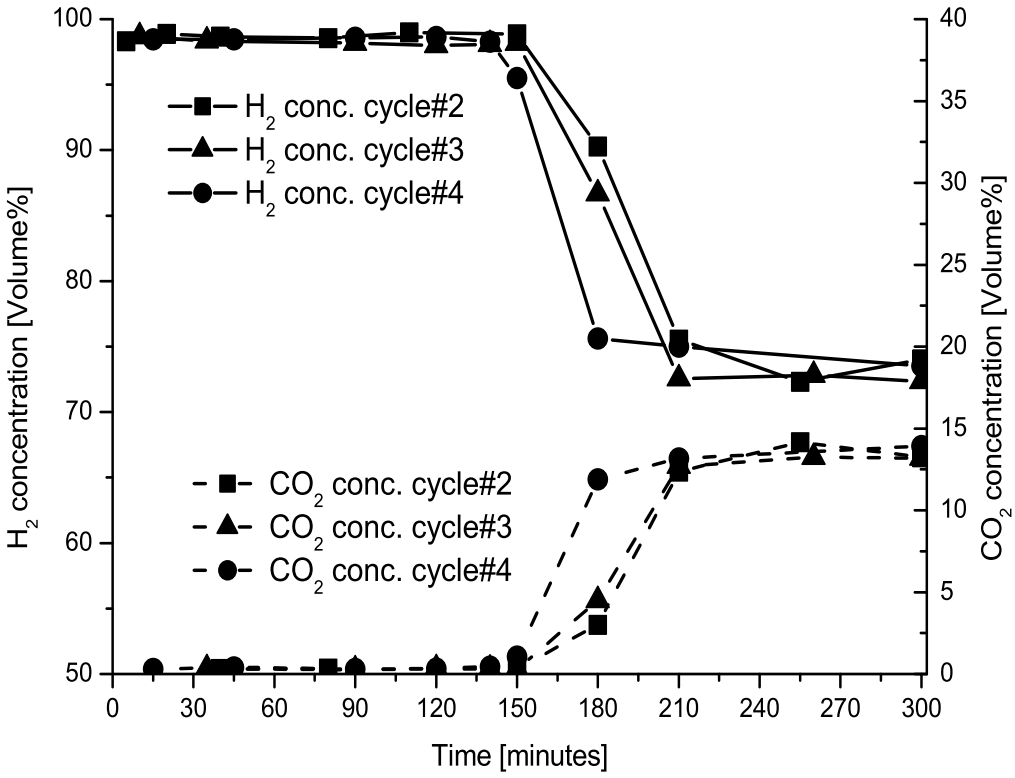

Figure 4.7: H_2 and CO_2 concentrations (dry basis) as functions of number of cycles (S/C=3, U=0.032 m/s at 600°C).

physically separating the catalyst from the dolomite. The solid mixture was exposed to hydrogen after each period of calcination to ensure that the nickel in the catalyst was in the reduced active form, corresponding to a continuous process where the solids would be exposed to a reducing atmosphere in the reformer.

Figure 4.7 shows the concentrations of hydrogen and carbon dioxide for different numbers of carbonation-calcination cycles. The first cycle is not included in this figure because the dolomite had been exposed to air, reducing its absorption capacity, hence making comparison with the other cycles difficult. It is clear from Figure 4.5 that the duration of the pre-breakthrough period is reduced somewhat with an increase in the number of cycles. This reduction is due to loss of CaO capacity, but the hydrogen concentration remained constant at 98-99%, suggesting that the equilibrium concentra-

tion of the combined reactions was reached for each cycle. The hydrogen concentration during the post-breakthrough period was again at equilibrium for successive cycles, indicating that the catalytic activity remained sufficiently high to reach equilibrium upon cycling. The breakthrough period was characterized by onset of the slow carbonation reaction rate regime, where diffusion through the solid product layer limited the rate of reaction. The slopes of the breakthrough curves indicate that the global reaction rate was not significantly affected by the number of cycles. However, the limited number of cycles and the low gas velocity in this study make it hard to conclude that the rate of reaction would in general not be affected by multi-cycling. Silaban and Harrison [36] reported that the loss of capacity was associated with a change in structural properties of the sorbent. It was claimed that reduced porosity left the interior of the sorbent particles inaccessible to CO_2. As a consequence, the CO_2 uptake capacity decreased with cycling, consistent with Figure 4.5.

Brun-Tsekhovoi et al. [34] employed relatively large dolomite particles (1.3 mm average), to facilitate their physical separation from the catalyst (250 μm) before regeneration. A separation stage should be avoided if possible as it would add extra components and complexity to the system, lead to additional attrition and cause extra heat losses. Khotomlyanskii et al. [78] studied the separation of catalyst from a heavier heat transfer agent in a fluidized bed using particles differing significantly in density and size. The catalyst density in the current study was 2200 kg/m^3, whereas the sorbent density depended on the degree of carbonation, with a possible range from 1560 kg/m^3 (fully calcined) to 2220 kg/m^3 (completely carbonated), the latter density being similar to that of the catalyst. Note that separation is more sensitive to different particle densities than to differences in particle size (Rowe and Nienow [79]). Since steam reforming catalysts commonly encounter temperatures similar to those employed in calcination, it should be possible to expose the catalyst to the calcination conditions without separation. The present investigation shows that catalytic activity remained after 4 cycles, without any separation of the particles. Nitrogen would not be used as the fluidizing gas for calcination in an industrial application, due to dilution of CO_2 leaving the regenerator for sequestration. In that case, CO_2 itself, or possibly steam, would be more realistic as the medium to avoid separation processes downstream. Silaban and Harrison [36] reported that a CO_2 atmosphere had an adverse effect on CaO sorption capacity during multi-cycling. It is therefore possible that the reduction in production time as a function of cycles, observed from Figure 4.7, would have been

greater if the carbonated sorbent had been calcined in atmospheres other than 100% N_2. However, Ortiz and Harrison [38] report no significant difference in loss of multi-cycle durability for different regeneration atmospheres, except when regeneration was carried out in pure nitrogen at 950°C, using dolomite as sorbent.

Increased superficial velocity

All multi-cycle runs were conducted at a superficial gas velocity of 0.032 m/s, a very low velocity compared to normal commercial fluidization processes. From an industrial point of view, a higher gas throughput would be advantageous. Keeping the total mass of solid constant, the superficial gas velocity was increased to see its effect. The highest gas velocity investigated was 0.096 m/s, again lower, though less so, than expected commercial velocities. However, it was desirable to investigate whether bubbles bypassing would lead to significantly lower conversions than reported for fixed bed reactors. Figure 4.8 shows the hydrogen concentration at three different superficial gas velocities.

As the gas velocity increased, the total production time decreased, as expected. The hydrogen concentration exceeded 95% on a dry basis for all three velocities. Both fresh dolomite and fresh catalyst were used for each run, making the results comparable. It is evident from Figure 4.8 that both mass transfer and reaction kinetics are fast enough to reach equilibrium within the given range of operation conditions. If there was any loss in catalyst activity, it was too small to reduce the conversion either before or after the capacity of the sorbent was exhausted. Higher velocities were not tested, but high CO_2 capture efficiencies by CaO have been reported [12] for flue gases at superficial velocities of 1 m/s, indicating that further increases in gas velocity are likely to be feasible. The experiment at U=0.064 m/s gave a somewhat lower maximum H_2 concentration than the two other runs, possibly due to the gas analysis method. There were always nitrogen peaks in the chromatograms, originating from the use of sampling bags and a syringe for manual injection into the GC, making the presence of air inevitable. The proportion of N_2 in the samples was usually 2-4 volume%, but for U=0.064 m/s a higher nitrogen concentration was observed. Hydrogen is the most volatile gas, and any leakage from a syringe or GC injection port would introduce air at the expense of hydrogen.

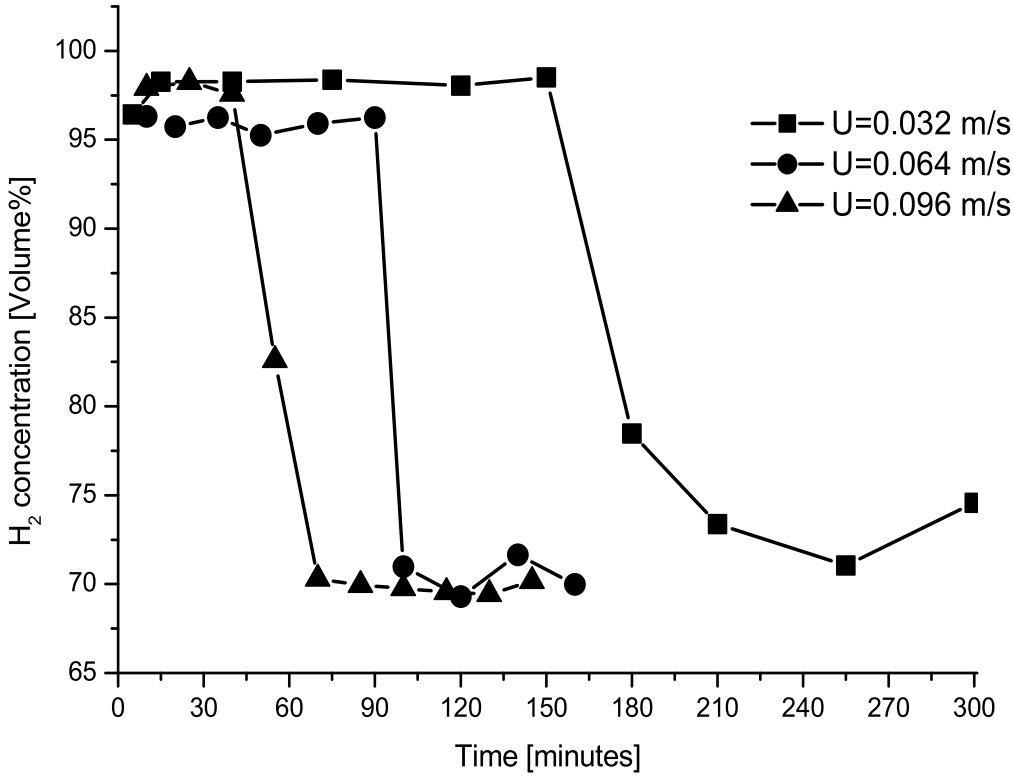

Figure 4.8: Hydrogen concentration (dry basis) in first cycle as a function of superficial gas velocity (S/C=3 and T=600°C).

Particle size distribution

The particle size distribution of the samples used in the BFBR was investigated by sieving. In order to reduce the error of analysis, sample amounts of 1.5-2 kg were used for the sieving tests. Several sieves with decreasing mesh sizes were put on top of each other and put in a "shaker machine", and the different fractions were weighted after 5 minutes of sieving. The results are presented in Figure 4.9.

Unfortunately, a narrow range particle size distribution test of the samples prior to the runs was not provided as reference samples, and only the rather coarse initial particle distribution of 125-300 μm is known. However, all three samples were crushed and sieved together making the particle size distribution comparable to each other. It

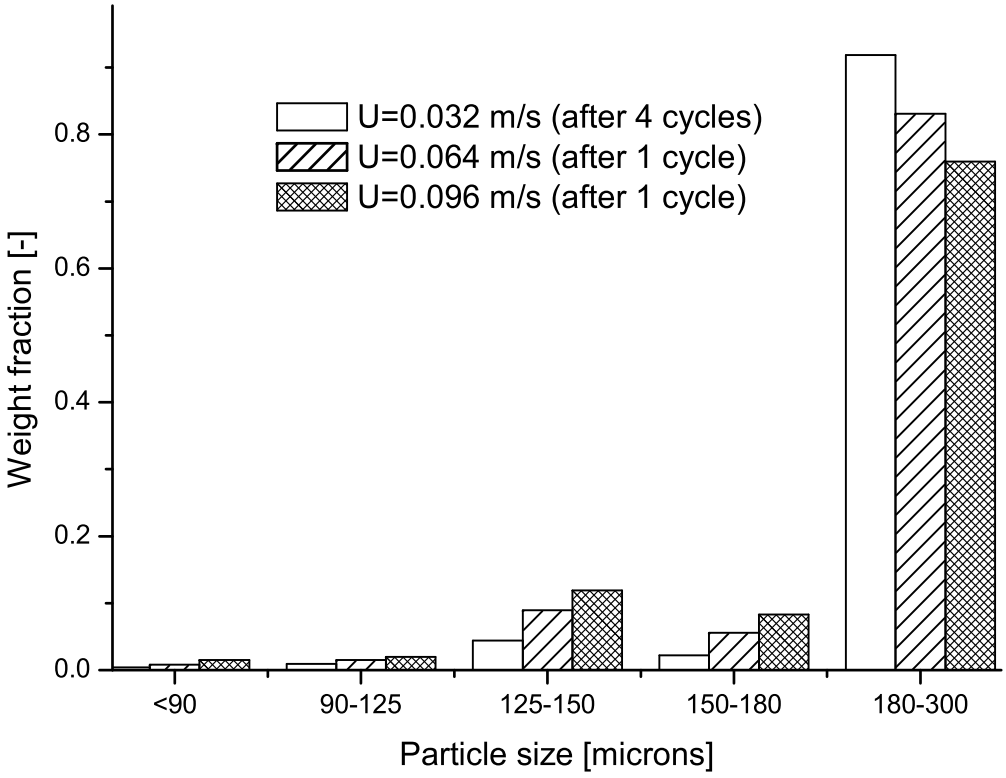

Figure 4.9: Particle size distribution of samples after BFBR runs.

is evident that the generation of fines is very low for all tests, with 1.5% of particles <90 μm being generated for the highest velocity run (U=0.096 m/s). It can be seen that the smaller particle size fractions are increased with increased gas velocity, which is as expected due to increased attrition. The sample with the lowest superficial gas velocity experienced four reforming/calcination cycles and was alternating between 600°C and 850°C with a total duration of about 30 hours, while the two other samples only experienced one cycle. Still, this sample showed the best resistance to generation of fines, with only 0.4% of the sample having a particle size below 90 μm. From this it can be understood that the effect of increased gas velocity is more critical than multiple reforming/regeneration cycles on the generation of fines.

Chapter 5

Fluidized bed modeling

A primary objective in modeling of any chemical reactor system is to represent the key physical and hydrodynamic features in a best possible manner. At the same time, it is important that models are sufficiently straightforward that their application does not demand excessive computation [61]. In this chapter, a steady-state model of a dual fluidized bubbling bed SE-SMR reactor system is investigated. The kinetics of carbonation and multi-cycle performance of Arctic dolomite, found in chapter 3, is used as input for the model. The predicted exit gas concentrations of the reformer is compared with the experimental results found in chapter 4. Circulation rates, reactant pre-heating and other operational issues are discussed with respect to system efficiency along with sorbent performance.

5.1 Bubbling bed models

Historically, two types of models have been proposed to describe the performance of fluidized bed reactors [80]:

i) Pseudo homogeneous models

ii) Two-phase models

The pseudo homogeneous models include ideal or simple one-parameter models, such as plug flow, complete mixing, dispersion and tank-in-series models. The model predictions using pseudo homogeneous models are in general discouraging, because they are

unable to account for the true flow and mixing behavior of fluidized beds. The two-phase approach, however, considers the bed to consist of at least two phases, a bubble and a dense phase (emulsion). Each phase is described by separate equations, including a term describing interfacial mass transfer. The two-phase theory states that all gas in excess of that necessary to fluidize the bed passes through the bed as bubbles. Various basic assumptions can be made on the nature of the different phases, e.g. the gas in the bubbles are often modeled as plug flow and the gas in the dense phase is modeled as stagnant or perfectly mixed. The presence of particles in the different phases is also an important feature when choosing an appropriate model. The performance of fluidized bed reactors is greatly influenced by the rate of mass transfer between the dilute phase (bubbles) and the dense phase, and some models also consider a separate cloud phase. Figure 5.1 shows a gas bubble surrounded by a cloud region.

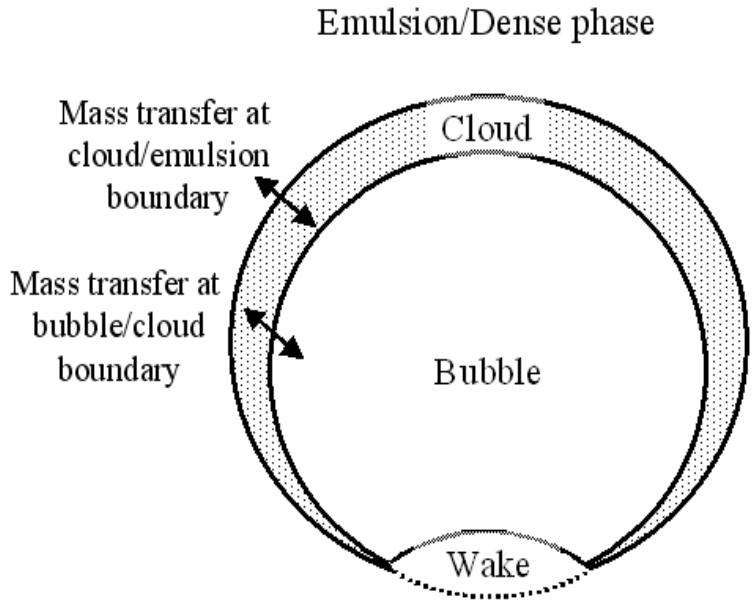

Figure 5.1: Two dimensional gas bubble in a fluidized bed [61].

The region just below the bubble is called the wake region and forms as the pressure in the bubble is less than in the nearby emulsion [64]. There are two resistances to mass transfer for cases in which cloud formation occurs [61]; at the bubble boundary and at

the cloud boundary. However, it is common that the mass transfer resistance at the cloud boundary is lumped either with the dense phase or the bubble, so that two-phase models, rather than three-phase models, can be adopted.

During the last decade, the development and availability of advanced numerical modeling software has made computational fluid dynamics (CFD) an attractive tool to simulate any process involving fluid flow. However, simultaneous modeling of flow and reaction is still a challenging problem for CFD applications.

5.1.1 The Orcutt model

In this study, a simple and widely applied two-phase model, proposed by Orcutt et al. [81], has been adopted. Figure 5.2 shows a schematic drawing of the Orcutt model.

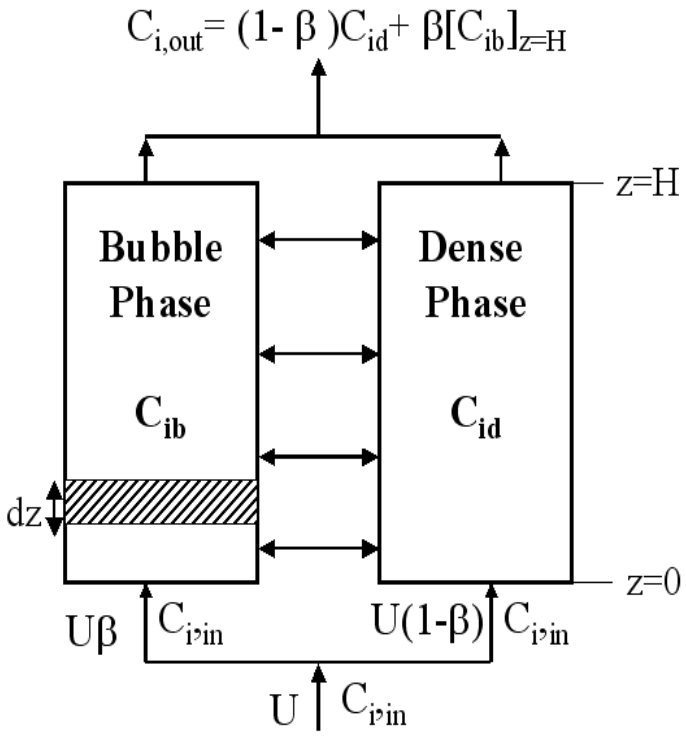

Figure 5.2: Two-phase model of Orcutt et al. [81].

The gas is assumed to be perfectly mixed in the dense phase, and the gas is assumed to be in plug flow in the bubble phase. There is no reaction taking place in the bubble phase (no particles present), and mass transfer between the two phases is represented

by an interphase mass transfer coefficient, k_q (m/s):

$$k_q = 0.75 \cdot U_{mf} + \frac{0.975 \cdot g^{0.25} \cdot D^{0.5}}{d_{eq}^{0.25}} \tag{5.1}$$

where U_{mf} is the minimum fluidization velocity (m/s), g is the acceleration of gravity (m/s^2), D is the gas phase diffusivity (m^2/s) and d_{eq} is the diameter of bubbles (m). Gas flow through the dense phase is at minimum fluidization velocity, U_{mf}, and all the excess gas is present as bubbles in the bubbling phase. The model in generalized by letting the fraction of gas which flows through the bubble phase at any height to be defined as:

$$\beta = \frac{U - U_{mf}}{U} \tag{5.2}$$

There is no reaction taking place in the bubble phase, and we can write the molar flux of specie i at any height in the bubble phase:

$$\beta \cdot U \cdot dC_{ib} = k_q \cdot (C_{id} - C_{ib}) \cdot a_b \cdot \epsilon_b \cdot dz \tag{5.3}$$

where a_b us the interfacial bubble area per unit bubble (1/m) and ϵ_b is the fraction of bed volume occupied by bubbles. The boundary condition of C_{ib} is C_{ib}=$C_{i,in}$ at z=0. For the dense phase:

$$(1-\beta) \cdot U \cdot (C_{i,in} - C_{id}) + \int_0^H k_q \cdot (C_{ib} - C_{id}) \cdot a_b \cdot \epsilon_b \cdot dz = (1-\epsilon_b) \cdot (1-\epsilon_{mf}) \cdot H \cdot R_i \tag{5.4}$$

where ϵ_{mf} is voidage at minimum fluidization and R_i is the rate of reaction (mole/(m^2·s)). The final exit concentration of i is written as:

$$C_{i,Out} = \beta \cdot [C_{ib}]_{z=H} + (1-\beta) \cdot C_{id} \tag{5.5}$$

A detailed derivation is found in Appendix C.1.

5.2 System description

A steady-state model of a dual fluidized bubbling bed SE-SMR reactor system is investigated and a schematic illustration of the process, based on parallel fluidized bed reactors, appears in Figure 5.3 .

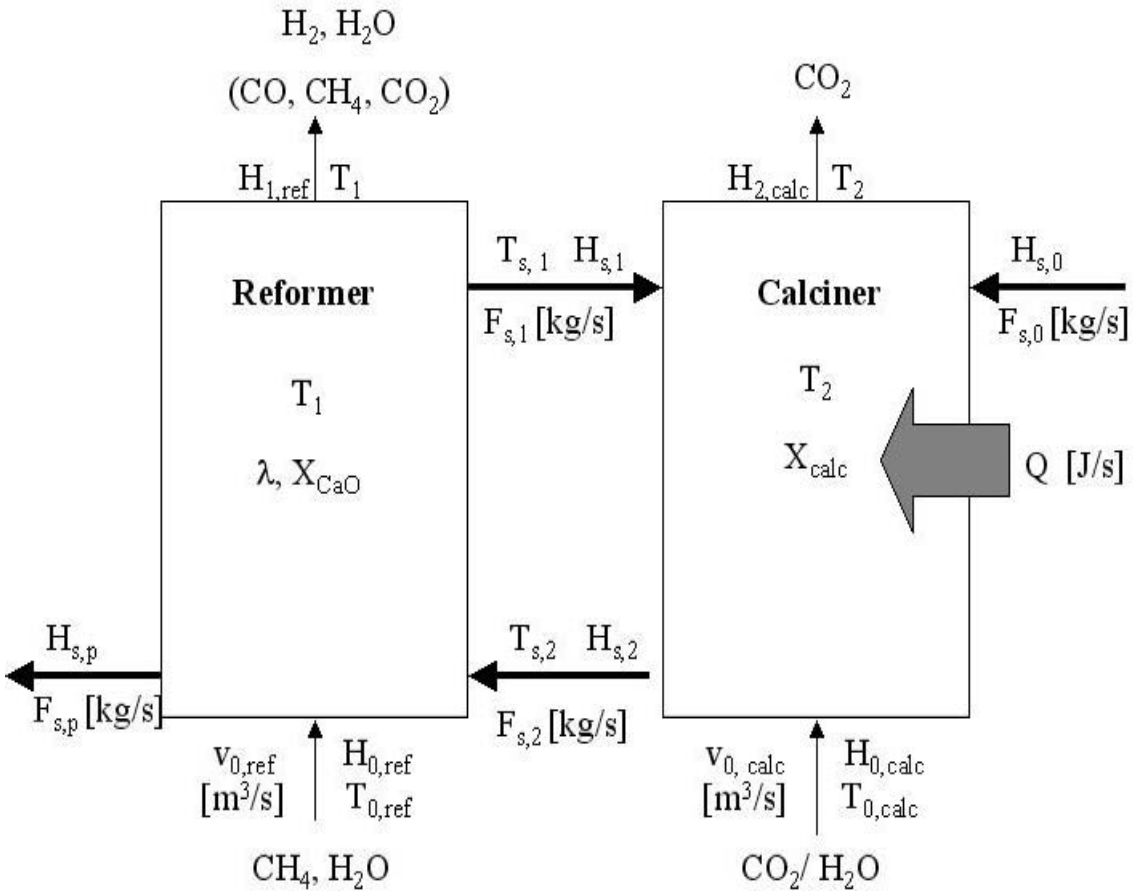

Figure 5.3: Schematic diagram of sorption-enhanced SMR process.

Reforming catalyst and CO_2-acceptor particles are mixed in the reformer (with λ as the volumetric ratio of sorbent to total volume of particles). The catalyst is a commercial Ni-based steam reforming catalyst ground to a mean particle diameter of 200 μm. It is not separated from the sorbent before being transferred to calciner. Temperature is relatively uniform due to rapid solid mixing, and solids are transferred easily between the two reactors. With almost complete CO_2 capture, the combined reactions Eq.(2.5) are slightly exothermic, eliminating the need for additional heat to

the reformer. The product gas from the reformer/carbonator then mainly consists of hydrogen and steam, with only minor quantities of CO, CO_2 and unconverted methane.

Carbonated sorbent is transferred to the calciner/regenerator where heat (Q) is supplied for the endothermic calcination reaction (Eq.(2.6)). Heat can be supplied either by burning fuel in the regenerator or by indirect heating from an external heat source. Indirect heating has the advantage of producing essentially pure CO_2 for further sequestration, e.g. suited to geological storage or enhanced oil recovery, eliminating the need for downstream purification. The SE-SMR process, illustrated in Figure 5.3, is based on pure CO_2 to be produced by the calciner. To avoid separation processes downstream, CO_2 and/or H_2O can be used as the fluidizing gas in the regenerator. Ortiz and Harrison [38] report no significant difference in loss of multi-cycle durability for different regeneration atmospheres with dolomite as sorbent, except when regeneration was carried out in pure nitrogen at 950°C. Multi-cycling was performed in the presence of reforming catalyst, which also appeared to maintain its activity.

The choice of fluidizing gas in the calciner influences the decomposition temperature of the carbonate. In pure CO_2, the decomposition temperature is ∼900°C, based on an equation proposed by Baker [42] (Eq.(2.8)). Steam as a fluidization medium has the advantage of reducing the partial pressure of carbon dioxide, hence reducing the temperature required for calcination, and it is therefore likely to be preferred over CO_2. Moreover, steam in the regeneration step proved to be advantageous in terms of sorbent multi-cycle stability, as shown in Figure 3.4 in chapter 3.

Calcium-based sorbents have the advantage of being available at a low cost, but they have proved to be unable to maintain their capture capacity over multiple reforming/regeneration cycles as shown in chapter 3. A make-up stream of fresh sorbent ($F_{s,0}$) must be included to maintain the capture capacity. The fresh sorbent is added to the calciner, whereas withdrawal is from the reformer, as indicated in Figure 5.3. Initial calcination completely decomposes both the $MgCO_3$ and $CaCO_3$, but carbonation conditions are at such high temperatures that only CaO forms carbonate. Since only CaO is considered as the active part of dolomite for CO_2-capture at the reforming temperatures, the dolomite is often referred to as CaO when considering sorbent conversion in this chapter.

A SE-SMR unit has a limited number of independent variables, such as pre-heat temperature of gas feed, volumetric feed rates of solids to the reformer and fresh sorbent addition rate. The steady-state reformer temperature (T_1) is influenced by the circu-

lation rate of solids, which in turn affects the gas conversion, CO_2 capture efficiency, calciner heat requirement, etc. Although the process layout is rather simple, with only two inter-connected vessels, the process is complex; proper design and operation require knowledge of the response to changes in the various process parameters.

5.2.1 Assumptions

Simplifying assumptions used for modeling of the reactor system are listed below.

i) Steady-state operation.

ii) Both reformer and calciner/regenerator operate in the bubbling regime at ambient pressure.

iii) Both reactors are isothermal, but they have different temperatures, T_1 and T_2. Gas and solids leave the reactor at the same temperature (T_1=$T_{s,1}$ and T_2=$T_{s,2}$). Heat loss associated with transfer of solids between the reactors is ignored, together with any other heat loss.

iv) The reformer operates under autothermal conditions. All heat needed for the reforming/sorption reactions is supplied by the hot solids from the calciner and the pre-heated feed gas.

v) The regenerator is assumed to be of the same size as the reformer. The volume of the calciner is sufficiently large to convert all $CaCO_3$ entering the regenerator to CaO (X_{calc}=*1*) at the given temperature. The fluidizing gas velocity in the reformer is set at 0.05 m/s.

vi) The calciner temperature (T_2) is calculated from the equilibrium pressure of CO_2 for the calcination reaction, with 50°C added to this temperature to assure complete calcination.

vii) Catalyst is not separated from the sorbent before entering the calciner.

viii) The reaction rates are not affected by the number of reforming/calcination cycles.

ix) A make-up flow of fresh sorbent ($F_{s,0}$) is added to compensate for the loss of sorbent capacity, and the decay is described by a simple relationship between

CaO conversion after N cycles, X_N, and cycle number, N, that was proposed by Abanades [82]:

$$X_N = f^{N+1} + b \tag{5.6}$$

where f and b are constants. This equation is used to describe the multi-cycle conversion of CaO in Arctic dolomite (Franzefoss A/S, Arctic Dolomite SHB). Thermo-gravimetric analysis was performed, with alternating carbonation and calcination in a pure CO_2 atmosphere at 850°C and 925°C, respectively. The results appear in Figure 5.4. Loss of sorption capacity as a function of carbonation/calcination cycling is evident. The constants of Eq.(5.6) were found to be f=0.82 and b=0.28 by fitting the experimental data.

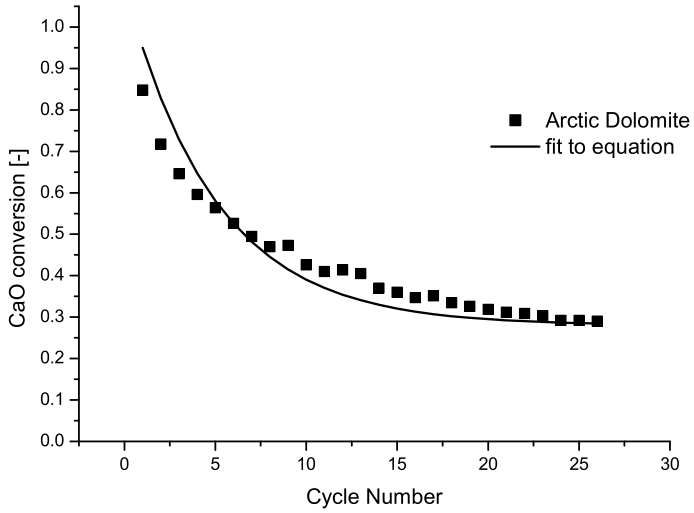

Figure 5.4: Loss of sorption capacity of CaO in dolomite as a function of number of cycles (Carbonation: 850°C in pure CO_2 for 2 hours; Calcination: 925°C in pure CO_2 for 3 hours).

x) The purge stream from the reformer is assumed to consist only of sorbent (no catalyst), requiring a dry classifier to be used in the process.

5.2.2 Model equations

To solve the system involving both catalytic reactions and a consumable solid, it is necessary to write separate mole balances for the gaseous phase and the solid phase. There are five gas species involved in the reactions, i.e. CH_4, H_2O, CO, CO_2 and H_2. The two-phase model of Orcutt et al. [81], previously described in this chapter, is used to model the reformer. This assumes the gas to be perfectly mixed in the dense phase, whereas it is in plug flow in the bubble phase, and mass transfer between the two phases is represented by an interphase mass transfer coefficient, k_q (Eq.(5.1)). Other hydrodynamic- and mass transfer correlations used in the model are listed in Table 5.1.

Table 5.1: Hydrodynamic and mass transfer relationships

Parameters	**Relationship**	**Reference**
Bubble size. Evaluated at z=0.4· H_{mf}[a]	$d_{eq} = d_{bm} - (d_{bm} - d_{b0}) \cdot \exp(\frac{-0.3 \cdot z}{d_t})$ where $d_{b0} = \frac{2.78}{g} \cdot (U - U_{mf})^2$ and $d_{bm} = 0.65 \cdot [\frac{\pi}{4} \cdot d_t^2 \cdot (U - U_{mf})]^{0.4}$	Mori and Wen [83]
Interfacial bubble area per unit volume	$a_b = \frac{6}{d_b}$	
Voidage fraction of bubbles in bed	$\epsilon_b = \frac{U - U_{mf}}{U_A}$	
Absolute bubble rise velocity	$U_A = 0.711 \cdot \sqrt{g \cdot d_{eq}} + (U - U_{mf})$	Davidsion and Harrison [84]
Minimum fluidization velocity of a binary system	$Ar = \frac{d_{p,mix}^3 \cdot \rho_f \cdot (\rho_m - \rho_f) \cdot g}{\mu^2}$ $\frac{d_{p,mix}^3 \cdot U_{mf} \cdot \rho_f}{\mu} = [(33.7)^2 + 0.0408 \cdot Ar]^{0.5} - 33.7$ where $\frac{1}{\rho_{mix}} = \frac{\omega_c}{\rho_{cat}} + \frac{\omega_d}{\rho_{dolomite}}$, and $\frac{1}{\rho_{mix} \cdot d_{p,mix}} = \frac{\omega_c}{\rho_{cat} \cdot d_{p,cat}} + \frac{\omega_d}{\rho_{dolomite} \cdot d_{p,dolomite}}$	Wen and Yu [85] and Goossens et al. [86]

[a] Average bubble size at 40% of bed height

Mole balances for species, i, in the bubbles and dense phase are given by Eqs.(5.3-5.4). CO_2 is the only gas species consumed in the gas-solid reaction. Its rate of dis-

appearance via the carbonation reaction must be included in the dense phase mole balance. And the reaction rate term, R_i (mole/m^3 solids/s), of Eq.(5.4) is expressed as:

$$R_i = (1-\lambda)\cdot\rho_{cat}\cdot r_i\cdot\frac{1000}{3600} \tag{5.7}$$

for i=CH_4, CO, H_2, H_2O

$$R_i = (1-\lambda)\cdot\rho_{cat}\cdot r_i\cdot\frac{1000}{3600} + \lambda\cdot r_i^{'} \tag{5.8}$$

for i=CO_2

The reaction rates for the catalytic reactions are denoted by r_i, whereas the gas-solid reaction rate is designated by $r_i^{'}$. The previous derived carbonation reaction expression in Eq.(3.8) is used for describing carbonation of Arctic dolomite. The rate expressions for catalytic steam reforming of methane over a nickel-based catalyst are those proposed by Xu and Froment [87] who used the same Ni/$MgAl_2O_4$ catalyst as is employed in this study and investigated temperatures in the range of 773-848 K, typical of temperatures for SE-SMR. The rate expressions were obtained under pressurized conditions, and validity in the atmospheric carbonator-reformer is assumed. The rate expressions for reactions, Eqs.(1.1-1.3), are, respectively, given by:

$$r_1 = \frac{k_1}{p_{H_2}^{2.5}}\cdot[p_{CH_4}\cdot p_{H_2O} - \frac{p_{H_2}^3\cdot p_{CO}}{K_1}]/DEN^2 \tag{5.9}$$

$$r_2 = \frac{k_2}{p_{H_2}}\cdot[p_{CO}\cdot p_{H_2O} - \frac{p_{H_2}\cdot p_{CO}}{K_2}]/DEN^2 \tag{5.10}$$

$$r_3 = \frac{k_3}{p_{H_2}^{3.5}}\cdot[p_{CH_4}\cdot p_{H_2O}^2 - \frac{p_{H_2}^4\cdot p_{CO_2}}{K_1\cdot K_2}]/DEN^2 \tag{5.11}$$

where $DEN = 1 + K_{CO}\cdot p_{CO} + K_{H_2}\cdot p_{H_2} + K_{CH_4}\cdot p_{CH_4} + \frac{K_{H_2O}\cdot p_{H_2O}}{p_{H_2}}$. The values of the kinetic parameters are listed in Table 5.2 and the total generation- and removal rates are written as:

$$
\begin{aligned}
r_{CH_4} &= -r_1 - r_3 \\
r_{H_2O} &= -r_1 - r_2 - 2 \cdot r_3 \\
r_{CO} &= r_1 - r_2 \\
r_{H_2} &= 3 \cdot r_1 + r_2 + 4 \cdot r_3 \\
r_{C0_2} &= r_2 + r_3 \\
r^{'}_{C0_2} &= -R_{dolo}(X)
\end{aligned}
\tag{5.12}
$$

Table 5.2: Kinetic parameters from Xu and Froment [87]

Rate constants	**Pre-exponential factor**	**Activation energy and heat of chemisorption [kJ/mole]**
k_1 $[\frac{\text{kmole}\cdot\ \text{kPa}^{0.5}}{\text{kg cat}\cdot\ \text{h}}]$	$9.49\cdot\ 10^{16}$	240.1
k_2 $[\frac{\text{kmole}}{\text{kg cat}\cdot\ \text{h}\cdot\ \text{kPa}}]$	$4.39\cdot\ 10^{4}$	67.13
k_3 $[\frac{\text{kmole}\cdot\ \text{kPa}^{0.5}}{\text{kg cat}\cdot\ \text{h}}]$	$2.29\cdot\ 10^{16}$	243.9
K_{CH_4} $[\text{kPa}^{-1}]$	$6.65\cdot\ 10^{-6}$	38.28
K_{CO} $[\text{kPa}^{-1}]$	$8.23\cdot\ 10^{-7}$	70.65
K_{CH_4} [-]	$1.77\cdot\ 10^{5}$	-88.68
K_{H_2} $[\text{kPa}^{-1}]$	$6.12\cdot\ 10^{-11}$	82.9
Equilibrium constants		
K_1 $[\text{kPa}^2]$	$K_1 = 10267\cdot\ 10^{\frac{-26830}{T}+30.11}$	
K_2	$K_2 = 10^{\frac{4400}{T}-4.036}$	

Mole balances

Calcined dolomite consists of CaO and inert material (mainly MgO), which is uniformly distributed in the dolomite pellet. Y_{CaO} and Y_{MgO} represent the weight percentages of CaO and MgO, respectively, in calcined Arctic dolomite. $F_{s,2}$ is the total mass flow of calcined dolomite from the calciner and is the sum of recycled sorbent, $F_{s,r}$, and fresh added sorbent $F_{s,0}$. Fresh sorbent is introduced to the calciner as $CaCO_3 \cdot MgCO_3$ and must be fully calcined before entering the reformer. The calcination of freshly added dolomite therefore adds to the energy requirement of the calciner. The catalyst is not

separated from the mixture before entering the calciner, so that the solid circulation includes catalyst. The solid streams between the reactors are listed in Table 5.3.

Table 5.3: Solid stream relationships

To reformer [kg/s]	**To calciner [kg/s]**
$F_{s,2}=F_{s,0}+F_{s,r}$	$F_{s,1}=F_{s,r}$
$F_{CaO,2}=F_{s,2}\cdot Y_{CaO}\cdot X_{calc}$	$F_{CaO,1}=F_{s,r}\cdot Y_{CaO}\cdot X_{calc}\cdot(1-X_{CaO})$
$F_{CaCO_3,2}=0$	$F_{CaCO_3,2}=F_{s,r}\cdot Y_{CaO}\cdot\frac{M_{CaCO_3}}{M_{CaO}} X_{CaO}$
$F_{MgO,2}=F_{s,2}\cdot Y_{MgO}$	$F_{MgO,1}=F_{s,r}\cdot Y_{MgO}$
$F_{cat,2}=F_{s,r}\cdot\frac{\omega_c}{1-\omega_c}$ [a]	$F_{cat,1}=F_{cat,2}$

[a] $\omega_c = \frac{(1-\lambda)\cdot\rho_{cat}}{(1-\lambda)\cdot\rho_{cat}+\lambda\cdot\lambda_{dolo}}$

A mole balance on CaO in the solid dolomite, continuously added and withdrawn from the reformer, has to be included:

moles CaO in - moles CaO out = moles CaO reacted

$$\frac{F_{CaO,2}}{M_{CaO}}\cdot X_{CaO} = -R_{dolo}(X)\cdot V_{dolomite} \tag{5.13}$$

The CO_2 conversion in the gas phase and solids conversion satisfies the equation:

Number of moles CO_2 consumed = number of moles CaO consumed

$$X_{CO_2}\cdot C_{CH_{4,in}}\cdot U\cdot A_c = \frac{F_{CaO,2}}{M_{CaO}}\cdot X_{CaO} \tag{5.14}$$

The solid conversion is calculated based on the reaction kinetics. However, there is an upper limit for solid conversion as the CaO sorption capacity dramatically decreases as a function of the number of cycles (as shown in Figure 5.4). The amount of fresh sorbent,

$F_{s,0}$, to be added to the system is calculated from a population balance, combined with the empirical Eq.(5.6) based on the work of Abanades [82] and should satisfy the equation:

$$X_{CaO} = \frac{f \cdot F_{s,0}}{F_{s,0} + F_{s,r} \cdot (1-f)} + b \tag{5.15}$$

If no fresh sorbent is added, this equation predicts that the steady-state conversion approaches 28%, which is consistent with the findings from the 100 multi-cycle test presented in Figure 3.4.

Enthalpy balances

Both reactors operate isothermally, and enthalpy balances are used to calculate the steady-state temperatures of the reactors. These balances have to be solved simultaneously with the mole balances in an iterative manner, as the solid outlet temperature of each reactor is required as an input to the other reactor. For component, i, without any phase change, the enthalpy at temperature T is given by:

$$H_i^{\circ}(X) = H_i^{\circ}(298) + \int_{298}^{T} C_{P,i} \cdot dT \tag{5.16}$$

The heat capacity is a function of temperature expressed by:

$$C_{P,i} = A_i + B_i \cdot T + \frac{C_i}{T^2} + D_i \cdot T^2 \tag{5.17}$$

The constants in Eq.(5.17) are obtained from the thermodynamic software program HSC Chemistry (HSC Chemistry 5.1, Outokumpu Research Oy, Finland), and listed in Appendix C.2. The enthalpy of the solids entering the reformer is calculated from:

$$H_{s,2} = F_{CaO,2} \cdot \Delta H_{CaO,2} + F_{CaCO_3,2} \cdot \Delta H_{CaCO_3,2} + F_{MgO,2} \cdot \Delta H_{MgO,2} + F_c \cdot \Delta H_{Catalyst,2} \tag{5.18}$$

For the reformer the enthalpy balance to be solved is:

$$(H_{s,1} + H_1 + H_{s,p}) - (H_{s,2} + H_{s,ref}) + \Delta H_{rx,reformer} = 0 \tag{5.19}$$

where $\Delta\ H_{rx,reformer}$ is the sum of the heats of reaction for the endothermic reforming reactions

$$\Delta H_{rx,reformer} = V_{Bed} \cdot (1-\epsilon_b) \cdot (1-\epsilon_{mf}) \cdot [\rho_{cat} \cdot (1-\lambda) \cdot \sum_{j}^{3} \Delta H_{rx,j} \cdot R_j + \lambda \cdot \Delta H_{rx,4} \cdot R_{dolo}(X)] \tag{5.20}$$

with

$\Delta H_{rx,1}$=206.2$\frac{kJ}{mole}$, $\Delta H_{rx,2}$=-41.1$\frac{kJ}{mole}$, $\Delta H_{rx,3}$=164.9$\frac{kJ}{mole}$,

$\Delta H_{rx,4}$=-178.8$\frac{kJ}{mole}$, $\Delta H_{rx,5}$=-100.9$\frac{kJ}{mole}$

For the calciner:

$$(H_{s,2} + H_2) - (H_{s,0} + H_{s,1} + H_{0,calc}) + \Delta H_{rx,calciner} = 0 \tag{5.21}$$

The heat of reaction for $\Delta H_{rx,calciner}$ is the sum of the endothermic calcination reaction of $CaCO_3$. Note that the heat of decomposition of $MgCO_3$, $\Delta H_{rx,5}$, is included for fresh dolomite added to the system.

5.2.3 Solving the system of equations

The model consists of a set of highly nonlinear algebraic equations. Mole balances and enthalpy balances for both reactors were solved simultaneously to obtain steady-state solutions for the system. The calculation procedure was iterative, implemented in MATLAB (MATLAB 6.5, The MathWorks, Inc.). The numerical solution procedure is:

i) Guess an initial temperature of solids entering the reformer from the calciner, $T_{s,2}$ (assumed equal to T_2).

ii) Calculate T_1 from the mole and enthalpy balances with the above temperature as input.

iii) Use calculated reformer temperature, T_1, as input to the energy balance in the calciner to calculate an improved value of the calciner temperature T_2. (No mole balance for the calciner is needed here, just the assumption that X_{calc}=1.)

iv) Compare the calculated T_2 from the energy balance with the initial guess value. A steady-state solution is reached when the calciner temperature is equal to the temperature of the solids entering the reformer.

Figure 5.5 shows a simplified block diagram of the model.

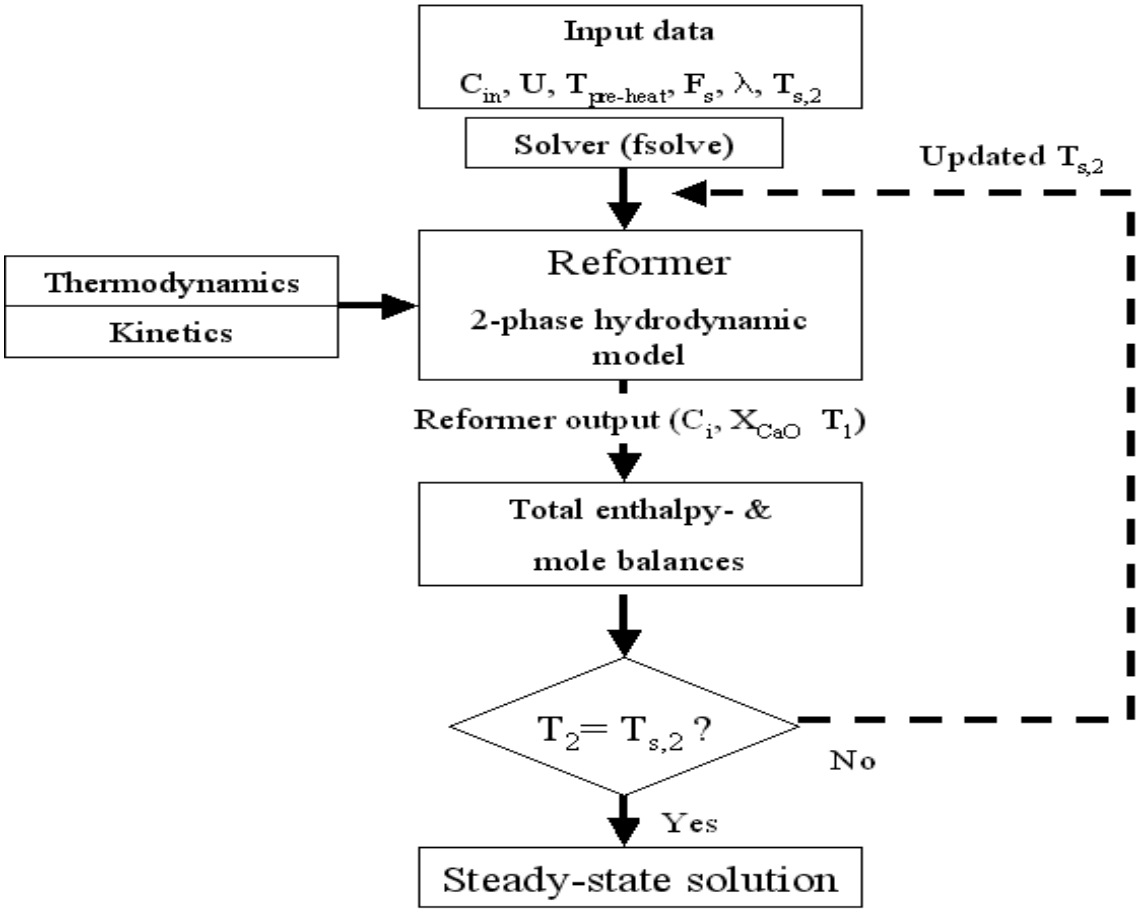

Figure 5.5: Simplified block diagram of solution procedure.

Evaluation parameters

Product gas purity and dry gas hydrogen concentration are key parameters in evaluating the performance of the process. Other important parameters include hydrogen yield (moles hydrogen produced/moles methane fed), Y_{H_2}, and carbon capture efficiency (moles CO2 captured/moles carbon fed), X_{CO_2}. The reformer efficiency is defined as in the work of Rydén and Lyngfelt [88]. A H_2-equivalent term, $H_{2,eq}$, describes the amount of hydrogen remaining per mole of CH_4 fed if all external heat and power demands were to be met using the produced H_2 for heating and power production.

$$H_{2,eq} = Y_{H_2} - H_{2,calciner} + H_{2,steam} - H_{2,compression} \tag{5.22}$$

A reformer efficiency is defined as:

$$\eta_r = H_{2,eq} \cdot \frac{LHV_{H_2}}{LHV_{CH_4}} \tag{5.23}$$

where
$H_{2,calciner} = \frac{Q_H}{LHV_{H_2}}$, $H_{2,steam} = \frac{Q_S \cdot 0.9}{LHV_{H_2}}$, $H_{2,compression} = \frac{Q_C}{LHV_{H_2}}$

Q_H is the heating demand of the calciner (J/mole CH_4), and Q_S is the heating excess of the streams entering and leaving the system. A steam generation efficiency of 90% is assumed. Q_C is the electricity needed to compress the product gases (both H_2 and CO_2). If the process produces excess heat and power, then $H_{2,eq}$ exceeds the actual hydrogen product. The lower heating values (LHV) for hydrogen and methane are 241.8 kJ/mole and 802.3 kJ/mole respectively. Rydén and Lyngfelt assumed that the electrical energies required to compress CO_2 and H_2 to 20 and 100 bar are 15 kJ/mole and 13 kJ/mole, respectively, and these values have also been adopted.

5.3 Model results and discussion

Unless otherwise stated the reactor dimensions used in the previous batch experiments were employed for the calculations, as listed in Table 4.1.

5.3.1 Effect of sorbent addition

Hydrogen concentration is predicted as a function of reactor length for three values of λ in Figure 5.6 for a reformer temperature of 600°C, a steam-carbon ratio of 3 and a superficial gas velocity of 0.1 m/s.

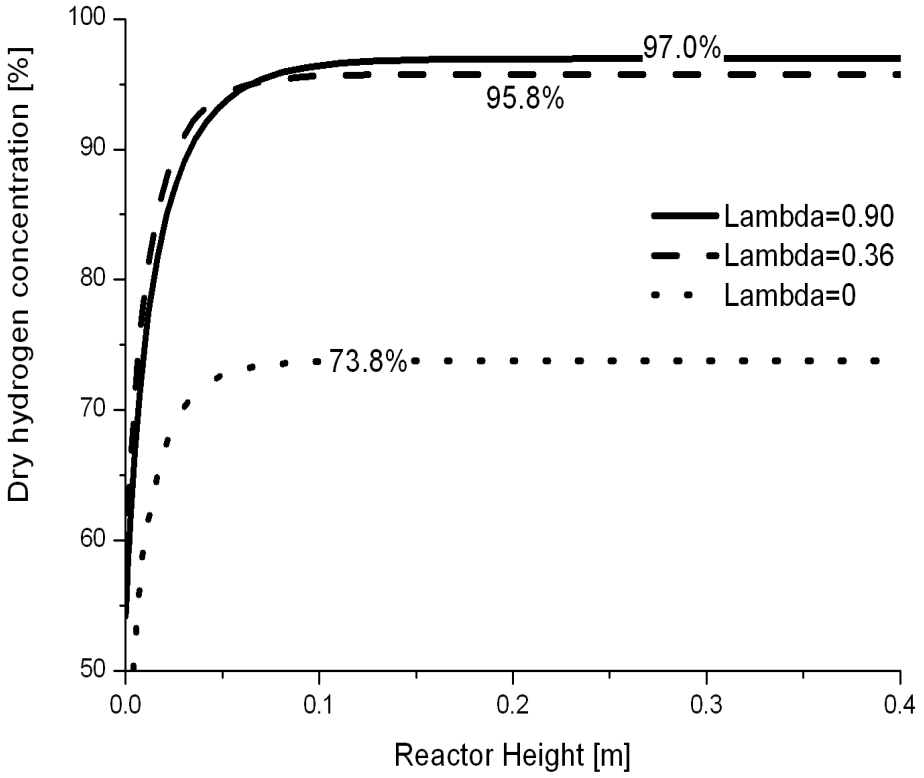

Figure 5.6: Effect of sorbent addition on exit hydrogen concentration (T_1=600°C, S/C=3, U=0.1 m/s).

An equilibrium dry hydrogen concentration of 73.8% is reached after traversing

$\sim$0.07 m when no sorbent is added (λ=0). When sorbent is added to the reactor, the hydrogen concentration increases to 95.8% and 97.0% for λ=0.36 and λ=0.90 respectively, showing the shift in equilibrium product composition.

A dry hydrogen concentration of $\sim$98% for λ=0.36 was found experimentally at the same reaction conditions, as reported in chapter 4. The under-prediction by the model may be related to the hydrodynamic model, in particular the fact that solids are not accounted for in the bubbles. Improved models are available [61, 89] which include a small portion of the solids within the bubbles. However, given the predicted leveling out of all three curves with height, the difference between the predictions and experimental results in this case is primarily related to the equilibrium approached, not the kinetic model. The temperature in the freeboard region was hotter than the actual bed temperature for the experimental investigation and additional reactions in this region of the reactor are likely to cause increased methane conversion. The relatively low ratio of λ=0.36 was chosen to give reasonable production times, as the experiments were conducted in batch mode. Previous workers, e.g. Ortiz and Harrison [38] used a dolomite-catalyst mass ratio of 2.2-2.7, corresponding to $\lambda\approx$0.8. To minimize the requirement for expensive catalyst, operation with high λ is desirable. For λ=0.90 a hydrogen concentration of 97% is predicted in the product gas. A further increase led to a drop in the predicted hydrogen concentration, indicating that at least 10% catalyst by volume is required to maximize the hydrogen yield and reduce the catalyst cost.

The observed "breakthrough", found from the experimental investigation, occurred somewhere between 40-55 minutes for U$\approx$0.1m/s. For this superficial gas velocity the total carbon feed rate is calculated to $2.9\cdot10^{-3}$ moles/s. Assuming that 95% of the carbon fed to the reformer is converted to CO_2 and reacted to form $CaCO_3$, the amount of unreacted sorbent at the point before the experimental breakthrough (40 minutes) is 280 g, corresponding to a solid conversion of 69%. Figure 5.7 shows the experimental hydrogen concentration compared with model predictions at different degree of sorbent conversion using the steady-state model. The point of breakthrough at 55 minutes is also modeled, corresponding to 95% conversion. The predicted dry hydrogen outlet concentration is somewhat lower than the experimental for the pre-breakthrough period. However, the kinetics and model predictions are quite consistent with the batch experiments.

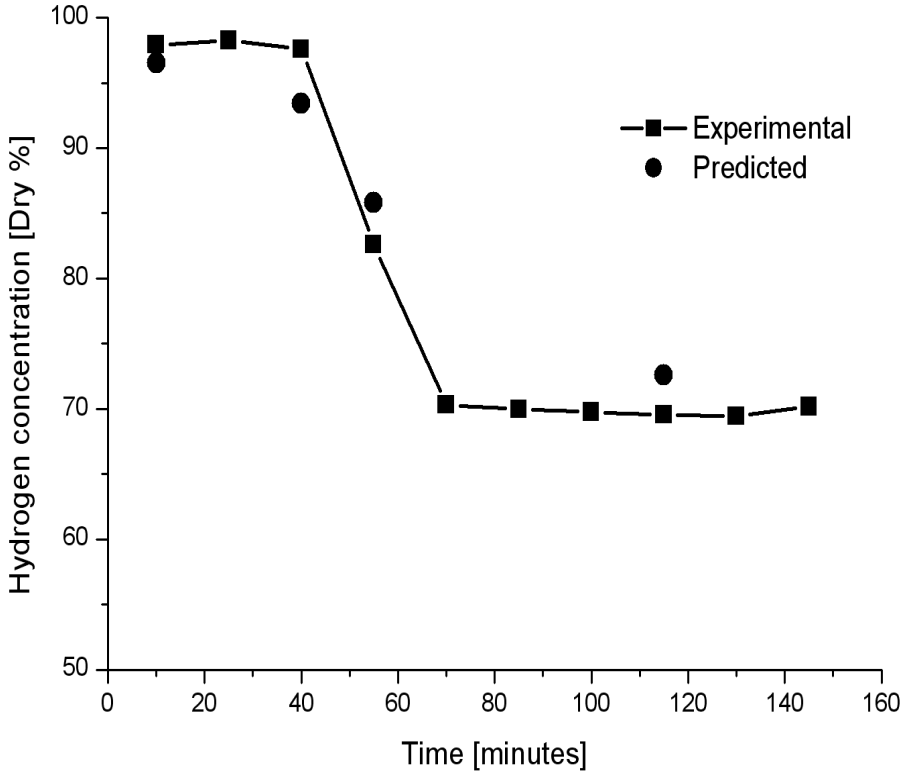

Figure 5.7: Experimental and predicted hydrogen concentration (T_1=600°C, S/C=3, U=0.1 m/s).

Effect of S/C-ratio

The effect of increased steam-to-carbon (S/C) ratio on outlet hydrogen concentration is shown in Figure 5.8. The ratio is varied over the range 3-4, the likely range of interest to minimize carbon formation while not requiring excessive energy for steam generation. The hydrogen concentration is predicted to increase from 97.0% to 98.4% as the S/C-ratio is varied from 3 to 4. This increase is related to the positive effect on the water-gas shift reaction (WGS) equilibrium, which favors production of H_2 and CO_2. Increased CO_2 partial pressure increases the rate of carbonation, further enhancing the steam reforming reaction.

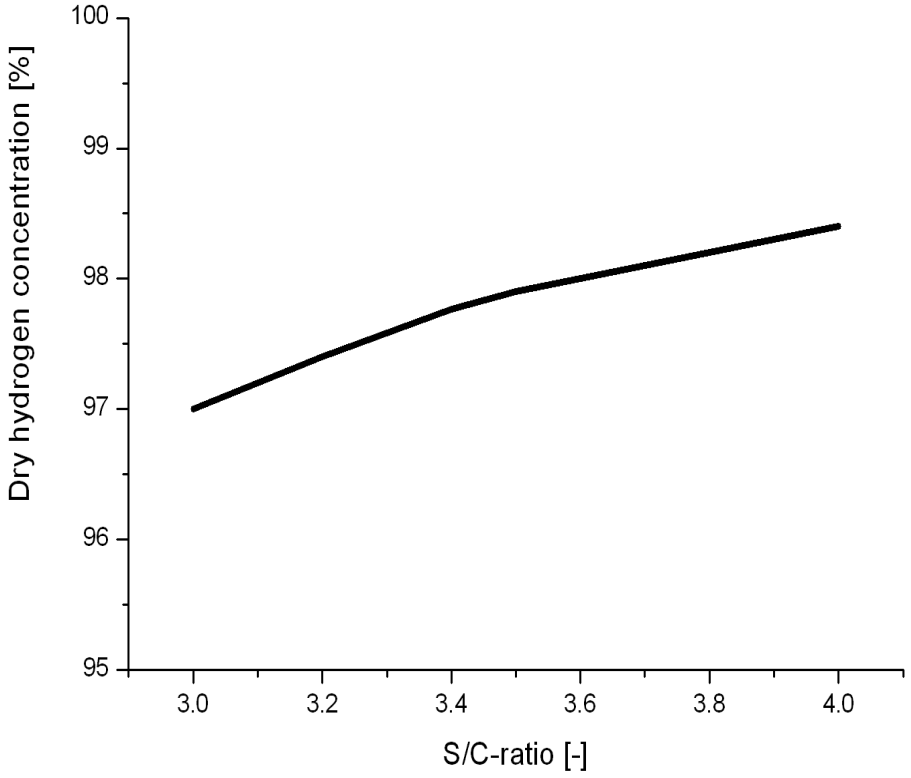

Figure 5.8: S/C-ratio effect on reformer hydrogen purity (T_1=600°C, λ=0.9, U=0.1 m/s).

5.3.2 System considerations

Based on the above findings, a steam-to-carbon ratio of 4 and λ=0.90 were chosen for the remaining simulations. The scale of the reformer/regenerator system was increased to a reactor diameter of 1 m. The static bed height of the shallow bubbling bed was slightly increased to 0.35 m to compensate for bigger bubbles. The velocity of 0.1 m/s is low when considering the practical application of the process. However, the velocity is within the bubbling regime, suiting the hydrodynamic two-phase model.

The concentration of hydrogen in the reformer depends on the rate of reaction of the combined reactions, which are strongly related to reformer temperature and solid conversion. Increasing the solid circulation rate leads to increased reformer temperature

as more hot solids are added from the calciner. Figure 5.9 shows how the reformer temperature, solid conversion and dry hydrogen mole concentration in the product gas are affected by increased circulation rate.

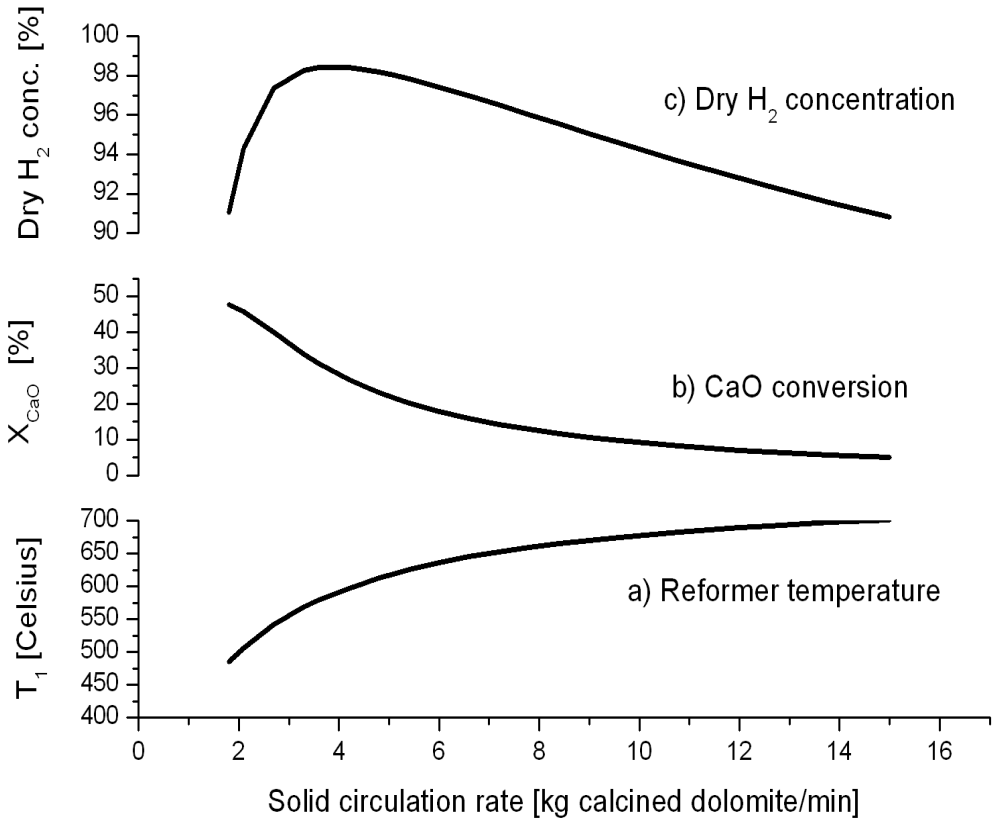

Figure 5.9: Reformer temperature (a), solid conversion (b) and dry hydrogen mole concentration (c) in reformer product gas as a function of circulation rate for S/C=4, λ=0.9 and $T_{0,ref}$=250°C.

It can be observed from Figure 5.9 that a reformer temperature in the range 550-620°C is optimal for obtaining a high hydrogen concentration in the product gas (>98%). In order to achieve this, the circulation rate of calcined dolomite has to be within the 3 to 5 kg/min range for this size of reactor and a pre-heating temperature of 250°C. The temperature effect on the combined reactions is rather complex. Increased temperature leads to an increased steam reforming reaction rate, whereas the rate of carbonation increases to a certain point before the reaction rate decreases

due to the drop in equilibrium constant, i.e. due to the reverse calcination reaction, as can be seen from the rate expression for carbonation in Eq.(3.8) used in the modeling, where the difference in partial CO_2 pressure and the equilibrium pressure at the given temperature represents the "driving force" for reaction. The circulation rate not only influences the reformer temperature, but also the solid conversion (Figure 5.9b). Solid conversion is dependent on residence time in the reformer, and a low solids conversion of 20-30% is achieved for the circulation rates, giving the maximum hydrogen concentration observed at $> 98\%$ H_2. High circulation gives a low fractional conversion of the sorbent, in addition to increased temperature. The reformer temperature can also be adjusted by varying the reactant pre-heating. By employing higher pre-heating temperatures ($T_{0,ref}$), the circulation rate can be reduced in order to reach the optimum reaction temperature for the combined reactions. Figure 5.10 shows how dry hydrogen concentration is affected by solid conversion and reformer temperature for two different pre-heating temperatures.

The higher pre-heating temperature of 500°C requires a lower solid circulation to achieve proper reaction temperatures; hence a steady-state solid conversion of 50-60% is reached at reforming temperatures close to 600°C. For a pre-heating temperature of 250°C, the same reforming temperature is reached at lower solid conversions of 20-30%. The maximum hydrogen concentration is also somewhat higher for the lowest pre-heating temperature. This can be understood by looking at the nature of the carbonation reaction, with a rapid initial reaction rate followed by a slower regime in which the rate is controlled by CO_2 diffusion through the $CaCO_3$ product layer. A reaction temperature of $\sim$600°C can be maintained by adjusting the circulation rate of hot solids entering the reformer in combination with pre-heating of the feed gas. If an increased circulation rate is used to raise the reformer temperature, more heat must be supplied to the calciner, thereby reducing the total system efficiency. However, this leads to a lower sorbent conversion in the reformer, utilizing the fast reaction regime, and the need for fresh sorbent addition is reduced. The effect of circulation rate on solid conversion and reformer efficiency is shown in Figure 5.11.

It seems that reformer efficiencies of about 86% can be achieved for moderate circulation rates of calcined dolomite of 4-6 kg/min. Efficiencies are reduced at low circulation rates due to the need to add more fresh sorbent to the calciner, requiring more heat to pre-calcine fresh dolomite. This is clearly seen in Figure 5.11, where there is a marked drop in reformer efficiency for CaO conversions exceeding 28%. The $MgCO_3$ uncalcined

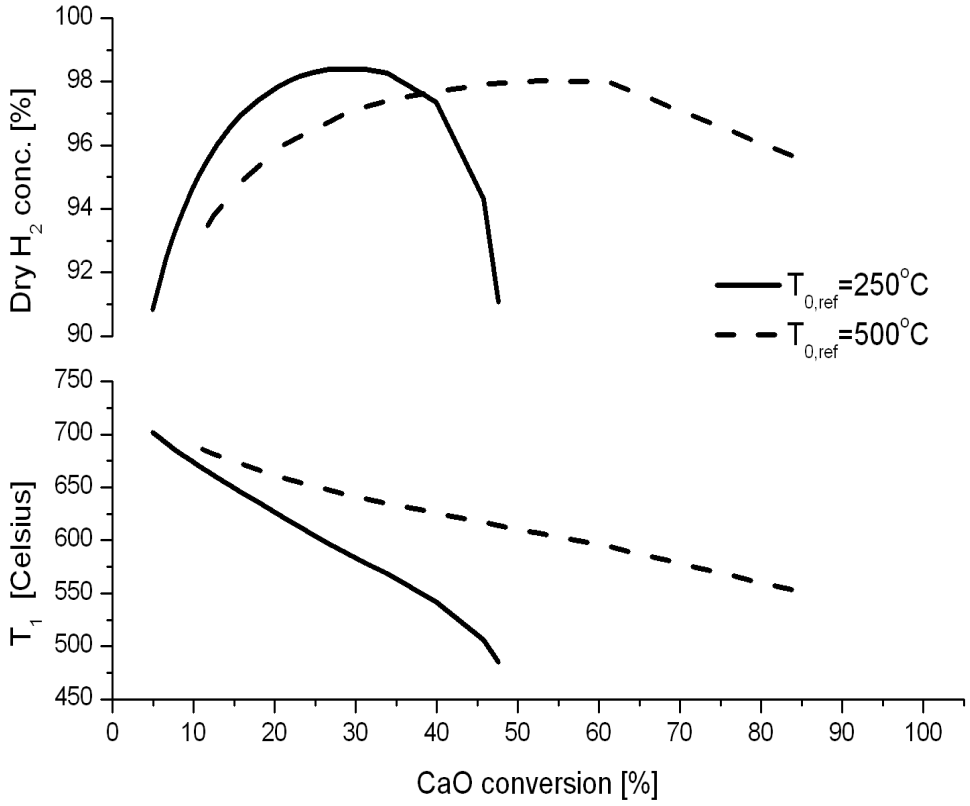

Figure 5.10: Reformer temperature and dry hydrogen concentration in reformer product gas as a function of CaO conversion for pre-heating values, $T_{0,ref}$, of 250°C (solid line) and 500°C (dashed line) (S/C=4 and λ=0.9).

dolomite also contributes to increased energy demand in the calciner compared to the case where the sorbent is pure limestone. The reformer efficiency also depends strongly on the temperature difference between the reformer and calciner. A high reformer temperature reduces the energy needed to heat the solids up to the calcination temperature. However, the reformer temperature has an upper limit as shown in Figures 5.9, because CO_2 capture decreases as its equilibrium shifts towards calcination with increasing reformer temperature.

The overall system performance for a pre-heat temperature of 250°C, S/C-ratio of 4 and λ=0.90 is presented in Table 5.4. It can be seen that increasing the solids circulation

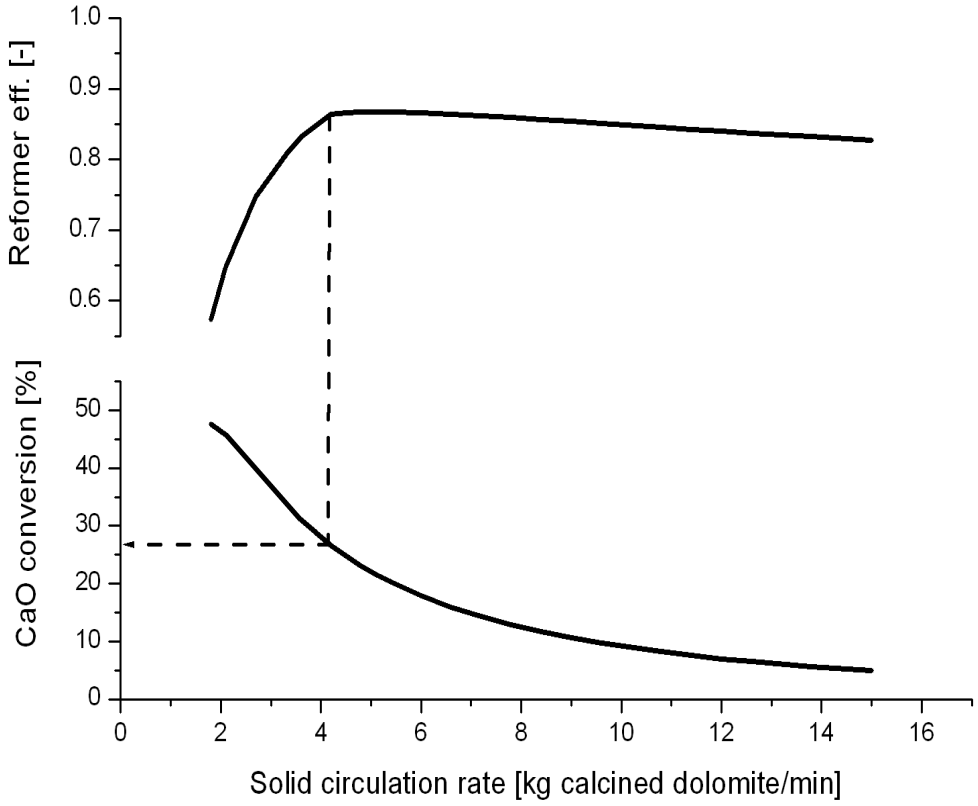

Figure 5.11: Reformer efficiency and solid conversion as function of circulation rate for S/C=4, λ=0.9 and $T_{0,ref}$=250°C.

rate causes the sorbent conversion (X_{CaO}) to decrease due to the shorter residence time in the reformer, whereas temperature (T_1) increases due to the increased flow of hot solids from the regenerator. The regenerator temperature (T_2) always equals the thermodynamic equilibrium decomposition temperature of $CaCO_3$ at the given partial pressure, with 50°C added to this temperature to assure complete calcination, and therefore slightly decreases as the degree of carbonation is reduced, so that less CO_2 is being released. The temperature difference between the reformer and calciner is critical for high system efficiencies. A higher temperature of the solids leaving the reformer means that less energy is needed for the calciner, hence increasing the efficiency. In addition, a lower CaO conversion means that less CO_2 is released in the calciner, reducing its partial pressure and decreasing the carbonate decomposition temperature.

Clearly there is a trade-off in choosing the reaction conditions if both high energy-efficiencies and high-purity of H_2 are sought. This is a major motivation for exploring other sorbents, which could release CO_2 at lower temperatures. The carbon capture efficiency is plotted as function of reformer temperature in Figure 5.12.

Table 5.4: Process parameters for S/C=4, λ=0.9 and $T_{0,ref}$=250°C

Solid circulation rate, $F_{s,2}$ [kg calcined dolomite/min]	**2.7**	**3.6**	**5.1**	**8.4**
Solid make-up ratio [fresh sorbent/recycled sorbent][a]	0.11	0.03	-	-
T_1 [°C]	542	578	619	665
T_2 [°C]	887	881	874	869
X_{CaO}	0.40	0.31	0.22	0.12
X_{CH_4}	0.92	0.96	0.98	0.99
X_{CO_2}	0.90	0.94	0.92	0.82
H_2 dry concentration [%]	97.4	98.4	98.0	95.5
Y_{H_2}	3.65	3.84	3.89	3.86
$H_{2,calciner}$	1.60	1.47	1.39	1.42
$H_{2,steam}$	0.70	0.66	0.65	0.68
$H_{2,caompression}$	0.27	0.27	0.27	0.26
$H_{2,eq}$	2.48	2.76	2.88	2.84
η_r [%]	74.7	83.1	86.7	85.6

[a] Based on calcined dolomite

The capture efficiency also depends to some extent on the sorbent conversion, as well as on temperature, and for a gas feed pre-heat temperature of 250°C the sorbent conversion ranges from 5-50% in the reformer temperature interval shown in Figure 5.12. Note that >90% of the carbon entering the reformer (assuming no carbon deposition on the catalyst) can be captured for reforming temperatures in the range of 540-630°C.

5.3.3 Heat supply to calciner

As previously mentioned, the heat of calcination can either be supplied by direct burning of fuel in the vessel or by the insertion of heat transfer tubes. There are two requirements that have to be fulfilled when determining the size of the calciner and the insertion of heat transfer tubes; the heat transfer area should be sufficiently large to supply the heat for the endothermic reaction, and the other is that the residence time of solids is high

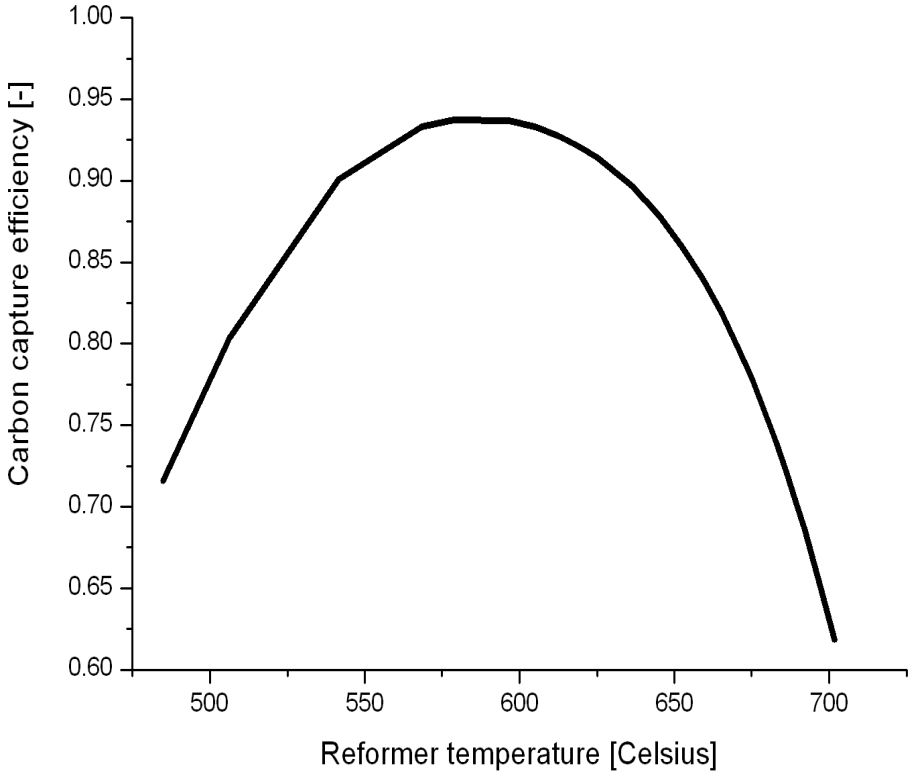

Figure 5.12: Carbon capture efficiency (X_{CO_2}) as function of reformer temperature for S/C=4, λ=0.9 and $T_{0,ref}$=250°C.

enough to ensure full conversion of the carbonate. The required heat transfer area can be estimated by assuming that the heat supply is the rate-limiting step for calcination.

The heat demand of calcination is represented by $H_{2,calciner}$ in Table 5.4, where a value of ∼1.4 mole H_2/mole CH_4 is representative for the heat demand of the calciner without any sorbent make-up addition. Multiplying with the molar feed rate of methane of 0.219 mole/s, and the lower heating value of hydrogen, the heat demand (Q) is found to be 74.2 kW. The heat transfer coefficient between the particle/gas medium and the submerged tube surfaces, h_w (kW//(m^2·K)), can be described by:

$$h_w = \frac{Q}{a_w \cdot (T_w - T_2)} \tag{5.24}$$

where a_w (m^2) is the submerged surface area, T_w is the temperature of the submerged surface, T_2 is the temperature of the bed and Q (kW) is the required heat for the calcination reaction.

The mechanisms of heat transfer are significantly different for different fluidization regimes [90]. Due to its engineering importance, the bed-to-surface heat transfer coefficient has been measured by many investigators for various geometries and operating conditions. Here, the heat transfer coefficient is estimated by using Vreedenberg's [91] correlation for horizontal tubes:

$$\frac{h_w \cdot D_t}{k_t} = 0.66 \cdot Pr_g^{0.3} \cdot \left(\frac{\rho_s \cdot (1-\epsilon)}{\rho_g \cdot \epsilon}\right)^{0.44} \cdot Re_D^{0.44} \qquad \text{for} \quad \frac{\rho_s}{\rho_g} \cdot Re_p \leq 2050 \tag{5.25}$$

where $Re_D = \frac{D_t \cdot \rho_g \cdot U}{\mu_g}$, $Re_p = \frac{d_p \cdot \rho_g \cdot U}{\mu_g}$, $Pr_g = \frac{C_{p,g} \cdot \mu_g}{k_t}$. Key properties for a gas mixture of steam and CO_2 at 870°C, obtained from the software Ergun (Ergun 6.0, Divergent S.A.), are listed in Table 5.5.

Table 5.5: Parameters used for calculating the heat transfer coefficient, obtained from Ergun (Ergun 6.0, Divergent S.A.) for a 50% H_2O/CO_2 mixture at 870°C

$C_{p,g}$ [J/kg K]	d_p [μm]	D_t [m]	k_t [W/m K]	U [m/s]	ρ_g [kg/m^3]	ρ_s [kg/m^3]	μ_g [Pa · s]
1795	200	0.05	0.0961	0.05	0.3887	2200	$4.39 \cdot 10^{-5}$

Inserting into Eq.(5.25):

$$\frac{h_w \cdot D_t}{k_t} = 0.66 \cdot 0.82^{0.3} \cdot \left(\frac{2200 \cdot (1-0.5)}{0.3887 \cdot 0.5}\right)^{0.44} \cdot 22.14^{0.44} = 108.84 \tag{5.26}$$

$$h_w = 108.84 \cdot \frac{0.0961}{0.05} = 0.209 \frac{kW}{m^2 \cdot K} \tag{5.27}$$

Radiative heat transfer needs to be taken into account at the high temperatures employed in the calciner. Ozkaynak et al. [92] found that the radiant contribution to heat transfer increased with temperature, and at 800°C the contribution was greater than 35% of the total heat flux in a bubbling bed. One way of calculating the radiative heat transfer coefficient, h_r, is to use the Stefan-Boltzman equation for radiant exchange

between opaque gray bodies [90], where it can be shown that:

$$h_r = (\frac{\epsilon_b \cdot \epsilon_w}{\epsilon_w + \epsilon_b - \epsilon_w \cdot \epsilon_b}) \cdot \frac{\sigma \cdot (T_2^4 - T_w^4)}{T_2 - T_w} \tag{5.28}$$

where σ is the Stefan-Boltzman constant ($5.67 \cdot 10^{-8}$ W/(m^2 K^4)), ϵ_w and ϵ_b are the emissivities of the wall and the bed respectively. For a bubbling bed it can be assumed that ϵ_b has the value of 0.9, while ϵ_w equals 0.66 for a SS316 material [90]. The required heat transfer area can be calculated by defining h=h$_w$+h$_r$, and rearranging Eq.(5.24):

$$a_w = \frac{Q}{h \cdot (T_w - T_2)} \tag{5.29}$$

Table 5.6 shows the calculated heat transfer area for various temperatures of the submerged surface, using T$_2$=870°C and Q=74.2 kW.

Table 5.6: Heat transfer area required in the calciner for different ΔT (T$_2$=870°C and Q=74.2 kW)

T$_w$ [°C]	**ΔT [°C]**	**h [kW/(m^2 K)]**	**a$_w$ [m^2]**
900	30	0.425	5.82
920	50	0.431	3.44
950	80	0.440	2.10

There are several ways the heat tubes can be arranged in the calciner. For simplicity, a rectangular box with horizontal tubes with a outer tube diameter of 0.05 m is assumed. With this geometry, seven tubes with a length of approximately 0.71 m can be placed in the cross section area of the reactor, and the distance between the tubes, the tube pitch, will be 0.06 m. Figure 5.13 shows the arrangement of the heat exchanger tubes. The surface area of a single heating tube is calculated to be:

$$A_t = 2 \cdot \pi \cdot \frac{0.05}{2} \cdot 0.71 = 0.11 \text{ m}^2 \tag{5.30}$$

The total number of heat exchanger tubes can now be calculated, based on the required heat transfer area in Table 5.6. The number of tubes was found to be 53, 32 and 20 for surface temperatures of 900, 920 and 950°C, respectively. The height of the bed (Z$_H$ in Figure 5.13) can be calculated by assuming that the distance between each

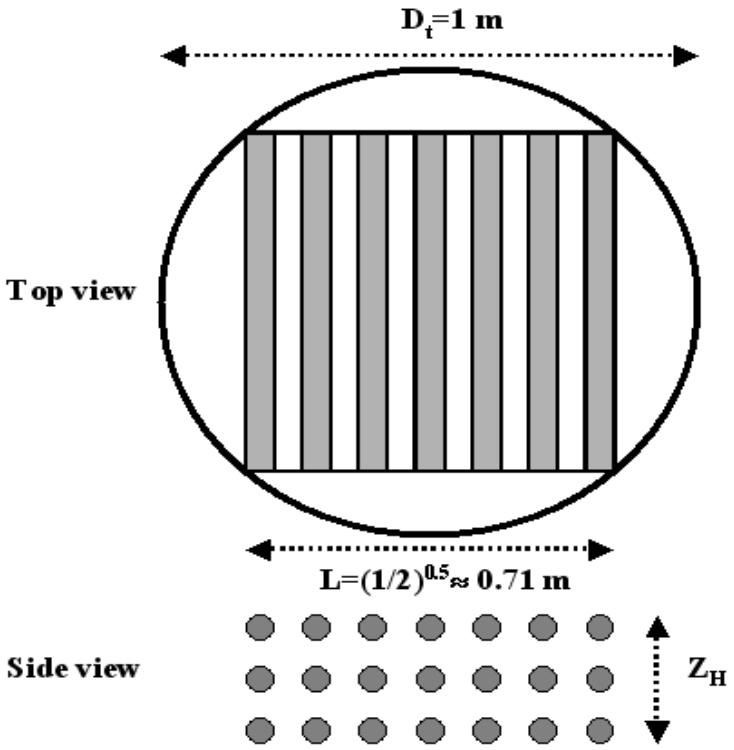

Figure 5.13: Arrangement of heat transfer tubes in calciner.

horizontal assembly of heating tubes is equal to the tube pitch of 0.06 m. Hence, 20 tubes correspond to a height of 0.27 m, whereas 53 tubes give a bed height of 0.82 m. These values are by no means unrealistic for a calciner of diameter 1 m, operated in the bubbling fluidization regime. However, surface temperatures of >900°C will require expensive high-temperature alloys to be used.

Design of high-temperature heat exchangers represent a major challenge for the process. Based on the above estimations, it is evident that high surface temperatures of the submerged heating tubes are required for obtaining reasonable values for the heating area. Indirect heat transfer is probably more likely to be applied for synthetic sorbents that are regenerated at lower temperatures.

5.3.4 Fresh sorbent addition

Abanades [82] incorporated a fresh sorbent make-up feed for CO_2 capture from combustion flue gases when evaluating carbon capture efficiency and claimed that there would be a compromise between moderate recycling rates and low addition of fresh sorbent to achieve high capture efficiencies. From Figure 5.11 it is clear that adding fresh sorbent reduces the efficiency of the system. Initial calcination of the fresh dolomite requires that $MgCO_3$ decomposes, partially nullifying the favorable multi-cycle properties of dolomites compared to limestone. Addition of fresh sorbent is only required for lower circulation rates to give steady-state CaO conversions above 28%. However, the model suggests that circulation rates can be relatively high while maintaining high-purity hydrogen and reformer efficiency. Note that the 28% conversion limit in the current model is based on a limited number of TG-cycles , and that a larger number of cycles is likely to give a lower conversion limit, which would require increased addition of fresh sorbent to the calciner, reducing the energy efficiency. For example, if the conversion limit (b) were to be reduced from 28% to 10%, and the circulation rate of sorbent remained constant at 6 kg/min, the reformer efficiency would be reduced from 86.6% to 72.1%.

Separation of catalyst from sorbent between the reactors should be avoided as this would add extra components and complexity to the system, lead to additional attrition and cause extra heat losses. Efficient separation of catalyst from the sorbent purge is likely to be difficult, meaning that addition of fresh sorbent should be minimized to reduce the loss of expensive catalyst from the purge stream. Ideally, the lifetime of the sorbent should be close to the expected catalyst lifetime - months or even years.

5.3.5 Increased gas velocity

A superficial gas velocity of 0.1 m/s is low for an industrial application. The effect of increased gas throughput was investigated, assuming a pseudo-steady-state conversion of sorbent of 20%, S/C=4, λ=0.9 and T_1=600°C, and the results are shown in Figure 5.14.

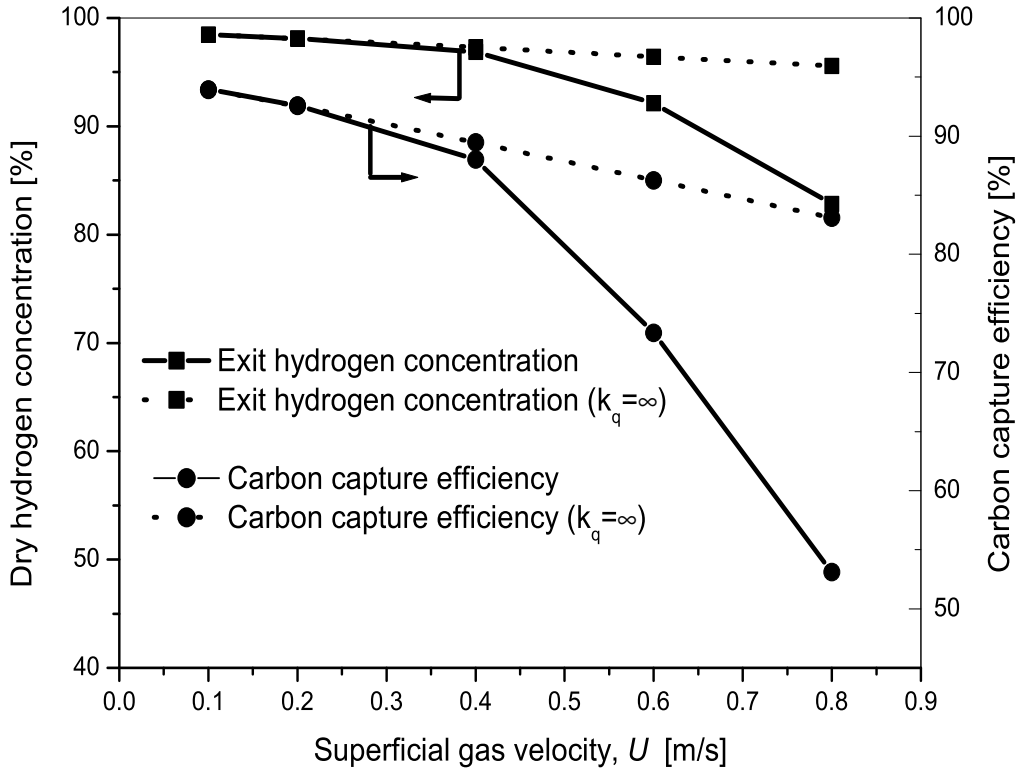

Figure 5.14: Effect of increased superficial gas velocity (S/C=4, λ=0.9, X_{CaO}=0.2 and T_1=600°C).

The exit hydrogen concentration is >95% for velocities up to ~0.5 m/s, after which there is a marked drop in hydrogen concentration and carbon capture efficiency. For U=0.8 m/s a hydrogen concentration of 82.2% is found at the reactor exit. In order to check if the reduced hydrogen concentration was caused by kinetic or interfacial mass transfer limitations, the mass transfer coefficient, k_q, was set to a infinite value and the

exit concentration was recalculated.

It is evident, from Figure 5.14, that the reduced hydrogen concentration is mainly caused by interphase mass transfer limitations rather than kinetics in the investigated range of velocities. The mass transfer coefficient, k_q, in Eq.(5.1), contains the sum of two terms. The first term is a throughflow component (convective flow) and the second term describes diffusion according to the penetration theory [61]. The convective term is mainly influenced by the particle size, as minimum fluidization velocity, U_{mf}, is increased with the particle diameter. Also, as the gas velocity is increased, the diameter of the bubbles in the bed, d_{eq}, increases in accordance with the findings of Mori and Wen [83], presented in Table 5.1. This effect is shown in Figure 5.14, where gas velocities exceeding ∼0.5 m/s will lead to significant by-pass of gas in the larger bubbles, reducing the exit hydrogen concentration. Note that the interphase mass transfer coefficient employed in the model is based on isolated bubbles. However, bubbles are likely to undergo interaction and coalescence as the gas velocity is increased and other mass transfer relationships might be more suited.

The rate of carbonation is also reduced as the residence time of the gas in the bed is reduced. The reforming reactions were found to be sufficiently fast, by setting λ=0, to reach equilibrium at all investigated velocities. The insertion of baffles in the bed is likely to reduce the bubble size and enhance the mass transfer between the bubbles and the dense phase.

5.3.6 Effect of pressure

The SE-SMR reactions are thermodynamically favored at low pressures, as shown in Figure 2.4. However, operating at pressurized conditions has the advantage of reducing the size of the reactors, and also reducing the energy requirements of compression of the product gases. If pressurized conditions are to be employed in the process, both reactors must be operated at essentially the same pressure in order to be able to transfer solids without adding a compressor.

Model predictions of hydrogen concentration as a function of temperature for pressures in the range of 1-20 atm, presented in Figure 5.15, are consistent with the thermodynamic calculations in Figure 2.4. The maximum hydrogen concentration is obtained at a higher reforming temperature as the pressure is increased. Increased total pressure will allow more gas to be fed to the reformer at a fixed superficial gas velocity, which

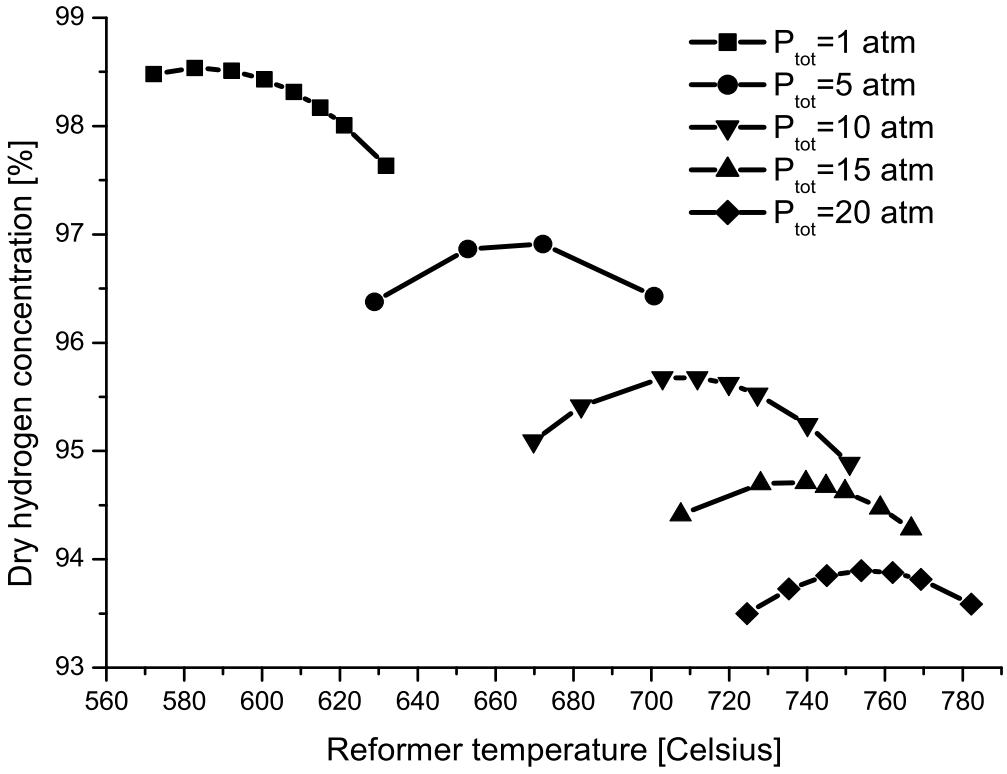

Figure 5.15: Exit hydrogen concentration as function of temperature for different pressures (S/C=4, λ=0.9 and $T_{0,ref}$=250°C).

again will require a higher circulation rate of sorbent. Circulation rates were adjusted so that the reformer temperature for obtaining maximum hydrogen concentration was reached, and a comparison of system performance at atmospheric pressure and at 20 atm is made in Table 5.7.

The volumetric feed rate of the gas is adjusted so that the superficial gas velocity corresponds to ∼0.1 m/s. Operating at 20 atm eliminates the need to compress the hydrogen product from the reformer. However, energy is still required to further compress the carbon dioxide from the calciner up to a pressure suited for transportation, i.e. 100 bar. From Table 5.7 it can be seen that the reformer efficiency is lower for the pressurized case. In fact, the reformer efficiency of 79.3% at 20 atm should be even lower if compression of the feed gas is taken into account. The lower efficiency is caused

Table 5.7: Pressure effect on system performance (S/C=4, λ=0.9 and $T_{0,ref}$=250°C)

Pressure	**1 atm**	**20 atm**
Volumetric feed rate [Nm^3/min]	1.47	29.4
Solid circulation rate, $F_{s,2}$ [kg calcined dolomite/min]	4.5	108
T_1 [°C]	601	754
T_2 [°C]	864	1076
X_{CaO}	0.25	0.17
X_{CH_4}	0.97	0.85
X_{CO_2}	0.94	0.78
H_2 dry concentration [%]	98.4	93.9
Y_{H_2}	3.88	3.37
$H_{2,calciner}$	1.43	1.60
$H_{2,steam}$	0.69	0.91
$H_{2,compression}$	0.27	0.05[a]
$H_{2,eq}$	2.87	2.63
η_r [%]	86.5	79.3

[a] Compression of feed gas is not included

by lower hydrogen yield and the very high regeneration temperature (1076°C) required. Operating the calciner at high pressure will increase the decomposition temperature of the carbonate, T_2, increasing the heat requirement for calcination, $H_{2,calciner}$, and also call for more expensive construction materials to be used. The very high regeneration temperature is also likely to cause severe sintering of the particles in the system. From this is it understood that the SE-SMR process should be run at low pressure.

5.4 Circulating fluidized bed

A circulating fluidized bed (CFB) for sorption-enhanced steam methane reforming has been modeled in order to get rough estimates of reactor dimensions and operating conditions. Reaction rate expressions as used in section 5.2 were adopted with a simple hydrodynamic model, assuming both gas and solids to be in plug flow [66]. More advanced models are available, e.g. the core-annulus model, but for getting rough estimates of e.g. the required reactor height for obtaining desirable hydrogen yield, the simple 1-D model was chosen. Only the reformer of the CFB system, shown in Figure 5.16 is considered.

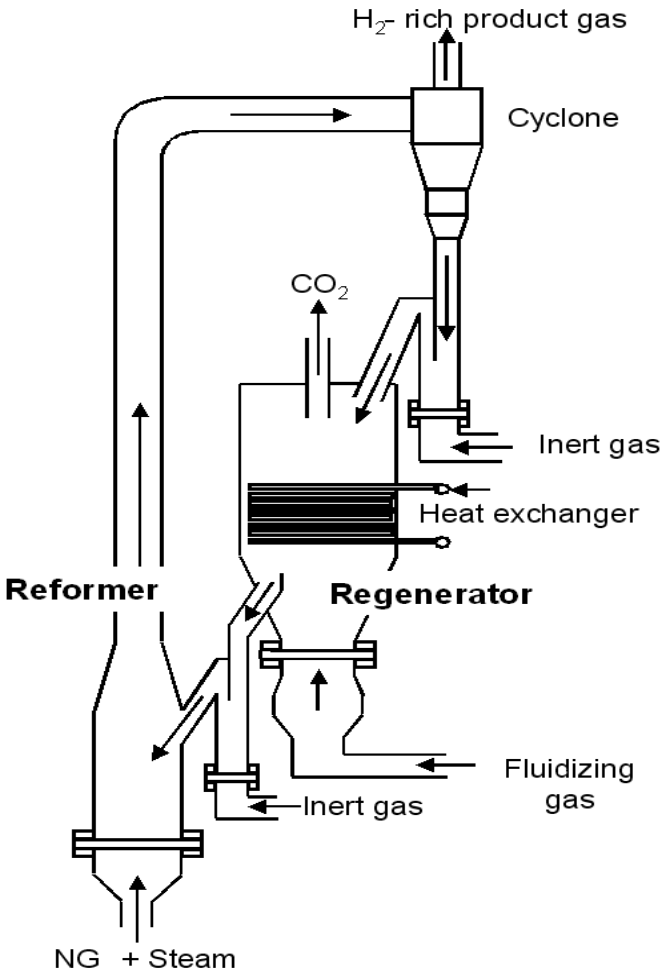

Figure 5.16: Simplified drawing of the CFB reactor concept.

5.4.1 Riser model

The following simplifying assumptions are made to the model of the riser:

i) Steady-state.

ii) Gas, catalyst and sorbent (calcined Arctic dolomite) are flowing in plug flow through the reformer, which is a cylindrical riser reactor.

iii) Negligible axial gas mixing and complete radial mixing.

iv) Constant volume fraction of solids along the height of the riser.

v) Isothermal operation at 600°C.

Design equations:

$$\frac{dF_i}{dz} = (1-\lambda)\cdot(1-\epsilon)\cdot A_c \cdot \rho_{cat} \cdot r_i \cdot \frac{1000}{3600} \tag{5.31}$$

for i=CH_4, CO, H_2, H_2O

$$\frac{dF_i}{dz} = (1-\lambda)\cdot(1-\epsilon)\cdot A_c \cdot \rho_{cat} \cdot r_i \cdot \frac{1000}{3600} - \lambda\cdot(1-\epsilon)\cdot A_c \cdot r_i^{'} \tag{5.32}$$

for i=CO_2

$$\frac{dF_i}{dz} = \lambda\cdot(1-\epsilon)\cdot r_i^{'} \tag{5.33}$$

for i=CaO, CaCO

where F_i (mole/s) is the molar flow of specie i, ϵ is the voidage in the riser and A_c is the cross sectional area of the riser (m^2). The reaction rates are as previously defined by Eq.(5.12), and λ is the volumetric ratio of sorbent to the total volume of solids calculated from:

$$\lambda = \frac{\gamma\cdot\psi\cdot\rho_{cat}}{\gamma\cdot\psi\cdot\rho_{cat} + \rho_{dolo}} \tag{5.34}$$

where γ is the feed mass ratio of sorbent to catalyst and ψ is the slip-factor (ratio between the particles and actual gas velocity). The slip-factor is calculated from a correlation proposed by Patience et al. [93] based on the Froude number:

$$\psi = \frac{U}{V_p \cdot \epsilon} = 1 + \frac{5.6}{Fr} + 0.47 \cdot Fr_t^{0.41} \tag{5.35}$$

where the Froude number is $Fr = \frac{U}{(g \cdot d_t)^{0.5}}$. For calculating the Froude number, Fr_t, the terminal particle velocity, U_t, is required, and the following relationship is used:

$$U_t = [0.072 \cdot g \cdot \frac{d_p^{(8/5)} \cdot (\rho_s - \rho_g)}{\rho_g^{(2/5)} \cdot \mu^{(3/5)}}]^{(5/7)} \tag{5.36}$$

The solid fraction, (1-ϵ), in the reformer is an important parameter for modeling of CFB risers, and numerous empirical correlations are available [94]. Investigations in the literature have demonstrated that the axial variation of the cross sectional average hold-up is dependent on many factors, such as operating conditions, solid properties, solid inventory, as well as geometry and system design configurations. At low solid rate, the solids move co-currently upwards with the gas and a uniform axial distribution is observed. By increasing the solid flow rate, a dense region at the bottom of the riser is observed with a dilute upper region. Without any experimental data on sorption-enhanced steam reforming in CFB reactors, empirical correlations are not available for the process. Therefore, for the purpose of preliminary estimates, the voidage correlation adopted by Pugsley and Berruti [95] was used:

$$\epsilon = \frac{U \cdot \rho_s}{U \cdot \rho_s + G_s \cdot \psi} \tag{5.37}$$

where G_s is the total solid flux (kg/(m^2 ·s)).

The molar flow rates of CaO and $CaCO_3$ can be rewritten, by using molar concentration [66]:

$$F_i = \lambda \cdot (1 - \epsilon) \cdot A_c \cdot V_p \cdot C_i \tag{5.38}$$

for i=CaO, CaCO

Inserting into Eq.(5.33):

$$\frac{dC_i}{dz} = \frac{r_i^{'}}{V_p} \tag{5.39}$$

where C_{CaO}=ρ_{CaO} at z=0

The particle velocity, V_p, found from the slip-factor, decreases as the particle size

increases, hence increasing the residence time. The base case conditions are listed in Table 5.8.

Table 5.8: Base case conditions for riser

Parameter	Value
Methane flow rate (Nm^3/h)	7.0 [a]
Steam-to-carbon molar feed ratio	4
Riser diameter (m)	0.1
Riser temperature (°C)	600
Superficial gas velocity (m/s)	~4[b]
Particle size[c](μm)	150
Height of riser (m)	6
Feed ratio, γ (kg dolomite/kg catalyst)	2

[a] Corresponding to ~80 kW LHV(H_2)-based for a hydrogen yield of 3.7 moles H_2/mole CH_4
[b] For feed gas entering at 600°C
[c] For both the dolomite and the catalyst

5.4.2 Results and discussion

The effect of increased circulation rate on hydrogen concentration in product gas was investigated, and the results are presented in Table 5.9.

Table 5.9: Reactor performance at proposed operation conditions

	Scenario 1	Scenario 2	Scenario 3
Solid circulation rate [kg/h] [a]	1922	2880	3837
Solid flux [kg/(m^2 ·s)]	68	102	136
λ [m^3 dolomite/m^3 total solids]	0.882	0.883	0.884
X_{CaO} [-]	0.0050	0.0045	0.0039
Voidage, ϵ [m^3 gas/m^3 reactor]	0.9795	0.9686	0.9579
Methane conversion, X_{CH_4} [%]	88.3	90.4	92.4
Exit dry H_2-concentration [%]	87.3	91.5	94.4

[a] Catalyst+dolomite

A very high circulation rate is needed in order to achieve hydrogen concentrations >90% at a reactor height of 6 meters. The rates calculated are comparable to other experimental studies in typical riser configurations listed by Bai and Kato [94], and the mass fluxes calculated in Table 5.9 are by no means unrealistic for CFBs. The very

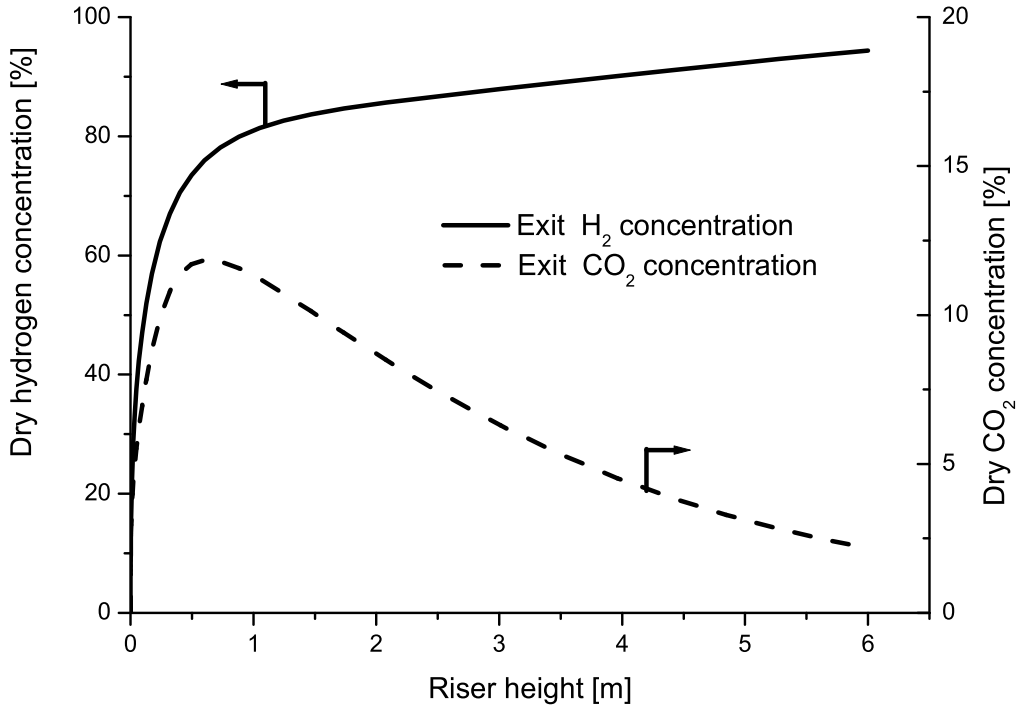

Figure 5.17: Exit hydrogen and carbon dioxide concentrations in riser for Scenario 3 (S/C=4, T=600°C and U=4 m/s).

high gas velocities in the riser are associated with large solid circulation rates. Increased solid flow increases the solid fraction, also referred to as solid hold-up, and according to Eqs.(5.31-5.33), the reaction rates will increase. It is therefore understood that the solid fraction in the riser is a key parameter in the model, and the uniform distribution of solids assumed should be regarded as a rough estimate. The solid hold-up is very dependent on solid properties as well as reactor configuration. For example, the exit shape of the riser will affect the pressure drop over the riser, again affecting the axial dispersion of solids in the riser. It is worth noticing the very low fractional conversion of

CaO at the exit of the riser (∼0.4%). Prasad and Elnashaie [66] also report a very low degree of CaO conversion in their CFB model, and found that increasing the slip-factor by increasing the particle size gave higher conversions. However, increasing the particle size of solids was not found to have the same advantageous effect in this study, due to slower reaction rate for larger dolomites particles, caused by diffusional limitations in the increased product layer of dolomite.

Figure 5.17 shows the concentration profiles of hydrogen and carbon dioxide for Scenario 3, where a final exit concentration of 94.4% hydrogen is reached. By allowing for a reactor height of 10 meters, the equilibrium concentration of ∼98% is approached. The very high riser required relates to the rather slow rate of carbonation. CO_2 will be consumed when the partial pressure is higher than the equilibrium partial pressure at the given temperature, and the onset of the net removal rate is observed approximately 1 m after the reactor inlet.

It should be emphasized that the very simple model adopted here only serves as a preliminary tool for analyzing the typical dimensions of a riser for the SE-SMR process. The assumptions of uniform solid distribution, discussed above, and uniform temperature are most likely not very realistic. In reality the solids entering the riser from the regenerator will probably have a temperature of ∼850°C, depending on the heat loss, and it will be important to control the temperature in order to operate at the optimum reaction temperature of ∼600°C. However, the model indicates CFB risers, with a height of 6-7 meters, to be a potential configuration with very high gas throughput and high hydrogen yield. Due to the uncertainties related to the hydrodynamics in the riser configuration, preliminary experimental studies of flow pattern in a cold flow reactor are needed.

Chapter 6

Conclusions and recommendations

6.1 Conclusions

The use of fluidized bed reactors for sorption-enhanced steam methane reforming has been investigated. The process has a continuous nature, as sorbent needs to be regenerated, and fluidized beds are considered an attractive reactor concept for this process. Arctic dolomite was chosen as the primary CO_2-acceptor in the study due to high absorption capacity, high reaction rate and low cost. The major findings of this work are summarized below:

- There is a lack of literature on the kinetics of carbonation of CaO, and due to different morphology of different calcium-based sorbents, rate equations for one sorbent cannot be applied for another. Conventional thermo gravimetric analysis, assuming constant temperature in the sample, was found unsatisfactory for obtaining kinetic parameters. Therefore, a non-isothermal approach using a novel thermo gravimetric reactor was applied, with a shrinking core model describing experimental data. An apparent activation energy of 32.6 kJ/mole was found from parameter fitting, which is in good agreement with previous reported results. The rate expression was able to predict experimental conversion up to ~30% very well, whereas the prediction of higher conversion levels was poorer. However, the residence time of sorbent in a continuous reformer-calciner system is likely to be rather low, so that only a fraction of the sorbent is utilized, highlighting the importance of the carbonation model at lower conversions. It is believed that the methodology for obtaining kinetic parameters used in this study, with

simultaneous recording of sample weight and temperature, could be applied to other gas-solid reactions as well.

- Hydrogen equilibrium concentrations were obtained in a bubbling fluidized bed reactor, operated at 600°C and 1 atm, for gas velocities investigated in the range of 0.032-0.096 m/s. Multiple reforming-regeneration cycles showed that the hydrogen concentration remained at 98-99 mole% after four cycles. The total production time was reduced with an increasing number of cycles due to loss of CO_2-uptake capacity of the dolomite, but the reaction rates of steam reforming and carbonation seemed to be unaffected for the conditions investigated. The very uniform temperature within the bed, with maximum axial differences in temperature of only 3-4°C, confirmed the good temperature control offered by bubbling fluidized beds. The degree of attrition of particles was found to be low in the bubbling bed, with 1.5% of the particles having a diameter of <90 μm for the highest velocity run of ∼0.1 m/s. At the given reaction conditions the overall reaction rate was sufficiently fast so that equilibrium was approached, making bubbling bed reactors an appealing choice for this process.

- Although the experimental results were obtained from a sequence of batch reforming-batch regeneration, it is believed that comparison can be made to coupling of two bubbling fluidized beds, which was investigated by modeling. Dry hydrogen concentrations of >98% can be achieved for temperatures of ∼600°C and a superficial gas velocity of 0.1 m/s using a simple two-phase bubbling bed model for the reformer, coupled with steam methane reforming and water gas shift reaction kinetics from the literature and experimentally-determined carbonation kinetics for Arctic dolomite. The model delineates important features of the system. Sorbent properties such as reactivity, multi-cycle capacity and reformer temperature determine the overall process performance. The catalytic reactions were found to be faster than the gas-solid carbonation reaction. A mixture containing 10% catalyst is predicted to obtain maximum hydrogen yield for the reactor conditions investigated. The reformer temperature should not be less than 540°C nor greater than 630°C to achieve carbon capture efficiencies >90%. The effect on carbonation for higher superficial gas velocities was investigated, and reduced hydrogen concentrations for U>0.5 m/s were found, mainly caused by interphase mass transfer limitations and by-pass of gas in bubbles. The multi-cycle capacity

of natural sorbents such as dolomites is rather poor, so that fresh sorbent needs to be added to the system to reduce the recycle flow. Operating at relatively high circulation rate is calculated to give the highest system efficiencies, because the reaction rate of natural sorbents is slow at high conversions compared to the initial carbonation stage, while addition of fresh dolomite requires energy to decompose both $CaCO_3$ and $MgCO_3$.

- A multi-cycle conversion limit of ∼30% was assumed in the model, which was based on experimental findings from TGA. This limit is, however, based on a limited number of cycles and the reformer efficiency was found very sensitive to this value. Synthetic sorbents that maintain their capacity upon multiple reforming-calcination cycles were also investigated. A low-temperature liquid phase co-precipitation method was used for synthesis of both Li_2ZrO_3 and Na_2ZrO_3. Li_2ZrO_3 showed a superior multi-cycle capacity compared to dolomite, but the rate of reaction in a diluted CO_2 atmosphere was very slow. The synthesized Na_2ZrO_3 proved to have both fast carbonation kinetics and stable multi-cycle performance. However, regeneration in the presence of carbon dioxide was not easily accomplished.

- Based on the findings of this work, a dual bubbling fluidized bed reactor configuration is believed to be an attractive configuration for SE-SMR. Low gas throughput is the major disadvantage for this configuration, and operation in the fast fluidization regime (circulating fluidized bed) is most likely to be preferred on an industrial scale of the process. Preliminary model results, using a plug flow assumption, suggest that the riser height in such a configuration will be in the order of 6-10 meters for equilibrium concentrations of >95% to be approached.

6.2 Future work

Based on the aforementioned conclusions, several new aspects of the process, subject for further investigations, arise. Also, there are subjects encountered that have been considered outside the scope of this work that should receive further attention.

- Further work is required on the cycling capacity properties of dolomites and other sorbents, in particular with respect to the sorption capacity after many more cycles than investigated in the current study or found in literature, because of the importance of the conversion limit with respect to the practicality and optimization of the sorption-enhanced reforming process. The lifetime of the sorbent should be close to that of the catalyst, in order to reduce the loss of expensive catalyst in the purge stream, and the number of cycles should be several thousands rather than the hundred investigated here.

- The use of circulating fluidized beds should be investigated. As a first approach, a cold flow reactor model of the CFB unit should be investigated for checking flow and circulation patterns, which also will give valuable information on solid hold-up in the system. The turbulent regime should also be investigated as a possible flow regime.

- Important hydrodynamic properties, such as voidage and solid hold-up, should be used as input for modeling of the CFB-unit. The very simple model of the riser employed in this study, should be made more sophisticated, incorporating the regenerator and energy balances. The model results should be used as basis for designing a full-scale CFB hot unit.

- Mechanical strength of particles will be crucial in a high velocity riser reactor, and both sorbent and catalyst attrition should be studied in detail. Most commercial reforming catalysts are designed for fixed bed applications, and will most likely not be suited for CFB operation. This calls for a comprehensive screening of catalysts. Also, long term performance in alternating reforming-regeneration atmospheres should be investigated in order to evaluate the catalyst stability in reducing/oxidizing environments. The use of noble based catalysts such as Ru, Rh and Ir, which are likely to withstand the oxidative regeneration conditions better than nickel, should also be investigated.

- The development of synthetic sorbents should be further investigated, with focus on understanding the reaction mechanisms of carbonation and calcination in order to formulate materials with better sorption properties. Sodium zirconate, in particular, proved to be a very promising sorbent, and may be further improved by adding a mixture of Na/K carbonates to create an eutectic interphase to promote CO_2 diffusion out of the particle during calcination.

- Synthetic Ca-based sorbents could also be investigated. These sorbents, reported by Cabot Superior MicroPowders, have just recently received publicity due to very stable multi-cycle performance compared to natural limestones and dolomites. The cost of raw materials for producing artificial dolomites is considerably lower than for the zirconium-based sorbents.

- Furthermore, it is recommended that heat exchange to the regenerator is investigated. Indirect heating is required for pure CO_2 to be released from the regenerator, this calls for design of high-temperature heat exchangers.

Bibliography

[1] http://yosemite.epa.gov/oar/globalwarming.nsf/content/climate.html.

[2] Houghton, J.T., Ding, Y., Griggs, D.J., Noguer, M., van der Linden, P.J., Dai, X., Maskell, K. and Johnson, C.A. *IPCC 2001: Climate Change 2001: The Scientific Basis. Contribution of Working Group I to the Third Assessment Report of the Intergovernmental Panel on Climate Change*. Cambridge University Press, 2001.

[3] International Energy Agency, Committe on Energy Research and Technology, Working Party on Fossil Fuels. Solution for the 21st century - zero emissions technology for fossil fuels. Technical report, OECD/IEA, 2002.

[4] Davidson, J. and Thambimuthu, K. Technologies for capture of carbon dioxide. In *Proceedings of the 7th International Conference on Green House Gas Control Technologies (GHGT-7)*, Vancouver, Canada, 5th-9th September 2004.

[5] Metz, B., Davidson, O., de Connick, H., Loos, M. and Meyer, L. *IPCC 2005: Special Report on Carbon Dioxide Capture and Storage*. Cambridge University Press, 2005.

[6] Mimura, T., Satsumi, S., Iijama, M. and Mitsuoka, S. Development of energy saving technologies for flue gas carbon dioxide recovery by chemical adsorption method and stream system in power plants. In *Proceedings of the 4th International Conference of Green House Gas Control Technologies (GHGT-4)*, Interlaken, Switzerland, 30th August-2nd September 1998.

[7] Morimoto, S., Taki, K. and Maruyama, T. Current review of CO_2 separation and recovery technologies. International test network for CO_2 capture, 4th workshop, Kyoto, 2002.

[8] International Energy Agency. Prospects for CO_2 capture and storage. Technical report, OECD/IEA, 2004.

[9] Mattisson, T., Johansson, M. and Lyngfelt, A. The use of NiO as an oxygen carrier in chemical-looping combustion. *Fuel*, 85:736–747, 2006.

[10] Granite, E.J. and O'Brien, T. Review of novel methods for carbon dioxide separation from flue and fuel gases. *Fuel Processing Technology*, 86:1423–1434, 2005.

[11] Shimizu, T., Hirama, T., Hosoda, H., Kitano, K., Inagaki, M. and Tejima, K. A twin fluid-bed reactor for removal of CO_2 from combustion processes. *Trans IChemE*, 77:62–68, 1999.

[12] Abanades, J.C., Anthony, E.J., Lu, D.Y., Salvador, C. and Alvarez, D. Capture of CO_2 from combustion gases in a fluidized bed of CaO. *AIChE Journal*, 50:1614–1622, 2004.

[13] Abanades, J.C. and Alvarez, D. Conversion limits in the reaction of CO_2 with lime. *Energy & Fuels*, 17:308–315, 2003.

[14] Muradov, N.Z. and Veziroglu, T.N. From hydrocarbon to hydrogen-carbon to hydrogen economy. *International Journal of Hydrogen Energy*, 30:225–237, 2005.

[15] Sherif, S.A., Barbir, F. and Veziroglu, T.N. Towards the hydrogen economy. *The Electricity Journal*, 18:62–76, 2005.

[16] Simbeck, D.R. CO_2 capture and storage - the essential bridge to the hydrogen economy. *Energy*, 29:1633–1641, 2004.

[17] Dicks, A.L. Hydrogen generation from natural gas for the fuel cell systems of tomorrow. *Journal of Power Sources*, 61:113–124, 1996.

[18] Pena, M.A., Gómez, J.P. and Fierro, K.L.G. New catalytic routes for syngas and hydrogen production. *Applied Catalysis A: General*, 144:7–57, 1996.

[19] Gaudernack, B. and Lynum, S. Hydrogen from natural gas without release of CO_2 to the atmosphere. *International Journal of Hydrogen Energy*, 23:1087–1093, 1998.

[20] López-Ortiz, A. *Enhanced sorption process for the production of hydrogen.* PhD thesis, Lousiana State University, 2000.

[21] Adris, A.M., Pruden, B.B., Lim, C.J. and Grace, J.R. On the reported attempts to radically improve the performance of the steam methane reforming reactor. *Canadian Journal of Chemical Engineering*, 74:177–186, 1996.

[22] Chen, Z., Yan, Y. and Elnashaie, S.S.E.H. Novel circulating fast fluidized-bed membrane reformer for efficient production of hydrogen from steam reforming of methane. *Chemical Engineering Science*, 58:4335–4349, 2003.

[23] Elnashaie, S. S. E. H. and Adris, A. M. A fluidized bed steam reformer for methane. In *Fluidization VI*, [Eds. Grace, J.R., Shemilt, L.W. and Bergougnou, M.A.], Engineering Foundation, New York, 319-326, 1989.

[24] Roy, S., Pruden, B.B., Adris, A.M., Grace, J.R and Lim, C.J. Fluidized bed steam methane reforming with oxygen input. *Chemical Engineering Science*, 54:2095–2102, 1999.

[25] Trimm, D.L. Coke formation and minimization during steam reforming reactions. *Catalysis Today*, 37(3):233–238, 1997.

[26] Nazarkina, E.G. and Kirichenkom, H.A. Improvement in the steam catalytic conversion of methane by hydrogen liberation via palladium membrane. *Khimiya Tekhnologiya Topliv Massel*, 3:5–7, 1979. English translation available on Chemistry and Technology of fuels and oils, Plenum Publishing Corporation, New York.

[27] Adris, A. M., Elnashaie, S.S.E.H. and Hughes, R. A fluidized bed membrane reactor for the steam reforming of methane. *Canadian Journal of Chemical Engineering*, 69:1061–1070, 1991.

[28] Adris, A.M. *A fluidized bed membrane reactor for steam reforming: experimental verification and model validation.* PhD thesis, University of British Columbia, 1994.

[29] Adris, A.M., Lim, C.J. and Grace, J.R. The fluidized bed membrane reactor for steam methane reforming: Model verification and parametric study. *Chemical Engineering Science*, 52:1609–1622, 1997.

[30] Adris, A.M., Grace, J.R., Lim, C.J. and Elnashaie, S.S.E.H. Fluidized bed reaction system for steam/hydrocarbon reforming to produce hydrogen. U.S. Patent No. 5,326,550, 1994.

[31] Rostrup-Nielsen, J.R. Catalytic steam reforming. In *Catalysis: Science and Technology*, [Eds: Anderson, J.R. and Boudart, M.], Springer, Berlin, 1-117 1984.

[32] Williams, R. Hydrogen production. U.S. Patent No. 1,938,202, 1933.

[33] Gorin, E. and Retallick, W.B. Method for production of hydrogen. U.S. Patent No. 3,108,87, 1963.

[34] Brun-Tsekhovoi, A.R., Zadorin, A.N., Katsobashvili, Y.R. and Kourdyumov, S.S. The process of catalytic steam reforming of hydrocarbons in the presence of carbon dioxide acceptor. In *Hydrogen Energy Progress VII, Proceedings of the World Hydrogen Energy Conference*, Pergamon Press, 885-900, 1988.

[35] Han, C. and Harrison, D.P. Simultaneous shift reaction and carbon dioxide separation for the direct production of hydrogen. *Chemical Engineering Science*, 49:5875–5883, 1994.

[36] Silaban, A. and Harrison, D.P. High temperature capture of carbon dioxide: Characteristics of the reversible reaction between CaO(s) and CO_2(g). *Chemical Engineering Communications*, 137:177–190, 1995.

[37] Silaban, A., Narcida, M. and Harrision, D.P. Characteristics of the reversible reaction between CO_2(g) and calcined dolomite. *Chemical Engineering Communications*, 146:149–162, 1996.

[38] Lopez Ortiz, A. and Harrison, D.P. Hydrogen production using sorption-enhanced reaction. *Industrial & Engineering Chemistry Research*, 40:5102–5109, 2001.

[39] Balasubramanian, B., Lopez Ortiz, A., Kaytakoglu, S. and Harrison, D.P. Hydrogen from methane in a single-step process. *Chemical Engineering Science*, 54:3543–3552, 1999.

[40] Yi, K.B. and Harrison, D.P. Low-pressure sorption-enhanced hydrogen production. *Industrial & Engineering Chemistry Research*, 44:1665–1669, 2005.

[41] Hufton, J. R., Mayorga, S. and Sircar, S. Sorption-enhanced reaction process for hydrogen production. *AIChE Journal*, 45(2):248–256, 1999.

[42] Baker, E.H. The calcium oxide-carbon dioxide system in the pressure range 1-300 atmospheres. *Journal of the Chemical Society*, 70:464–470, 1962.

[43] Ding, Y. and Alpay, E. Equilibria and kinetics of CO_2 adsorption on hydrotalcite adsorbent. *Chemical Engineering Science*, 55:3461–3474, 2000.

[44] Essaki, K. and Kato, M. Influence of temperature and CO_2 concentration on the CO_2 absorption properties of lithium silicate pellets. *Journal of Materials Science*, 40:5017–5019, 2005.

[45] Yi, K.B. and Eriksen, D. Low temperature liquid state synthesis of lithium zirconate and its characteristics as a CO_2 sorbent. *Separation Science and Technology*, 41:283–296, 2006.

[46] L*ó*pez-Ortiz, A., Perez Riviera, N.G., Reyes Rojas, A. and Lardizabal Gutierrez, D. Novel carbon dioxide solid acceptors using sodium containing oxides. *Separation Science and Technology*, 39:3559–3572, 2004.

[47] Dedman, A. J. and Owen, A. J. Calcium cyanide synthesis. part 4 - the reaction of CaO + CO_2 = $CaCO_3$. *Transactions of the Faraday Society.*, 58:2027 – 2035, 1962.

[48] Bhatia, S. K. and Perlmutter, D. D. Effect of the product layer on the kinetics of the CO_2-lime reaction. *AIChE Journal.*, 29:79–86, 1983.

[49] Bandi, T., Marquard-Moellenstedt, T., Sichler, P., Specht, M. and Axmann, P. Natural minerals for high temperature CO_2 capture. Poster presentation at 7th International Conference on Green House Gas Technologies, Vancouver, Canada, 5th-9th September 2004.

[50] Salvador, C., Lua, D., Anthony, E.J. and Abanades, J.C. Enhancement of CaO for CO_2 capture in an fbc environment. *Chemical Engineering Journal*, 96:187–195, 2003.

[51] Gullett, B.K. and Bruce, K.R. Pore distribution changes of calcium-based sorbents reaction with sulfur dioxide. *AIChE Journal*, 33(10):1719–1726, 1987.

[52] Kuramoto, K., Fujimoto, S., Morita, A., Shibano, S., Suzuki, Y., Hatano, H., Shi-Ying, L., Harada, M. and Takarada, T. Repetitive carbonation-calcination reactions of Ca-based sorbents for efficient CO_2 sorption at elevated temperatures and pressures. *Industrial & Engineering Chemistry Research*, 42:975–981, 2003.

[53] Reijers, H.T.J., Valster-Schiermeier, S.E.A., Cobden, P.D. and van der Brink, R.W. Hydrotalcite as CO_2 sorbent for sorption-enhanced steam reforming of methane. *Industrial & Engineering Chemistry Research*, 45:2522–2530, 2006.

[54] Nakagawa, K. and Ohashi, T. A reversible change between lithium zirconate and zirconia in molten carbonate. *Electrochemistry*, 67:618–621, 1999.

[55] Ida, J. and Lin, Y. Mechanism of high temperature CO_2 sorption on lithium zirconate. *Environmental Science Technology*, 37:1999–2004, 2003.

[56] Ochoa-Fernández, E., Rusten, H.K., Jakobsen, H.A., Rønning, M., Holmen, A. and Chen, D. Sorption enhanced hydrogen production by steam methane reforming using Li_2ZrO_3 as sorbent: Sorption kinetics and reactor simulation. *Catalysis Today*, 106:41–46, 2005.

[57] Kato, M. and Nakagawa, K. New series of lithium containing complex oxides, lithium silicates, for application as a high temperature CO_2 absorbent. *Journal of Ceramic Society of Japan*, 109(11):911–914, 2001.

[58] Kato, M., Yoshikawa, S. and Nakagawa, K. Carbon dioxide absorption by lithium orthosilicate in a wide range of temperatures and carbon dioxide concentrations. *Journal of Materials Science Letters*, 21:485–487, 2002.

[59] Abanades, J.C., Rubin, E.S. and Anthony, E.J. Sorbent cost and performance in CO_2 capture systems. *Industrial & Engineering Chemistry Research*, 43:3462–3466, 2004.

[60] http://www.hydrogen.energy.gov/pdfs/review05/fc44_stevens.pdf.

[61] Grace, J.R. Chapter 11: Fluid beds as chemical reactors. In *Fluidization Technology*, [Ed:Geldart, D.], Wiley, Chichester, 285-339 1986.

[62] Grace, J.R. Contacting modes and behaviour classification of gas-solid and other two-phase suspensions. *Canadian Journal of Chemical Engineering*, 64:353–363, 1986.

[63] Jiang, P., Wei, F. and Fan, L.S. Chapter 12: General approaches to reactor design. In *Handbook of Fluidization and Fluid-Particle Systems*, [Ed: Yang, W.C.], Marcel Dekker, Inc, New York, 309-342, 2004.

[64] Kunii, D. and Levenspiel, O. *Fluidization Engineering*. Butterworth-Heinemann, Newton, MA, 1991.

[65] Bi, H.T., Ellis, N., Abba, I.A. and Grace, J.R. A state-of-the-art review of gas-solid turbulent fluidization. *Chemical Engineering Science*, 55:4789–4825, 2000.

[66] Prasad, P. and Elnashaie, S.S.E.H. Novel circulating fluidized-bed membrane reformer using carbon dioxide sequestration. *Industrial & Engineering Chemistry Research*, 43:494–501, 2004.

[67] Bemrose, C.R. and Bridgwater, J. A review of attrition and attrition test methods. *Powder Technology*, 49:97–126, 1987.

[68] D 5757: Standard test method for determination of attrition and abrasion of powder catalysts by air jets. ASTM, US.

[69] Lee, D.K. An apparent kinetic model for the carbonation of calcium oxide by carbon dioxide. *Chemical Engineering Journal*, 100:71–77, 2004.

[70] Gupta, H. and Fan, L. Carbonation-calcination cycle using high reactivity calcium oxide for carbon dioxide separation from flue gas. *Industrial & Engineering Chemistry Research*, 41:4035–4042, 2002.

[71] Mess, D., Sarofim, A.F. and Longwell, J.P. Product layer diffusion of calcium oxide with carbon dioxide. *Energy & Fuels*, 13:999–1005, 1999.

[72] Kyaw, K., Kanamori, M., Matsuda, H. and Hansatani, M. Study of carbonation reaction of Ca-Mg oxides for high temperature energy storage and heat transformation. *Journal of Chemical Engineering of Japan*, 29(1):112–118, 1996.

[73] Levenspiel, O. *Chemical Reaction Engineering*. Wiley, New York, 1972.

[74] Zevenhoven, C.A.P., Yrjas, K.P. and Hipa, M.M. Hydrogen sulfide capture by limestone and dolomite at elevated pressure. 2. sorbent particle conversion modeling. *Industrial & Engineering Chemistry Research*, 35:943–949, 1996.

[75] Yi, Kwang Bok and Eriksen, Dag Øistein. Method for producing lithium zirconate. Norwegian patent application No.: 20053197, 2006.

[76] Constantineau, J.P. *Fluidized bed roasting of zinc sulfide concentrate: factors affecting the particle size distribution.* PhD thesis, University of British Columbia, 2004.

[77] Li, Y., Buchi, S., Grace, J.R. and Lim, C.J. SO_2 removal and CO_2 capture by limestone resulting from calcination/sulphation/carbonation cycles. *Energy & Fuels*, 19:1927–1934, 2005.

[78] Khotomlyanskii, L.N., Brun-Tsekhovoi, A.R., Katsobashvili, Y.R., Petrov, V.N. and Skoblo, A.I. Investigation of the separation of dissimilar particles in fluidized bed. *Chemistry and technology of fuels and oils*, 6:15–19, 1970.

[79] Rowe, P.N. and Nienow, A.W. Particle mixing and segregation in gas fluidized beds: a review. *Powder Technology*, 15:141–147, 1976.

[80] Ho, T.C. Chapter 9: Modeling. In *Handbook of Fluidization and Fluid-Particle Systems*, [Ed: Yang, W.C.], Marcel Dekker, Inc, New York, 239-255, 2004.

[81] Orcutt, J.C., Davidson, J.F. and Pigford, R.L. Reaction time distributions in fluidized catalytic reactors. *Chemical Engineering Progress Symposium Series*, 58(38):1–15, 1962.

[82] Abanades, J.C. The maximum capture efficiency of CO_2 using a carbonation/calcination cycle of $CaO/CaCO_3$. *Chemical Engineering Journal*, 90:303–306, 2002.

[83] Mori, S. and Wen, C.Y. Estimation of bubble diameter in gaseous fluidized beds. *AIChE Journal*, 21:109–115, 1975.

[84] Davidson, J.F. and Harrison, D. *Fluidized Particles.* Cambridge University Press, New York, 1963.

[85] Wen, C.Y. and Yu, Y.H. A generalized method for predicting the minimum fluidization velocity. *AIChE Journal*, 12:610–612, 1966.

[86] Goossens, W.R.A, Dumont, G.L. and Spaepen, G.L. Fluidization of binary mixtures in the laminar flow region. *Chemical Engineering Progress Symposium Series*, 67:38–45, 1971.

[87] Xu, J. and Froment, G.F. Methane steam reforming, methanation and water gas shift- I. intrinsic kinetics. *AIChE Journal*, 35:88–96, 1989.

[88] Rydén, M. and Lyngfelt, A. Hydrogen and power production with integrated CO_2 capture by chemical looping reforming. In *Proceedings of the 7th International Conference on Green House Gas Control Technologies*, Vancouver, Canada, 5th-9th September 2004.

[89] Grace, J.R. Generalized models for isothermal fluidized bed reactors. In *Recent Advances in Engineering Analysis of Chemical Reacting Systems*, [Ed: Doraiswamy, L.K.], Wiley, New Delhi, 1984.

[90] Chen, J.C. Chapter 10: Heat transfer. In *Handbook of Fluidization and Fluid-Particle Systems*, [Ed: Yang, W.C.], Marcel Dekker, Inc, New York, 257-286, 2004.

[91] Vreedenberg, H.A. Heat transfer between a fluidized bed and a horizontal tube. *Chemical Engineering Science*, 9:52–60, 1958.

[92] Ozkaynak, T.F., Chen, J.C. and Frankenfield, T.R. An experimental investigation of radiant heat transfer in a high temperature fluidized bed. In *Fluidization IV*, Engineering Foundation, New York, 371-378, 1983.

[93] Patience, G.S., Chaouki, J., Berruti, F. and Wong, R. Scaling considerations for circulating fluidized bed risers. *Powder Technology*, 72:31–37, 1992.

[94] Bai, D. and Kato, K. Quantitative estimation of solids holdups at dense and dilute regions of circulation beds. *Powder Technology*, 101:183–190, 1999.

[95] Pugsley, T.S. and Berruti, F. A predictive hydrodynamic model for circulating fluidized bed risers. *Powder Technology*, 89:57–69, 1996.

[96] Reid, R.L. and Sherwood, T.L. *The properties of gases and liquids*. McGraw-Hill, 1968.

[97] Lydersen, A.L. *Fluid Flow and Heat Transfer*. John Wiley and Sons, Chichester, 1979.

[98] Wilke, C. R. A viscosity equation for gas mixtures. *Journal of Chemical Physics*, 18:517–519, 1950.

Appendix A: Derivation of the shrinking core model

A.1 Shrinking unreacted core

For a spherical particle, a generalized mathematical model has been developed for the reaction:

$$A(g) + bB(s) \longleftrightarrow P(s) \tag{A.1}$$

where in this case A is CO_2, B is CaO, P is $CaCO_3$ and the stoichiometric coefficient b is equal to unity. The calcined dolomite particle contains inert MgO and the following derivation is made considering a calcined dolomite particle. Calcined dolomite is referred to as dolomite, for convenience. A schematic drawing of a shrinking unreacted core for dolomite is shown in Figure A.1

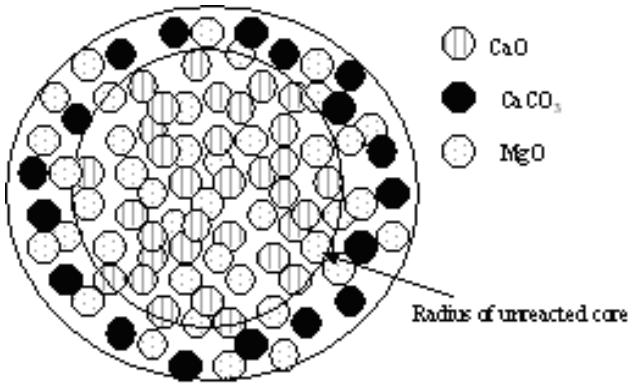

Figure A.1: Shrinking core of dolomite

The three resistances to reaction, described by Levenspiel [73], are treated separately.

External mass transfer

Whenever the resistance of the gas film controls, the driving force will be constant.

$$-\frac{1}{4 \cdot \pi \cdot R_p^2} \cdot \frac{dN_B}{dt} = b \cdot k_g \cdot (C_{Ag} - C_{As}) \tag{A.2}$$

where k_g is the external mass transfer coefficient (m^3 gas/m^2 external particle/s), C_{Ag} and C_{As} are gas concentrations in the bulk and at the particle surface (mole/m^3 gas), respectively, and R_p is the radius of the particle (m). The situation is illustrated in Figure A.2 .

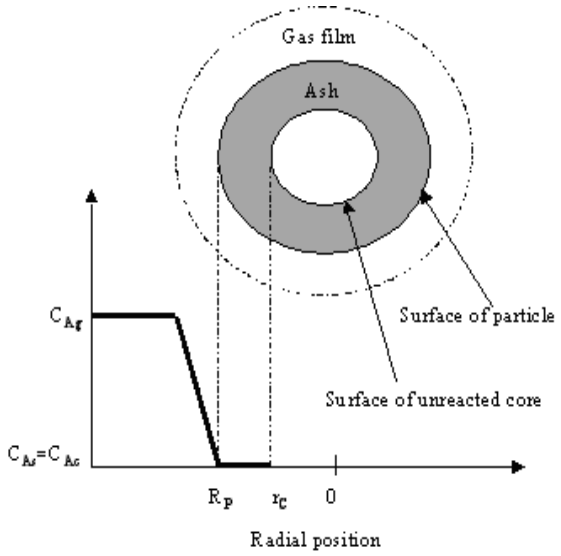

Figure A.2: Concentration of gas phase reactant versus radial position when gas film is the controlling resistance.

The decrease in volume or radius of unreacted core accompanying the disappearance of dN_B moles of solid is given by

$$-dN_B = -b \cdot dN_A = -\rho_B \cdot dV_{dolomite} = -\rho_B \cdot d(\frac{4}{3}\pi \cdot r_c^3) = -4\pi \cdot \rho_B \cdot r_c^2 dr_c \tag{A.3}$$

where r_c is the radius of the unreacted core (m) and ρ_B is the molar density (mole CaO/m^3 dolomite). Inserting this into Eq.(A.2), and expressed by the partial pressure

of reactant gas

$$-\frac{1}{4\cdot\pi\cdot R_p^2}\cdot\frac{dN_B}{dt}=-\frac{\rho_B\cdot r_c^2}{R_p^2}\cdot\frac{dr_c}{dt}=b{\cdot}k_g\cdot(C_{Ag}-C_{As})=\frac{b\cdot k_g}{R\cdot T}\cdot(P_{Ag}-P_{As}) \quad \text{(A.4)}$$

$$-\frac{dr_c}{dt}=\frac{R_p^2\cdot b\cdot k_g}{R\cdot T\cdot\rho_B\cdot r_c^2}\cdot(P_{Ag}-P_{As}) \quad \text{(A.5)}$$

Intra-particle diffusion control

An illustration of the situation when resistance to diffusion through the ash/product layer is rate controlling is shown in Figure A.3 .

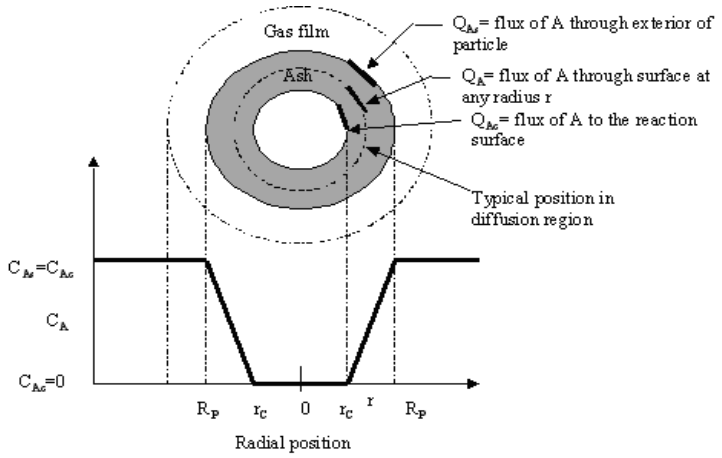

Figure A.3: Reacting particle when diffusion through the product layer is the controlling resistance

Both the reactant A and the boundary of unreacted core move inwards to the center of the particle. Shrinking of unreacted core is assumed to be much slower than the flow of A towards the unreacted core, and thus the unreacted core behaves as if it was stationary. The rate of reaction of A at any instant is given by its rate of diffusion to the reaction surface

$$-\frac{N_A}{dt}=4\pi\cdot r^2\cdot Q_A=4\pi\cdot {R_p}^2\cdot Q_{As}=4\pi\cdot {r_c}^2\cdot Q_{Ac}=\text{constant} \quad \text{(A.6)}$$

Flux of A within the product layer is expressed by Ficks's law for equimolar counter diffusion:

$$Q_A = D_e \cdot \frac{dC_A}{dr} \tag{A.7}$$

where D_e (m^3 A/m core /s) is the effective diffusivity of A. Combining Eq.(A.6) and Eq.(A.7) we obtain for any r

$$-\frac{N_A}{dt} = 4\pi \cdot r^2 \cdot \frac{dC_A}{dr} \tag{A.8}$$

Integrating from R_P to r_c

$$-\frac{N_A}{dt} \cdot \int_{R_p}^{r_c} \frac{1}{r^2} dr = 4\pi \cdot D_e \cdot \int_{C_{Ag}=C_{As}}^{C_{Ac}=0} dC_A \tag{A.9}$$

or

$$-\frac{N_A}{dt} \cdot (\frac{1}{r_c} - \frac{1}{R_p}) = 4\pi \cdot D_e \cdot (C_{As} - C_{Ac}) = \frac{4\pi \cdot D_e}{R \cdot T} \cdot (P_{As} - P_{Ac}) \tag{A.10}$$

Using the relationship given by Eq.(A.2), $-dN_B = -b \cdot dN_A$, and solving for r_c

$$-\frac{dr_c}{dt} = \frac{b \cdot D_e}{R \cdot T \cdot \rho_B \cdot r_c^2 \cdot (\frac{1}{r_c} - \frac{1}{R_p})} (P_{As} - P_{Ac}) \tag{A.11}$$

Chemical reaction control

The reaction between CO_2 and the CaO in the calcined dolomite is very temperature sensitive and the reverse calcination reaction must also be considered. The equilibrium constant of the reaction is defined as $K_E = \frac{k_f}{k_r} = \frac{1}{P_{Ae}}$

$$-\frac{1}{4\pi \cdot r_c^2} \cdot \frac{dN_B}{dt} = -\frac{b}{4\pi \cdot r_c^2} \cdot \frac{dN_A}{dt} = b \cdot (k_f \cdot C_{Ac} - k_r \cdot C_P) = k_f \cdot b \cdot (C_{Ac} - \frac{C_P}{K_E}) = \frac{k \cdot b}{R \cdot T} \cdot (P_{Ac} - P_{Ae}) \tag{A.12}$$

Since the progress of reaction is unaffected by the presence of any product layer, the rate is proportional to the available surface of the unreacted core. Inserting $-dN_B = -4\pi \cdot \rho_B \cdot r_c^2 \cdot dr_c$

$$-\frac{dr_c}{dt} = \frac{b \cdot k}{\rho_B \cdot R \cdot T} \cdot (P_{Ac} - P_{Ae}) \tag{A.13}$$

where k is a first-order rate constant for the surface reaction (m^3 gas/m^2 core dolomite/s), defined by $k = k_0 \cdot e^{\frac{E_a}{R \cdot T}}$

Combination of resistances

After deriving the individual resistances, we now combine Eq.(A.5), Eq.(A.11) and Eq.(A.13) and eliminate the intermediate partial pressures of P_{As} and P_{Ac}, to give an overall reaction rate equation

$$-\frac{dr_c}{dt} = \frac{\frac{b}{\rho_B \cdot R \cdot T} \cdot (P_{Ag} - P_{Ae})}{\frac{1}{k} + \frac{r_c \cdot (R_p - r_c)}{R_p \cdot D_e} + \frac{r_c^2}{R_p^2 \cdot k_g}} \tag{A.14}$$

It is desirable to express this rate in terms of conversion. For a spherical particle we have the following relationship between the radius of shrinking core, r_c, and the conversion:

$$X = 1 - (\frac{r_c}{R_p})^3 \tag{A.15}$$

The radius of the unreacted core is then given by

$$r_c = R_p \cdot (1 - X)^{(1/3)} \tag{A.16}$$

and

$$-dX = 3 \cdot (\frac{r_c}{R_p})^2 \cdot \frac{1}{R_p} \cdot dr_c \tag{A.17}$$

This can be inserted into Eq.(A.14), and solved with respect to conversion directly

$$\frac{dX}{dt} = \frac{\frac{3}{R_p} \cdot (1 - X)^{2/3} \cdot \frac{b}{\rho_B \cdot R \cdot T} \cdot (P_{Ag} - P_{Ae})}{\frac{1}{k} + \frac{R_p \cdot [(1-X)^{1/3} - (1-X)^{2/3}]}{D_e} + \frac{(1-X)^{2/3}}{k_g}} \tag{A.18}$$

Finally, the unit consistency of Eq.(A.18) is carefully checked by introducing radius, external surface area and volume of the whole dolomite particle and at the core boundary. By using A=CO_2 and B=CaO, one can write:

b	[=]	$\frac{\text{mole CaO}}{\text{mole CO}_2}$
D_e	[=]	$\frac{\text{m}^3\text{ gas}}{\text{m core} \cdot \text{s}}$
k	[=]	$\frac{\text{m}^3\text{ gas}}{\text{m}^2\text{ core} \cdot \text{s}}$
k_g	[=]	$\frac{\text{m}^3\text{ gas}}{\text{m}^2\text{ dolomite} \cdot \text{s}}$
$\frac{P_A}{R \cdot T}$	[=]	$\frac{\text{mole CO}_2}{\text{m}^3\text{ gas}}$
R_p	[=]	m dolomite
X	[=]	$\frac{\text{m}^3\text{ reacted}}{\text{m}^3\text{ dolomite}}$
$(1\text{-X})^{2/3}$	[=]	$\frac{\text{m}^2\text{ core}}{\text{m}^2\text{ dolomite}}$
$R_p \cdot [(1\text{-X})^{1/3}\text{-}(1\text{-X})^{2/3}]=r_c \cdot (1\text{-}\frac{r_c}{R_p})$	[=]	m core
ρ_B	[=]	$\frac{\text{mole CaO}}{\text{m}^3\text{ dolomite}}$

Inserting into Eq.(A.18):

$$\frac{dX}{dt}[=]\frac{\frac{1}{\text{m dolomite}} \cdot \frac{\text{m}^2\text{ core}}{\text{m}^2\text{ dolomite}} \cdot \frac{\text{mole CaO}}{\text{mole CO}_2} \cdot \frac{\text{m}^3\text{ dolomite}}{\text{mole CaO}} \cdot \frac{\text{mole CO}_2}{\text{m}^3\text{ gas}}}{\frac{1}{\frac{\text{m}^3\text{ gas}}{\text{m}^2\text{ core} \cdot \text{s}}} + \text{m core} \cdot \frac{\text{m core} \cdot \text{s}}{\text{m}^3\text{ gas}} + \frac{\text{m}^2\text{ core}}{\text{m}^2\text{ dolomite}} \cdot \frac{\text{m}^2\text{ dolomite} \cdot \text{s}}{\text{m}^3\text{ gas}}} = \frac{\frac{\text{m}^2\text{ core}}{\text{m}^3\text{ gas}}}{\frac{\text{m}^2\text{ core} \cdot \text{s}}{\text{m}^3\text{ gas}}} = \frac{1}{s} \quad \text{(A.19)}$$

The units of the rate constant (k) and diffusivity (D_e) are for convenience written as m/s and m^2/s respectively.

A.2 Conversion dependent effective diffusivity

Zevenhoven et al. [74] introduced a conversion dependent effective diffusion constant to a shrinking core model for sulfidation of limestone and dolomite. The conversion dependent diffusivity accounts for the fact that intra-particle transport of mass and heat is strongly affected by the progress of conversion, with the build-up of a solid product layer. The following relationships are given:

$$\frac{V_{pore} + V_{pl}}{D_e} = \frac{V_{pl}}{D_{pl}} + \frac{V_{pore}}{D_{pore}} \tag{A.20}$$

where V is volume fraction

$$\text{product layer volume fraction} = (1 - \epsilon_0) \cdot X = V_{pl} \tag{A.21}$$

$$\text{porosity} = \epsilon_0 = V_{pore} \tag{A.22}$$

$$\text{Unreacted solid volume fraction} = (1 - \epsilon_0) \cdot (1 - X) = 1 - V_{pore} - V_{pl} \tag{A.23}$$

The diffusion of gas with a diffusion coefficient D_{mol} inside a porous structure, with porosity ϵ and tortuosity τ, is given by:

$$\frac{1}{D_{mol+Kn}} = \frac{1}{D_{mol}} + \frac{1}{D_{Kn}} \tag{A.24}$$

and

$$D_{pore} = D_{mol+Kn} \cdot \frac{\epsilon_0}{\tau} \tag{A.25}$$

$$D_{Kn} = 97 \cdot r_{av} \cdot (\frac{T}{M_{CO_2}})^{\frac{1}{2}} \tag{A.26}$$

where D_{Kn} is Knudsen diffusivity for an average pore radius r_{av}. D_{mol+Kn} is the combined molecular and Knudsen diffusivity in the gaseous phase inside the porous solid. Particle properties used for calculating diffusivity are listed in Table A.1.

Table A.1: Input parameters for diffusivity calculation

Parameter	Description	Value	Comment
τ	Tortuosity factor	5	For catalyst a factor of 3 is often used. Presumably higher for porous dolomite
ϵ_0	Porosity	0.5	Based on complete calcination of dolomite and a loss on ignition of ∼46%
r_{av}	Pore radius	$10 \cdot 10^{-9}$ m	Assumption

Combining the above equations:

$$D_e = D_e(X) = D_{eff,0} \cdot \frac{1 + AX}{1 + BX} \tag{A.27}$$

$$A = \frac{1-\epsilon_0}{\epsilon_0}, \qquad D_{eff,0} = D_{pore} = \frac{\epsilon_0}{\tau} \cdot D_{mol+Kn} \quad \text{and} \qquad B = \frac{A \cdot D_{pore}}{D_{pl}}$$

The molecular gas diffusivity can be calculated from the semi-empirical equation given by Reid and Sherwood [96]:

$$D_{A-I} = 1.858 \cdot 10^{-7} \cdot \frac{\sqrt{T^3 \cdot (\frac{1}{M_A} + \frac{1}{M_I})}}{P \cdot \sigma_{AI}^2 \cdot \Omega_D} \tag{A.28}$$

where A denotes CO_2 and I denotes inert gas, P is pressure (atm), M is the molar weight of the gases, σ_{AI} is a constant in the Lennard-Jones potential function and Ω_D is the collision integral. The following correlations are used for the calculations:

$$\sigma_{AI} = 1/2 \cdot (\sigma_A + \sigma_I) \tag{A.29}$$

$$\epsilon_{AI}/k = [\epsilon_A/k \cdot \epsilon_I/k]^{0.5} \tag{A.30}$$

$$\Omega_D = 0.88224 \cdot (kT/\epsilon)^{-0.73695} + 0.56241 \tag{A.31}$$

Table A.2: Lennard-Jones parameters for pure gas compounds

Compound	σ **[A]**	ϵ/k **[K]**
H_2	2.827	59.7
CO_2	3.941	195.2
CO	3.69	91.7
H_2O	2.641	809.1
Ar	3.542	93.3

Gas film diffusion constant

The mass transfer coefficient, k_g, between a single sphere and the surrounding gas is well described by a set of dimensionless groups

$$Sh_{single} = \frac{k_g \cdot d_p}{D} = 2 + 0.6 \cdot (Re_p)^{0.5}(Sc)^{0.333} \tag{A.32}$$

where D is the gas diffusivity (m^2/s), d_p is the particle diameter (m), Re_p is the particle Reynolds number and Sc is the Schmidt number. The dimensionless numbers are defined as:

$$Re_p = \frac{\rho_g \cdot U \cdot d_p}{\mu} \tag{A.33}$$

$$Sc = \frac{\mu}{\rho_g \cdot D} \tag{A.34}$$

where ρ_g is the gas density (kg/m^3), U is the gas velocity (m/s) and μ is the gas viscosity ($Pa \cdot s$). A correlation for calculating gas viscosity is found in Appendix C.2. Note that Eq.(A.32) is valid for a single sphere dispersed in a gas stream.

Appendix B: Reaction kinetics of Arctic dolomite

B.1 Response curves

The conversion-temperature curves as function of time are shown below. Experimental conditions are found in Table 3.6 in chapter 3.3.

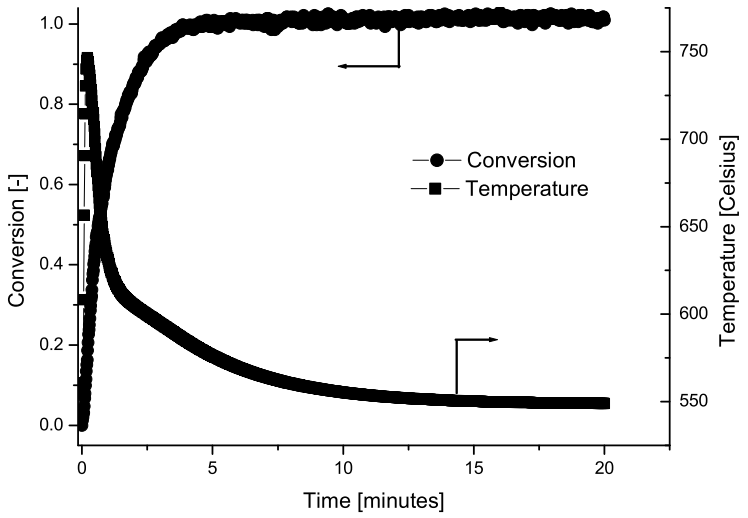

Figure B.1: Temperature and conversion of sorbent as a function of time for sample Kin-Dolo1.

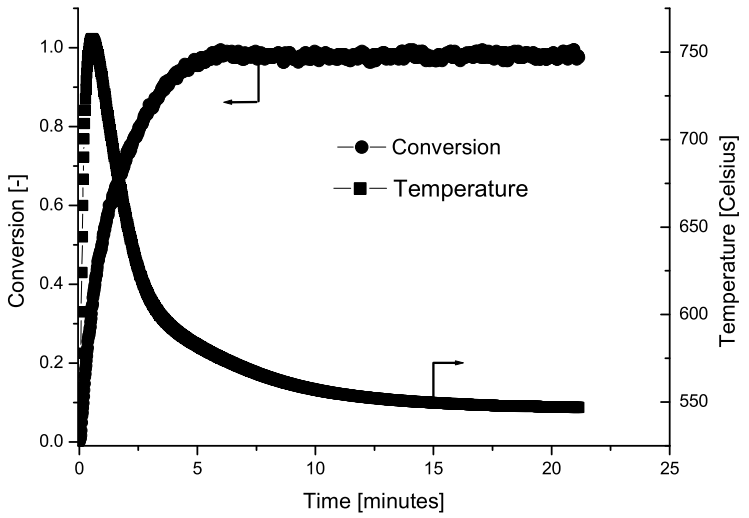

Figure B.2: Temperature and conversion of sorbent as a function of time for sample Kin-Dolo2.

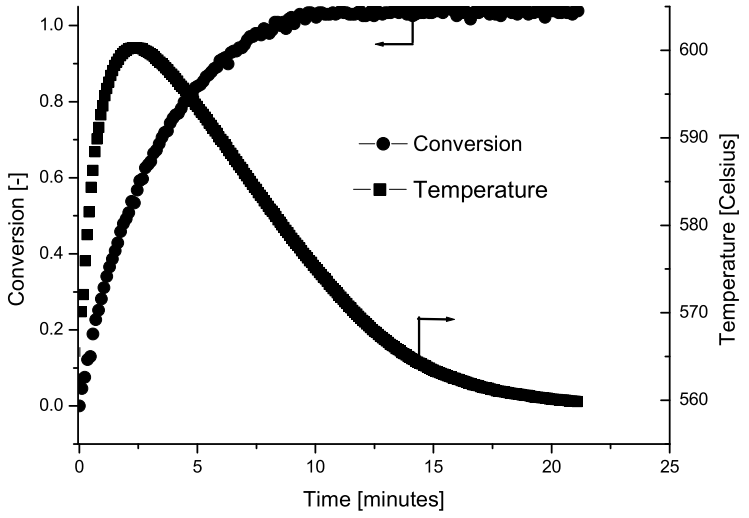

Figure B.3: Temperature and conversion of sorbent as a function of time for sample Kin-Dolo3.

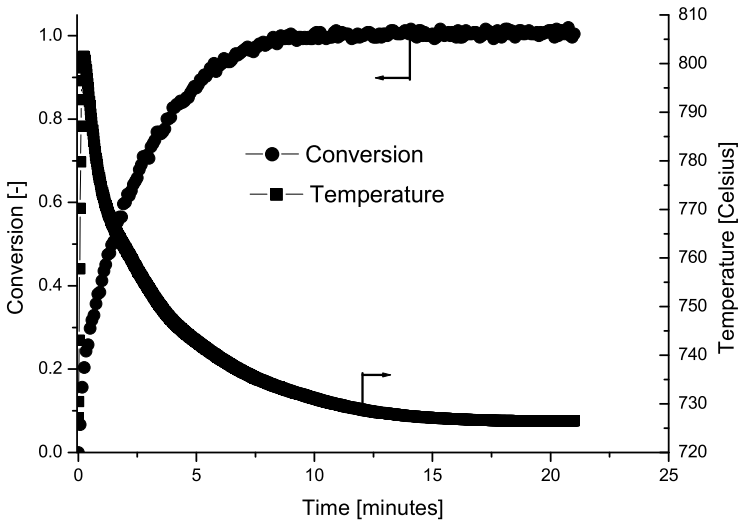

Figure B.4: Temperature and conversion of sorbent as a function of time for sample Kin-Dolo4.

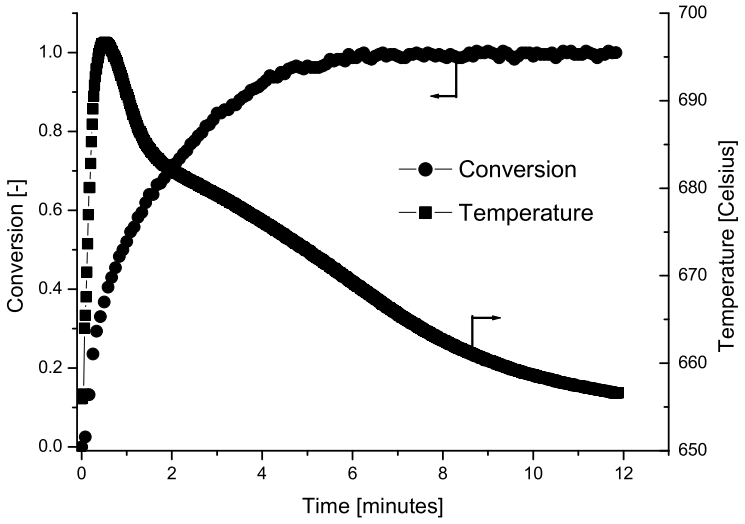

Figure B.5: Temperature and conversion of sorbent as a function of time for sample Kin-Dolo5.

B.2 Numerical solution: MATLAB scripts

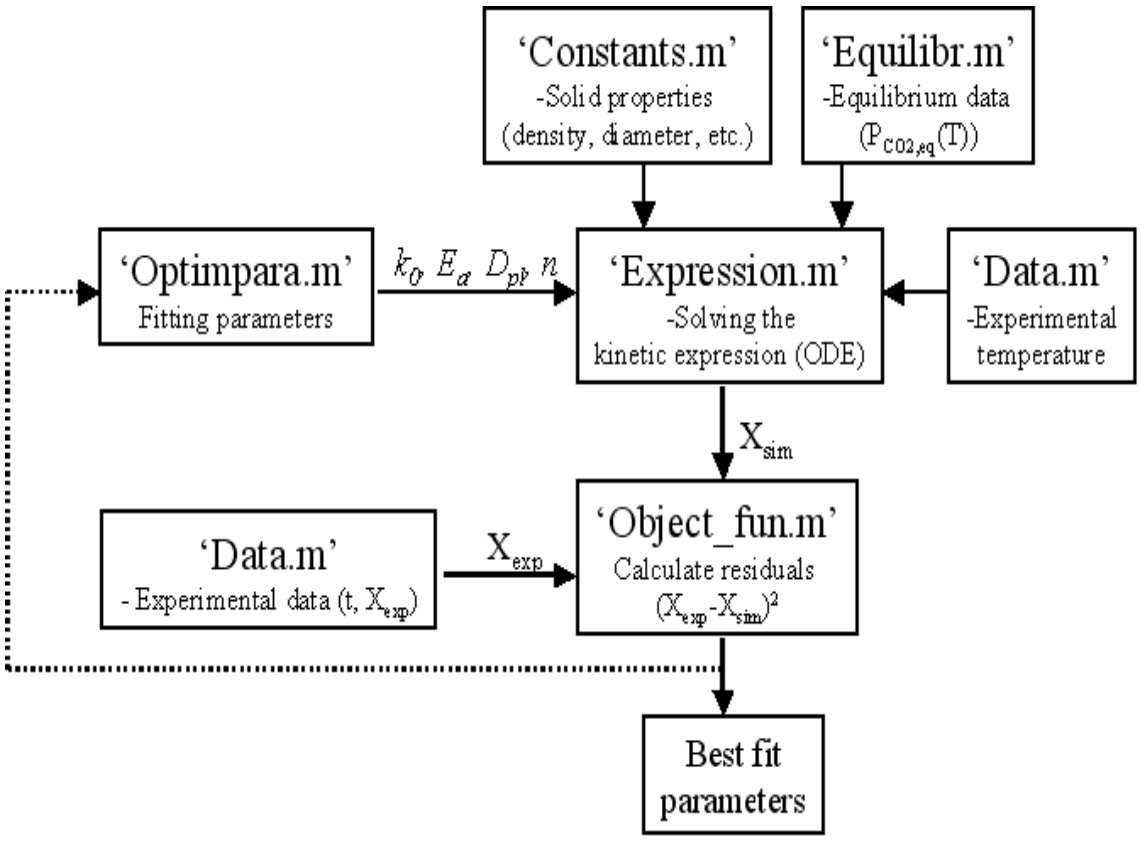

Figure B.6: Solving procedure for obtaining best-fit parameters.

The m-script-file, expression.m, is given below:

```
function [derivert] = expression(tid,x,T1,Pe1,xobs,k0,E,sz,De0,n_CO2f,n_argon,n)

T=T1;
Pe=Pe1;

% Solid properties
Diameter=[175 250 250 250 250].*10^(-6);  % particle diameter [m]
Rad=Diameter./2;
x_caO=0.32;                               % weight fraction CaO in dolomite
x_inert=0.2;                              % weight fraction MgO (inert) in dolomite
RHO_dolom=2870;                           % density of dolomite supplied from producent
RHO_dolo=RHO_dolom*(1-0.46);              % density of calcined dolomite (MgO*CaO) [kg/m3 ]
RHO_CaO=RHO_dolom*x_caO/56*1000;          % molar density of CaO in calcined dolomite [mol/m3]
RHO_CaCO3=RHO_dolom*x_caO/100*1000;       % molar density of CaCO3 in dolomite [mol/m3]
```

```
RHO_bulk=1480;                          % bulk density of dolomite (measured experimentaly) [kg/m3]
Eps_b=0.5;                              % Voidage of bed (approximate)
R=8.314;                                % Gas constant
Eps=.5;                                 % porosity of dolomite (assumption)
tort=5;                                 % tortuosity factor  (assumption)
r_av=10.*10^(-9);                       % pore radius   (assumption)

% Initial gas flow and solid amount
F_CO2=[2 1.6 2 1 2];                    % Nl/min
F_argon=[0 .4 0 1 0];                   % Nl/min
F_tot=F_CO2+F_argon;                    % Nl/min
m0=[10.14 10.16 10.7 10.2 10];          % inital weight of dolomite  [g]
n_s0=x_caO*m0/56;                       % moles of CaO at t=0
n_i=x_inert*m0/40.3;                    % moles inert
V_bed=m0./RHO_bulk/1000;                % volume of bed of solids
V_dolo=V_bed*(1-Eps_b);

% Updated gas flow
n_total=x(6:10)+n_argon;                % total mol/min flow of gas out
Pt=1;                                   % total pressure, atm
P=Pt*x(6:10)./n_total;                  % partial pressure of CO2, atm

% Gas phase diffusivity
epsilon_CO2=195.2;                                  % pure CO2
chi_CO2=3.941;
epsilon_mix=(195.2*93.3)^.5;                        % CO2 and Argon
chi_mix=.5*(3.941+3.54);
omega_CO2=0.88224.*((1/epsilon_CO2).*T).^(-0.73695)+0.56241;
omega_mix=0.88224.*((1/epsilon_mix).*T).^(-0.73695)+0.56241;
D_CO2=0.001858.*T.^(3/2).*((1./44+1./44).^.5./omega_CO2./Pt./(chi_CO2).^2);   % cm2/sec
D_mix=0.001858.*T.^(3/2).*((1./44+1./40).^.5./omega_mix./Pt./(chi_mix).^2);   % cm2/sec
De=[D_CO2 D_mix D_CO2 D_mix D_CO2]   ;          %   gas diffusity   [cm2/s]
De=De(1:5)./10000;                              %   m2/s
D_mol=De;

% Calculating Knutsen diffusion
D_kn=97.*r_av.*(T./44);
inv_Dmk=1./D_mol+1./D_kn;
D_kn=1./inv_Dmk;

% Effective diffusivity (using correlations from Zevenhoven)
A=(1-Eps)./Eps;
D_pore=D_kn.*Eps./tort;
D_pl=De0.*10^(-9);                                          % m2/s
B=A.*D_pore./D_pl;
D_eff=D_pore.*(1+A.*x(1:5))./(1+B.*x(1:5));                 % m2/s
D_eff=D_eff.*60;                                            % m2/min

% Calculation of gas film mass transfer coefficient
n_flow=F_tot./22.414/60;                        % Gas flow [mol/s]
F_new=0.082057.*T.*n_flow/1;                    % L/s @ reaction temperature
```

```
F_new=F_new/1000;
Area=24/10000;                                  % cross section area of reactor m2
u_0=F_new./Area;                                % linear gas velocity m/s

% Dimensionless groups
RHOg=P*1.013*10^5*44./8.314./T./1000;  % Gas density (average molecular weight 44 g/mole)[kg/m3]
Vis=3.5*10^(-6);                       % kg/m s    (Assumed constant  for pure CO2 at 650C)
VisKin=Vis./RHOg;                      % m2/s
Re=u_0.*Rad.*2./VisKin;                % Reynolds number
Sc=VisKin./D_mol;                      % dimensionless
Sh=2+0.6.*(Re).^(.5).*Sc.^(1/3);       % dimensionless
kg=De.*Sh./Rad./2;                     % m/s
kg=kg.*60;                             % m/min
P=1.013*10^5.*P;
Pe=1.013*10^5.*Pe;

% Numerator rate expression
Teller=3./Rad.*(1-x(1:5)).^(2/3).*(1./R./T./RHO_CaO).*(P-Pe).^(n/100);

% Rate of reaction
k=k0.*exp(-E.*1000/R./T);
Rx=1./k;

% Product layer diffusion
Diff=Rad.*((1-x(1:5)).^(1/3)-(1-x(1:5)).^(2/3))./D_eff;      % min/m

% External mass transfer
Film=(1-x(1:5)).^(2/3)./kg;                                  % min/m
r=RHO_CaO.*(Teller./(Film+Diff+Rx));
dxdt=r./n_s0.*V_dolo;
dn_CO2dt=n_CO2f-x(6:10)-r.*V_dolo;
derivert=[dxdt(1) dxdt(2) dxdt(3) dxdt(4) dxdt(5)dn_CO2dt(1) dn_CO2dt(2) dn_CO2dt(3) dn_CO2dt(4) dn_CO2dt(5)];
```

Appendix C: Two-phase model equations

C.1 Two-phase model

Bubble phase

The molar flux of specie i at any height in the bubble phase:

$$\beta \cdot U \cdot dC_{ib} = k_q \cdot (C_{id} - C_{ib}) \cdot a_b \cdot \epsilon_b \cdot dz \tag{C.1}$$

where a_b us the interfacial bubble area per unit bubble and ϵ_b is the fraction of bed volume occupied by bubbles.

Rearranging:

$$\frac{dC_{ib}}{dz} = \alpha \cdot (C_{id} - C_{ib}) \tag{C.2}$$

$$\alpha = \frac{k_q \cdot a_b \cdot \epsilon_b}{\beta \cdot U} \tag{C.3}$$

The boundary condition: C_{ib}=$C_{i,in}$ at z=0.

Integrating from z=0 to z=H (C_{id} is assumed to be constant throughout the column):

$$\ln \frac{(C_{ib} - C_{id})}{(C_{i,in} - C_{id})} = \alpha \cdot H \tag{C.4}$$

$$C_{ib} = C_{id} + (C_{i,in} - C_{id}) \cdot \exp(-\alpha \cdot H) \tag{C.5}$$

Dense phase

$$(1-\beta)\cdot U\cdot(C_{i,in}-C_{id})+\int_0^H k_q\cdot(C_{ib}-C_{id})\cdot a_b\cdot\epsilon_b\cdot dz=(1-\epsilon_b)\cdot(1-\epsilon_{mf})\cdot H\cdot R_i \quad \text{(C.6)}$$

Substituting Eq.(C.5) into Eq.(C.6):

$$(1-\beta)\cdot U\cdot(C_{i,in}-C_{id})+k_q\cdot(C_{i,in}-C_{id})\cdot a_b\cdot\epsilon_b\cdot\int_0^H \exp(-\alpha\cdot H)dz=(1-\epsilon_b)\cdot(1-\epsilon_{mf})\cdot H\cdot R_i \quad \text{(C.7)}$$

Solving the integral:

$$\int_0^H \exp(-\alpha\cdot H)dz=\frac{1}{\alpha}\cdot(1-\exp(-\alpha\cdot H)) \quad \text{(C.8)}$$

Inserted into Eq.(C.7):

$$(1-\beta)\cdot U\cdot(C_{i,in}-C_{id})+k_q\cdot(C_{i,in}-C_{id})\cdot a_b\cdot\epsilon_b\cdot\frac{1}{\alpha}\cdot(1-\exp(-\alpha\cdot H))=(1-\epsilon_b)\cdot(1-\epsilon_{mf})\cdot H\cdot R_i \quad \text{(C.9)}$$

Inserting for α and rearranging:

$$U\cdot(C_{i,in}-C_{id})\cdot(1-\beta\cdot\exp(-\alpha\cdot H))=(1-\epsilon_b)\cdot(1-\epsilon_{mf})\cdot H\cdot R_i \quad \text{(C.10)}$$

$$C_{id}=C_{i,in}-\frac{(1-\epsilon_b)\cdot(1-\epsilon_{mf})\cdot H\cdot R_i}{(1-\beta\cdot(\exp(-\alpha\cdot H))\cdot U} \quad \text{(C.11)}$$

C.2 Correlations

Correlations used in the model are listed here.

Viscosity

The viscosity of the pure compound is as defined by Lydersen [97]:

$$\mu_i = \frac{b_i \cdot T^{1.5}}{T + S_i} \tag{C.12}$$

where b_i and S_i are constants listed in Table C.1.

Table C.1: Coefficients for viscosity calculations

Compound	$\mathbf{b}_i$ **[kg/m s K$^{0.5}$]**	$\mathbf{S}_i$ **[K]**
H_2	0.65e-6	67
CO_2	1.50e-6	220
CO	1.46e-6	110
CH_4	1.00e-6	165
H_2O	1.74e-6	626

An estimate of the viscosity of a gas mixture can be found by using the correlation by Wilke [98]:

$$\mu_{mix} = \sum_{i=1}^{n} \frac{x_i \cdot \mu_i}{\sum_{j=1}^{n} x_i \cdot \phi_{ij}} \tag{C.13}$$

where

$$\phi_{ij} = \frac{1}{\sqrt{8}} \cdot (1 + \frac{M_i}{M_j})^{-0.5} \cdot (1 + (\frac{\mu_i}{\mu_j})^{0.5} \cdot (\frac{M_j}{M_i})^{0.25})^2 \tag{C.14}$$

where M is the molar weight and x_i is the mole fraction. It is claimed that this correlation gives good estimates of gas mixture viscosities for most cases, especially for mixtures with gases having molar weights close to each other. Another way of estimating the viscosity of mixtures, is by assuming that there is a linear dependency of the viscosity of mixture of the pure compounds:

$$\mu = \sum_i \mu_i \cdot x_i \tag{C.15}$$

An average of these two correlations has been adopted, based on comparison with the viscosity calculated by the Ergun software (Ergun 6.0, Divergent S.A.).

Heat capacity

The heat capacity of the pure compounds is described by:

$$C_{P,i} = A_i + B_i \cdot T + \frac{C_i}{T^2} + D_i \cdot T^2 \tag{C.16}$$

The coefficients, obtained from HSC Chemistry (HSC Chemistry 6.0, Outokumpu Research Oy), are listed in Table C.2.

Table C.2: Coefficients for calculation of the heat capacity

Compound	**A [J/mole K]**	**B [J/mole K^2]**	**C [J K/mole]**	**D [J/mole K^3]**
CH_4	2.23	96.94e-3	6.11e5	-26.04e-6
CO	25.87	6.51e-3	1.11e5	1.02e-6
CO_2	29.31	39.97e-3	-2.48e5	-14.78e-6
H_2	25.86	4.84e-3	1.58e5	-0.37e-6
H_2O	28.41	12.48e-3	1.28e5	0.360e-6
CaO	57.76	-10.78e-3	-11.51e5	5.23e-6
$CaCO_3$	99.54	27.14e-3	-21.47e5	0.002e-6
MgO	47.49	4.65e-3	-10.34e5	-0.27e-6
$MgCO_3$	73.35	63.95e-3	-14.50e5	0.02e-6
$MgAl_2O_4$	153.85	26.84e-3	-40.62e5	0

Appendix D: Papers

Is not included due to copyright